Stony Brook University

Using Seismic Observations and Modeling to Place Constraint on the Structure Beneath Japan and Central America

A Dissertation Presented

by

Hui Long

to

The Graduate School

In Partial Fulfillment of the

Requirements

for the Degree of

Doctor of Philosophy

in

Geosciences

Stony Brook University

December 2014

Stony Brook University
The Graduate School

Hui Long

We, the dissertation committee for the above candidate for the
Doctor of Philosophy degree, hereby recommend
acceptance of this dissertation.

Lianxing Wen – Dissertation Advisor
Professor, Department of Geosciences

William Holt - Chairperson of Defense
Professor, Department of Geosciences

Donald J. Weidner
Distinguished Professor, Department of Geosciences

Baosheng Li
Research Professor, Mineral Physics Institute

Lupei Zhu
Professor, Department of Earth and Atmospheric Sciences
Saint Louis University

This dissertation is accepted by the Graduate School

Charles Taber
Dean of the Graduate School

Abstract of the Dissertation

Using Seismic Observations and Modeling to Place Constraint on the Structure Beneath Japan and Central America

by

Hui Long

Doctor of Philosophy

in

Geosciences

Stony Brook University

2014

Understanding Earth's internal structure by seismic observations, both temporally and spatially, is key in seismology. In this thesis, I constrained structural changes beneath the Japan subduction zone based on a newly developed theory, and detailed mid to lower mantle structure beneath Central America by waveform and travel time observations and modeling.

A newly developed theory states that the differential wave field of two repeated sources in a temporally changed medium can be equivalently treated as wave fields propagating from virtual point sources or volumetric sources. The virtual point sources or volumetric sources are located at the place of temporal changes, and their strengths are equal to the product of magnitude of medium property change and magnitude of the

initial wave fields from the repeated sources. Applying the theory to the Japan subduction zone, we then locate the temporal change of seismic properties beneath this area between 2011 and 2013 to be at $(37.2^{\circ}N, 142^{\circ}E)$, and estimate the magnitude of the conceptual body force associated with the temporal change to be 1.15×10^{10} N, or as a reference, a 0.87% density change for an assumed volume of temporal change of 10^3 km^3.

Seismic waveform and travel time observations sampling the mid to lower mantle beneath Central America are analyzed and modeled. Waveform observations show complex reflection phases and exhibit significant variations with azimuth and distance, and travel time analyses show increasing S residuals of up to 9 seconds as distance increases from 45° to 80°. Forward waveform and travel time modeling reveals that several sub-horizontal 10-20 km thick segments with –10% shear wave velocity perturbation are buried inside a "trapezoid-like" low velocity region with –2% shear wave velocity perturbation extending between 1000 and 2750 km depth. In addition, analyses of the ScSH-SH and PcP-P differential travel time residuals suggest a structural transition in the lowermost mantle beneath Central America. Comparisons of stacked waveforms across the region indicate relatively uniform attenuation. Rapidly changing ScSH/SH amplitude ratio and incoherently delayed radial component S phases both indicate widely existing anisotropy and heterogeneity.

Table of Contents

List of Figures

List of Tables

Acknowledgements

The completion of my Ph.D. study and dissertation has been a long journey. It was not an easy journey for me, involving a lot of ups and downs. And there are a number of people without whom I might not have been able to accomplish this journey.

Foremost, I would like to express my sincere gratitude to my advisor Lianxing Wen for the patient guidance, encouragement and advice he has provided throughout my time as his student. He is truly a great mentor, with his great attitude and passion inspiring me so much. I am grateful to other dissertation committee members, Lupei Zhu, William Holt, Donald J. Weidner and Baosheng Li, for spending time to go through all the details of the dissertation with me. I also want to give a huge thanks to the staff, faculty and graduate students from Geosciences department. Life would have been a lot harder without your help. I benefited so much from group meetings and discussions with labmates and colleagues, Yi Wang, Yu Chen, Yumei He, Li Sun, Zhiyang Dai, Wei Wang and Miao Zhang. Also, I would like to acknowledge IRIS and Hi-Net for providing precious data for my Ph.D. study.

To my family and friends, thank you for listening, offering me advice, and supporting me through this entire process. My dearest mom and dad, you should know that your support and encouragement is worth more than I can express on paper. Special thanks to my Stony Brook friends, Yi Wang, Wei Zhu, Congcong Che, Yuyan Zhao, Yu Chen, Wenqian Xu, Josephine Durand, Cecillia Cheung, Gina Shcherbenko and many

others. To my friends scattered around the country and overseas, thank you for your thoughts, phone calls, emails, texts, visits, and being there whenever I needed you.

Chapter 1

General Introduction

The solid Earth is a restless planet, which involves dynamics at different scales. One end member of large-scale dynamics of Earth is the mantle convection. The slow creeping motion of mantle caused by convection not only enables tectonic plates to move around the Earth's surface, subduct under each other at convergent boundaries, but also enable mantle materials to sink, rise and trespass which generates lateral heterogeneity. Another end member of small-scale dynamics compared with mantle convection is earthquake activities. The occurrence of an earthquake involves stress and strain accumulation and release near seismic fault zones in time spans of years or days. It is natural to be intrigued by the mystery of earth's structure and how it works.

The Earth's elastic vibrations are embedded codes containing wealthy information about the structures through which they propagate. Through generations of seismologists decoding seismograms, the resolution of Earth's interior picture continues to be improved. Early regional and global travel time studies discovered Earth's primary structures, the Mohorovicic discontinuity, the core-mantle boundary, and the outer core-inner core boundary. Later on, with the progression of seismic networks and computational methods, studies about more complex structures and dynamic processes at different scales bloomed, including the D'' layer, the transition

zone, the ULVZ, earthquake ruptures and etc. In the 80s and 90s, revolutionary 1D Earth velocity models were published and are still in use, such as PREM, IASP91, andAK135-F. Nowadays, various 3D tomography pictures and updated regional structural studies continue to provide new and detailed information about the deep Earth structure. Through interpretation, each seismic finding tells a story about the status or evolution of the Earth. Unfortunately, to fully understand Earth's interior and how it changes, these findings are far from completion. Therefore, it is necessary to keep exploring the Earth internal structure through seismic observations, both temporally and spatially.

Seismology is an observational science, composed of highly specialized sub-disciplines, that relies heavily on the availability of data. Based on types of data, it includes body wave (P and S wave), surface wave (Rayleigh and Love wave), normal modes and ambient noise studies. In this thesis, I choose to use body wave to study two regions, Japan and Central America, benefiting from two of the densest seismic networks in the world, Hi-net and USArray.

Japan is a study region with great numbers of seismic recorders and sources. Hi-net seismic network encompasses over 700 Hi-net seismic stations that are deployed all over Japan in a roughly 20-km mesh. These stations are installed at the bottom of over 100 meter deep boreholes, and thus are able to detect non-human-sensitive weak ground shaking by micro-earthquakes. Real-time Hi-net seismic data has been available since 2004. Additionally, being on the conjunction area of the Eurasian plate, North American plate, Pacific plate and Philippine Sea plate, Japan's

location gives it a strong seismogenic geological setting and one of the densest seismicities. Therefore, the ability to find and locate repeating earthquakes as great sources for studying time-lapse structural changes is enhanced. In this project, a new theory, which uses repeated sources and their difference wave field to quantify time-lapse structural change, is derived and applied in Japan.

On the other side of the Earth, Central America is a classic study region that allows utilizing seismic events from South America and recorders in North America. Over 400 portable USArray seismic stations have been deployed across the United States in an approximately 70-km spacing mesh since 2004. The great improvement of seismic station coverage in the US, especially outside of the western US, provides a precious opportunity to study the mid to lower mantle structure beneath Central America in details. In this project, we explore the interesting waveform and travel time features of the mid to lower mantle, and build reliable velocity structures through seismic modeling.

In this thesis, I present a new theory for quantitative determination of temporal change of structure and application of the theory in Japan in Chapter 2; Then I present detailed seismic observations and modeling results of a shear wave low velocity structure in the mid-lower mantle beneath Central America in Chapter 3, and S and P wave observations tied to a structural transition in the lowermost mantle beneath Central America in Chapter 4; Finally I summarize the main conclusions in Chapter 5.

Chapter 2

Using Repeated Sources to Quantitatively Determine Temporal Change of Medium Properties: Theory and an Example

2.1 Abstract

We develop a theory of using difference wave fields of repeated sources to locate and quantify temporal medium change and apply the theory to locate temporal change of seismic properties beneath the Japan subduction zone using repeated earthquakes. Our theory states the difference wave fields of two repeated sources in a temporally changed medium can be equivalently treated as wave fields propagating from conceptual sources, with their location at the place of temporal change and their strengths equal to the product of magnitude of medium property change and magnitude of the initial wave fields from the repeated sources. When the medium change extends to a finite region, the conceptual sources become volumetric sources distributed over the region of the medium change and propagating in the direction of the initial wave. The conceptualization establishes a theoretical framework for possible applications of using difference wave fields to locate and quantify temporal medium changes in geological sciences, ultrasonic experiments, civil engineering and medical imaging. We search repeating earthquakes occurring in the Japan subduction zone, formulate an empirical procedure to extract the difference wave fields between

repeating earthquakes and determine temporal change of seismic properties using a back-projection method. We locate the temporal change of seismic properties beneath the Japan subduction zone to be at $(37.2°N, 142°E)$, and estimate the magnitude of the conceptual body force associated with the temporal change to be 1.15×10^{10} N, or as a reference, a 0.87% density change for an assumed volume of temporal change of 10^3 km^3.

2.2 Introduction

Using seismic or ultrasonic waves to probe temporal change in the medium is an important topic in ultrasound experiments, civil engineering, medical imaging and geological sciences. In ultrasound experiments, scattered waves of repeated sources are used to estimate nonlinear behavior in seismic velocity using coda wave interferometry [*Snieder et al*., 2002*; Gret et al*., 2006]. In civil engineering, repeated ultrasonic waves are used to monitor rock fractures of a building [*Young and Collins*, 2001]. In medical imaging, ultrasound images have been used to monitor cerebral blood flow changes in focal ischemia in rabbits [*Els et al*., 1999*; Bonnin et al*., 2008*; Li et al*., 2010]. And, in geological sciences, repeated seismic sources or explosions are used to monitor volcano activities [*Poupinet et al*., 1984*; Martini et al*., 2009], seismic velocity changes before an earthquake [*Niu et al*., 2008] and following large earthquakes [*Li et al.,* 1998; *Baisch and Bokelmann*, 2001; *Matsumoto et al.*, 2001; *Vidale and Li*, 2003; *Ikuta and Yamaoka*, 2004; *Schaff and Beroza*, 2004; *Nishimura et al*., 2005; *Peng and Ben-Zion*, 2006; *Rubinstein et al*., 2007; *Li et al*., 2007; *Cheng et al*., 2011], temporal evolution of oil production fields [*Lumley*, 2001; *Rickett and Lumley*, 2001], underground carbon sequestration [*Santos and Harris*, 2009] and

temporal change of seismic signals related to change of the properties in the crust [*Bokelmann and Harjes*, 2000; *Furumoto et al*., 2001; *Niu et al.,* 2003; *Taira et al.,* 2008; *Zhao and Peng,* 2009; *Cheng et al.,* 2011] and in the Earth's core [*Zhang et al.,* 2005; *Wen*, 2006; *Cao et al*., 2007; *Zhang et al.*, 2008]. Recently, repeated ambient noise analysis provides another means for monitoring temporal change of elastic medium [*Sens-Schonfelder and Wegler*, 2006; *Snieder et al.*, 2007; *Wegler and Sens-Schonfelder*, 2007; *Brenguier et al*., 2008a, 2008b].

It is clear from these studies that probing temporal medium change has not only started to provide fundamental insights into physics of many geophysical phenomena, such as earthquake nucleation, fault zone damage and healing process, volcano activities, stress build-up in the crust and the thermo-chemical processes in the top of the Earth's inner core, but also become a practical and effective tool for monitoring evolution of oil fields and underground carbon sequestration. Two types of approach have been developed in detecting temporal change of medium properties. One approach is to obtain the medium images at different time steps and extract the difference between the images, while the other one is to relate the difference of waveform characteristics of the repeated sources or the Green's functions obtained from noise correlations to temporal change of medium properties. The issue, however, has always been challenging, because the signal associated with the temporal change is usually very weak compared to background waves, and the methods of detecting it require extremely high resolution and great care. In the approach of comparing images at different time steps, the presence of noise and actual station distribution make the resolution analysis difficult in constructing images using the background

waves. The potential artifacts in the time-lapse images could significantly affect the identification and inference of temporal change in the medium. In the approach of relating the difference of waveform characteristics of the repeated sources or the Green's functions obtained from noise correlations to temporal change of medium properties, the repeatability of the source is always a practical issue for both ambient noise and repeated events including the controlled sources. In addition, most of the methods in this approach only provide an average estimation of the bulk medium.

In this chapter, we establish a theoretical framework that conceptualizes propagation of difference waves fields, defined as the wave field difference between the repeated sources, and uses difference wave fields to effectively image temporal change of properties in the medium. The conceptualization we propose would make experiment design and resolution analysis straightforward, and overcome many challenging issues in the current methods of determining temporal property change in the medium. The conceptualization also makes it possible to pinpoint and quantify temporal change inside the medium. We apply the theory to search temporal change of medium properties beneath the Japan subduction zone using the difference *SH* waveforms of a pair of moderate-size earthquake doublet recorded at the Hi-net stations. We present the theory in Section 2.3, application to the determination of temporal seismic change beneath the Japan subduction zone in Section 2.4, and discussion and conclusion in Sections 2.5, 2.6.

2.3 Theoretical framework of relating the difference wave fields with temporal change of medium

We use two-dimensional *SH* wave propagation to demonstrate the concept. The extension of the concept to the *P-SV* system or to three-dimensional wave propagation is straightforward. We are dealing with the wave propagation problem that repeated sources are used at (x_s, z_s), and there is a change of medium properties of density and shear modulus between the timing of the repeated sources. The theory is to relate the observed difference wave fields to the location and magnitude of the property changes in the medium.

SH elastic wave propagation in a two-dimensional x - z medium is governed by the following equations:

$$-f\delta(x - x_s, z - z_s) + \rho(x,z)\frac{\partial v}{\partial t} = \frac{\partial \sigma_{xy}}{\partial x} + \frac{\partial \sigma_{zy}}{\partial z} \tag{2.1}$$

$$\frac{\partial \sigma_{xy}}{\partial t} = \mu(x,z)\frac{\partial v}{\partial x} \tag{2.2}$$

$$\frac{\partial \sigma_{zy}}{\partial t} = \mu(x,z)\frac{\partial v}{\partial z} \tag{2.3}$$

where f is body force, (x_s, z_s) location of repeated sources, v velocity wave field, σ_{xy}, σ_{zy} stresses, ρ density, μ shear modulus, and t time.

Let $v = v_0$, $\sigma_{xy} = \sigma_{xy,0}$, $\sigma_{zy} = \sigma_{zy,0}$ be the velocity and stress wave fields and $\rho = \rho_0$, $\mu = \mu_0$ the density and shear modulus of the medium associated with the first source; $v = v_0 + \delta v$, $\sigma_{xy} = \sigma_{xy,0} + \delta\sigma_{xy}$, $\sigma_{zy} = \sigma_{zy,0} + \delta\sigma_{zy}$, $\rho = \rho_0 + \delta\rho$, $\mu = \mu_0 + \delta\mu$ be those of the latter source. Inserting these variables for the latter source

into equations (2.1 - 2.3) and ignoring second-order perturbations, one yields the following equations related to the difference wave fields:

$$\rho(x,z)\frac{\partial \delta v}{\partial t} + \delta\rho(x,z)\frac{\partial v_0}{\partial t} = \frac{\partial \delta\sigma_{xy}}{\partial x} + \frac{\partial \delta\sigma_{zy}}{\partial z} \tag{2.4}$$

$$\frac{\partial \delta\sigma_{xy}}{\partial t} = \mu(x,z)\frac{\partial \delta v}{\partial x} + \delta\mu(x,z)\frac{\partial v_0}{\partial x} \tag{2.5}$$

$$\frac{\partial \delta\sigma_{zy}}{\partial t} = \mu(x,z)\frac{\partial \delta v}{\partial z} + \delta\mu(x,z)\frac{\partial v_0}{\partial z} \tag{2.6}$$

where $\delta\rho$, $\delta\mu$ are temporal change of density and shear modulus between the sources, and δv, $\delta\sigma_{xy}$, $\delta\sigma_{zy}$ are difference velocity and stresses of the wave fields as a result of the medium property changes.

Let us first consider the case that the property change is localized at a single point in space (x_c, z_c), i.e., $\delta\rho(x,z) = \Delta\rho\delta(x - x_c, z - z_c)$ and $\delta\mu(x,z) = \Delta\mu\delta(x - x_c, z - z_c)$. Equations (2.4 – 2.6) now become:

$$\rho(x,z)\frac{\partial \delta v}{\partial t} - f\delta(x - x_c, z - z_c) = \frac{\partial \delta\sigma_{xy}}{\partial x} + \frac{\partial \delta\sigma_{zy}}{\partial z} \tag{2.7}$$

$$\frac{\partial \delta\sigma_{xy}}{\partial t} = \mu(x,z)\frac{\partial \delta v}{\partial x} + s_x\,\delta(x - x_c, z - z_c) \tag{2.8}$$

$$\frac{\partial \delta\sigma_{zy}}{\partial t} = \mu(x,z)\frac{\partial \delta v}{\partial z} + s_z\,\delta(x - x_c, z - z_c) \tag{2.9}$$

where $f = -\Delta\rho\frac{\partial v_o}{\partial t}|_{(x,z)=(x_c,z_c)}$, $s_x = \Delta\mu\frac{\partial v_o}{\partial x}|_{(x,z)=(x_c,z_c)}$, and $s_z = \Delta\mu\frac{\partial v_o}{\partial z}|_{(x,z)=(x_c,z_c)}$.

Note that, other than two additional source terms, s_x and s_z being at (x_c, z_c), and the body force term f at (x_c, z_c), equations (2.7 – 2.9) are identical to equations (2.1 – 2.3). Equations (2.7 - 2.9) thus state that the difference wave fields can be treated as the wave fields that propagate in the same medium as the initial waves, with a conceptual body force f and conceptual stress perturbations, s_x and s_z, at the

location of property change (Figure 2.1a, 2.1b). The magnitude of the conceptual body force is equal to the negative of the product of density change and acceleration of the initial wave fields at the location of density change; the magnitudes of the conceptual stress perturbations are equal to the product of shear modulus change and strains (displacement gradients) of the initial wave fields at the location of shear modulus change.

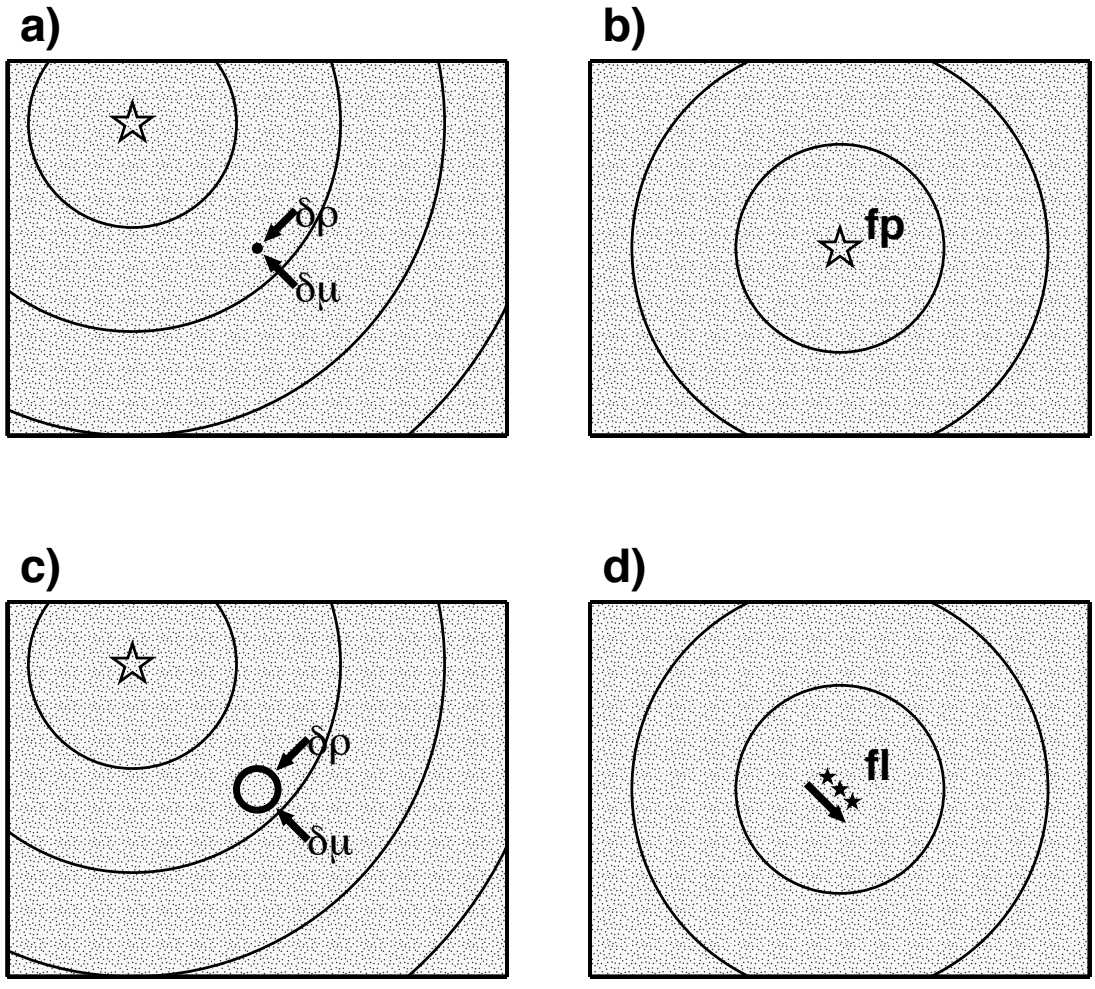

Figure 2.1. Conceptualization of propagation of difference wave fields of repeated sources in changed media. a) Cartoon illustration of wave propagation of repeated sources in a temporally changing medium. Sources are repeated at the location represented by star. Between the repeated sources, a density change ($\delta\rho$) and a shear

modulus change ($\delta\mu$) occur at the location represented by dot; b) conceptual source model for propagation of difference wave fields in a). Wave fields propagate in the same background medium in a), the conceptual source situates at the location where the medium change occur (star and dot in a); and the strength of the conceptual source, fp, is a summation of s_x, s_z, and f (see text); c) same as a), except that the medium changes extend to a finite region represented by circle; d) volumetric sources model for propagation of difference wave fields in c). Wave fields propagate in the same background medium in c), volumetric sources (stars in a circular volume lined up in the propagating direction of source) are distributed in the region of medium changes and propagating in the direction of initial wave (arrow), the strength of the net force, fl, is the volumetric integration of fp in b).

When temporal change of elastic properties extends to a finite region, the conceptual source would be the volumetric integration of equivalent forces in the region of medium change. Since the initial wave fields (acceleration and strains) of the actual source arrive at different time for different parts of the changed medium and the equivalent forces take effects at the arrival times of the initial waves, the equivalent forces become a propagating force, traveling in the direction of initial waves impinged on the changed medium (Figure 2.1c, 2.1d).

Numerical simulations indicate that such conceptualization of difference wave propagation accurately reproduces the difference wave fields. An example is shown for a homogeneous whole space medium (Figure 2.2a - 2.2d). In this example, the earlier source generates a wave field in a homogeneous whole space and the latter source propagates through the same medium, but with a density change of 50% at the point represent by the dot (Figure 2.2a). The wave fields for the two sources are calculated by a finite-difference technique [*Wen*, 2002] and difference wave fields are

obtained by subtracting the wave fields of the earlier source from those of the latter source (Figure 2.2b). In the conceptual model, a source is placed at the location of density change with the magnitude of the body force equal to the product of density change and acceleration of wave fields of the earlier source at the location of the density change (star, Figure 2.2c). The wave fields for the conceptual source model match the difference wave fields well in time, amplitude and shape. This is evident from snapshots (Figure 2.2b, 2.2d) and examples of waveform comparison (Figure 2.3a).

When the density change extends to a finite region (Figure 2.2e), the residual wave fields exhibit direction dependence with respect to the direction of the initial waves from the repeated sources (Figure 2.2f), or directivity typical of a finite propagating source. The residual wave fields exhibit narrower shapes and stronger amplitudes (Figure 2.2f and the top traces in Figure 2.3b) in the direction of the initial wave impinged on the changed media (arrow in Figure 2.2f), broader shapes and smaller amplitudes (Figure 2.2f and the bottom traces in Figure 2.3b) in the direction away from the initial wave propagation, and waveform features intermediate to those in and away from the initial wave propagation (Figure 2.2f and the middle two trace pairs in Figure 2.3b) for the receivers in the direction perpendicular to the initial wave propagation.

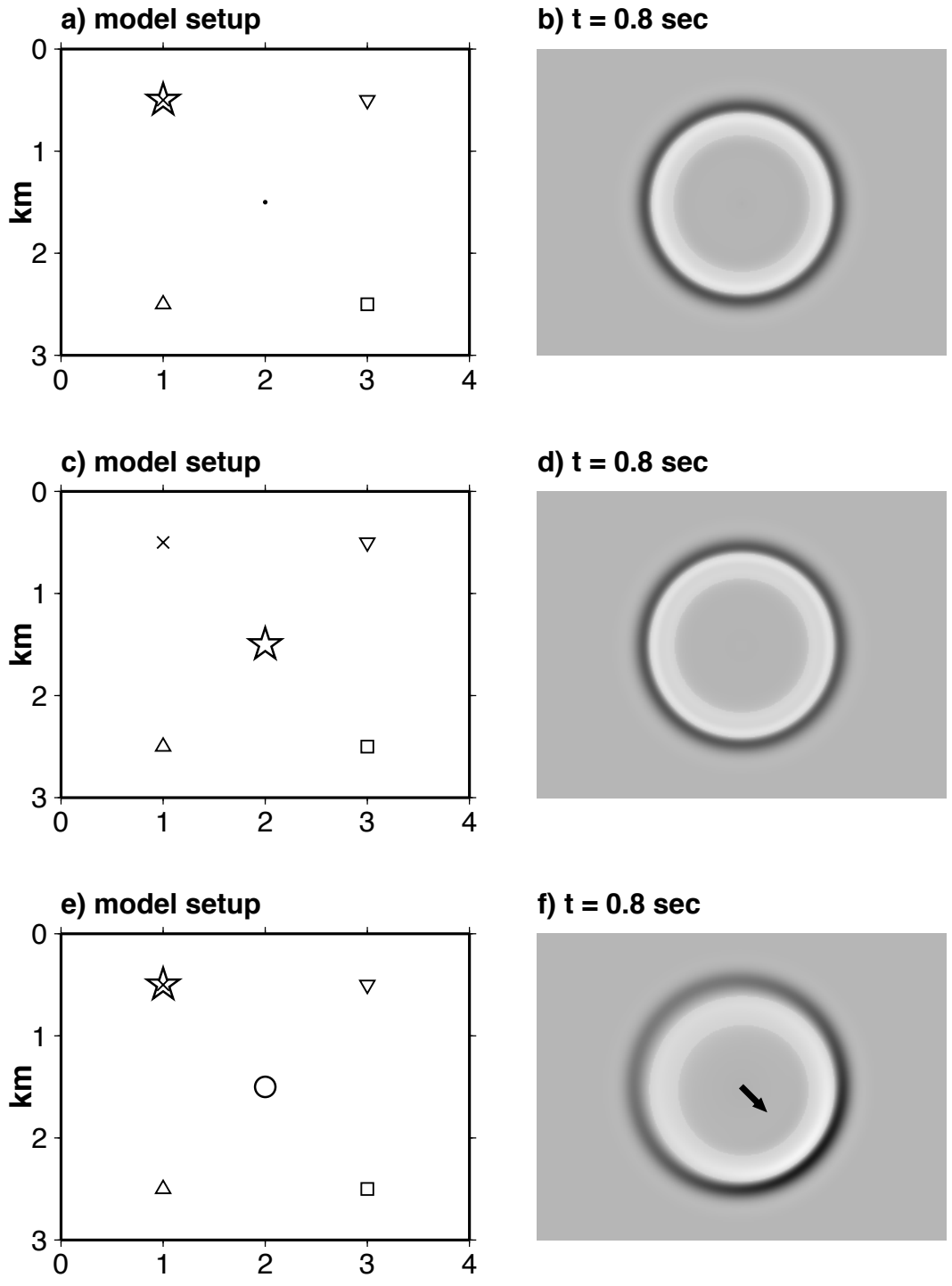

Figure 2.2. Comparisons of difference wave fields of repeated sources from a conceptual source for a homogeneous whole space with a density of 2.6 g/cm^3 and a shear velocity of 2.85 km/s. a) model setup, repeated sources (star) and location of the density change (dot); b) a snapshot of difference wave fields of the repeated sources. Difference wave fields are obtained by subtracting the wave fields for homogeneous whole space from those for a model with a density change of 50% in the

location represented by the dot in whole space; c) model setup for wave fields of a conceptual source located at the place of density change (star and the same represented by dot in a), with a strength equal to the product of density change and acceleration of the initial waves; d) snapshot of wave fields for the conceptual source at the same time step in b); e) model setup same as in a), except the density change occurs in a finite region represented by circles; f) snapshot of difference wave fields for model e. For comparison, the amplitudes of residual fields are scaled to a point source based on the volumetric distribution of the density change. Arrow indicated the direction of the initial waves from the repeated sources impinged on the location of density change. Cross, triangles and square in three models represent four receiver sites.

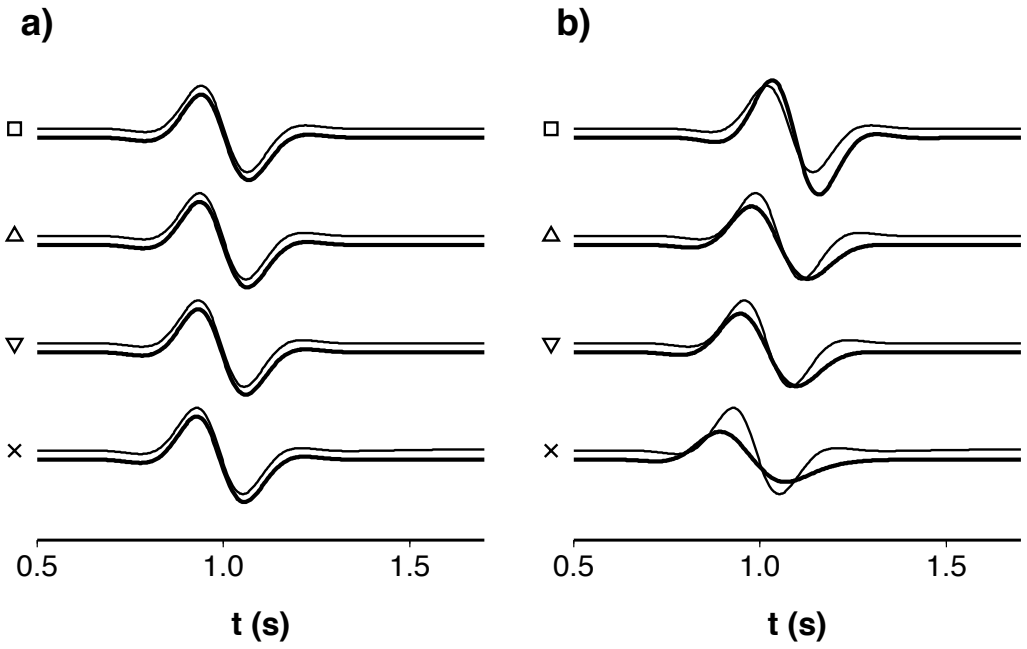

Figure 2.3. Synthetic waveform comparisons of difference wave fields of repeated sources from a conceptual source. a) Comparisons of waveforms of difference wave fields (heavy traces) obtained for model setup in Fig. 2.2a and wave fields (light traces) generated by a conceptual source for model setup in Fig. 2.2c; b) same as a), except that wave fields are for model setup in Fig. 2.2e. For comparison, the amplitudes of the residual fields are scaled based on the volumetric distribution of the density change. Synthetic waveforms are labeled with the symbols according to the receiver locations in Fig. 2.2a, 2.2c, 2.2e.

Since, except for the equivalent source terms, equations (2.7 – 2.9) are identical to the governing equations for the initial waves, the conceptualization of residual wave fields propagation (Figure 2.1) applies to any types of heterogeneous media. This is illustrated in a half-space model that consists of a free surface and random variations of seismic velocity of 4% with correlation scale lengths of 200 m in both *x*- and *z*- directions. The conceptual source in this case contains two major parts related to the initial direct wave and the reflected initial wave from the free surface, and minor components associated with the scattering of the initial waves from the random medium. The conceptual source model of wave propagation reproduces all the features of the residual waves, including various components related to direct, reflected and scattered initial waves, their interaction with free surface and interference of various components of residual waves, as evident from comparisons of snapshots (Figure 2.4b – 2.4d, 2.4f – 2.4h) and synthetic waveforms (Figure 2.5).

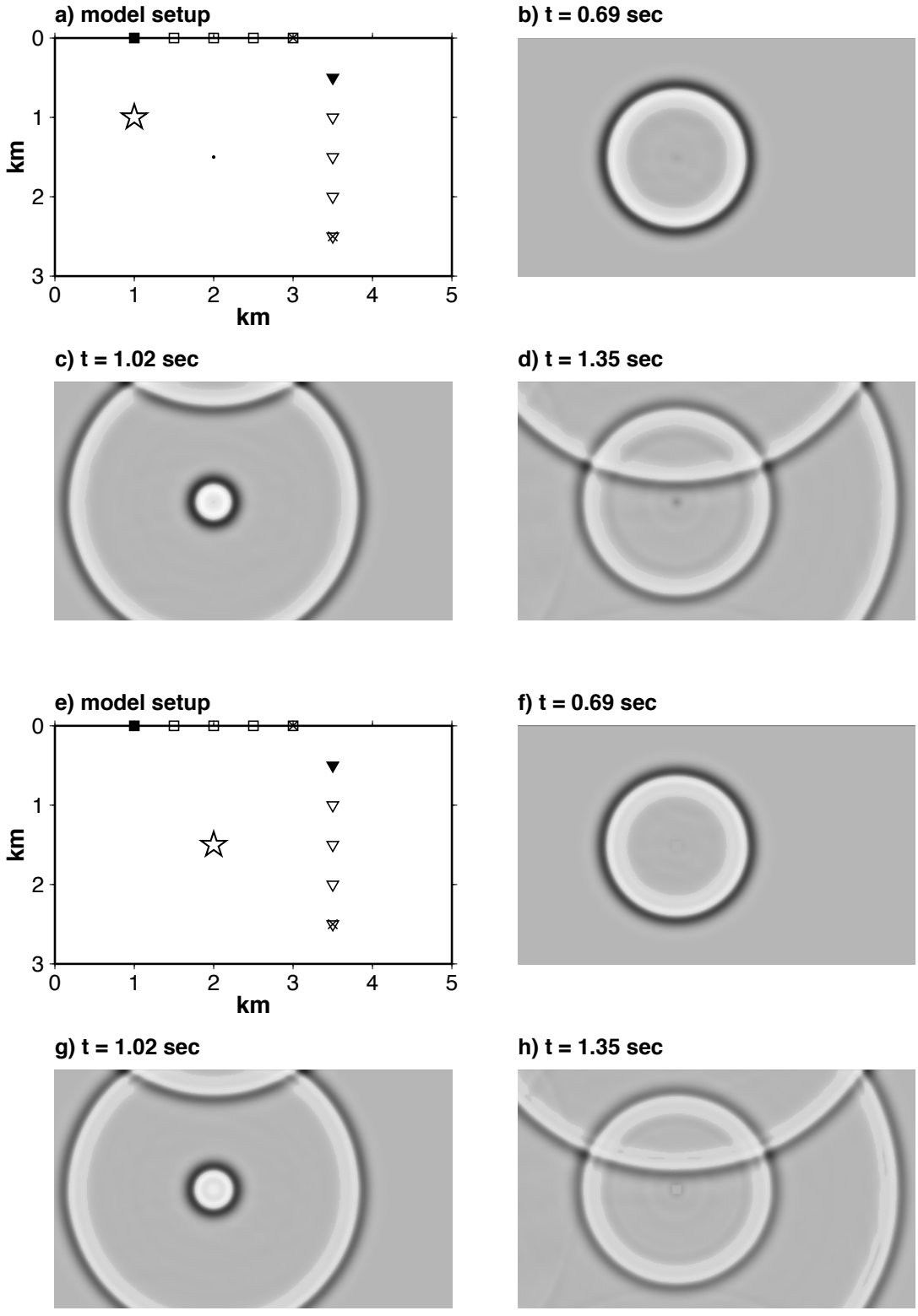

Figure 2.4. Comparisons of residual wave fields of repeated sources and wave fields from a conceptual source for a half-space model with a density of 2.6 g/cm^3, a shear

velocity of 2.85 km/s and random velocity variations of 4% with correlation lengths of 200 m in both horizontal and vertical directions. a) Model setup, repeated sources (star), location of density change (dot); the magnitude of density change is 50% between the repeated sources; b-d) snapshots of residual wave fields of the repeated sources; e) model setup for wave fields of a conceptual source situated at the location of density change (star, and the same represented by dot in a), with a strength equal to the product of density change and acceleration of the initial waves; f-h) snapshots of wave fields for the conceptual source at the same time steps in b-d). Squares and triangles in a) and e) indicate receiver locations where synthetic waveforms of two wave fields are shown in Fig. 2.5.

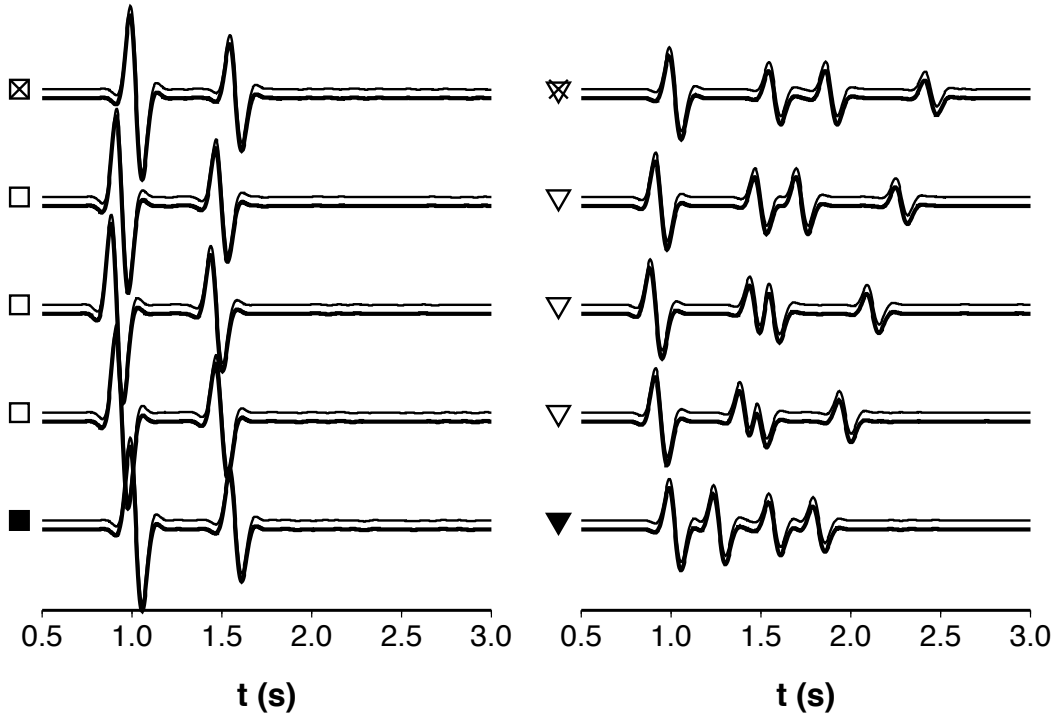

Figure 2.5. Comparisons of waveforms of difference wave fields (heavy traces) obtained for model setup in Fig. 2.4a and wave fields (light traces) generated for a conceptual source for model setup in Fig. 2.4e. Synthetic waveforms are labeled with symbols according to the receiver locations in Fig. 2.4a, 2.4e.

2.4 Application to study temporal change of seismic properties beneath the Japan subduction zone using earthquake doublet

As an example, we apply the theory to search and determine temporal change of seismic properties beneath the Japan subducution zone. Temporal seismic velocity changes are reported in the region associated with faulting and volcanic activities [*Furumoto et al.*, 2001; *Matsumoto et al.,* 2001; *Nishimura et al.,* 2005; *Rubinstein et al.,* 2007] and the region is covered by more than 700 high-resolution Hi-Net seismic stations. We will rely on earthquake doublets as sources. In the following subsections, we present doublet search, an empirical procedure for the extraction of the difference wave fields and results of inferred temporal change of seismic properties in the region.

2.4.1 Doublet search

We adopt the procedures outlined in [*Yu and Wen*, 2012] to search possible doublets in the Japan subduction zone. We briefly review the procedures here. We first group event-pairs based on the event catalog between 2004 and 2010 provided by the Incorporated Research Institutions for Seismology for events that are less than 40 km away and with a body wave magnitude larger than 4.0. We collect vertical component data for those event-pairs from the seismic stations at the Global Seismographic Network (GSN), and band-pass filter the data from 0.8 to 1.5 Hz. Waveforms are further selected based on high signal-to-noise ratios. We cross-correlate the waveforms recorded at each GSN station between possible event-pairs. Highly similar neighboring events with an average cross-correlation coefficient higher than 0.95 are selected for further event relocation.

We use the most similar and closest doublet located on the eastern coastline of Japan as repeated sources (Figure 2.6c). The doublet consists of two events occurring in 2005 and 2009 (table 2.1). The GSN recordings of this doublet constitute good azimuthal coverage for determining their relative location (Figure 2.6a, 2.6c). We employ a master event relocation method developed by *Wen* [2006] to relocate the doublet. Relative location of the doublet is determined by minimizing the RMS travel time residuals of the P or Pn phase observed at GSN stations [*Wen*, 2006]. The relocation procedures place the 2009 event 225 m east and 40 m north to the 2005 event (Figure 2.6b, 2.6d).

Table 2.1. Doublet information

Event	Date (year/mm/dd)	Origin Time (hh:mm:ss)	Latitude (^{o}N)	Longitude (^{o}E)	Magnitude (Mb)
2009 (master event)	2009/01/03	07:13:05.00	37.1270	141.0560	4.8
2005 (before relocation)	2005/09/10	20:06:50.00	37.0650	141.1850	4.7
2005 (after relocation)	2005/09/10	20:06:50.01	37.0654	141.1871	4.7

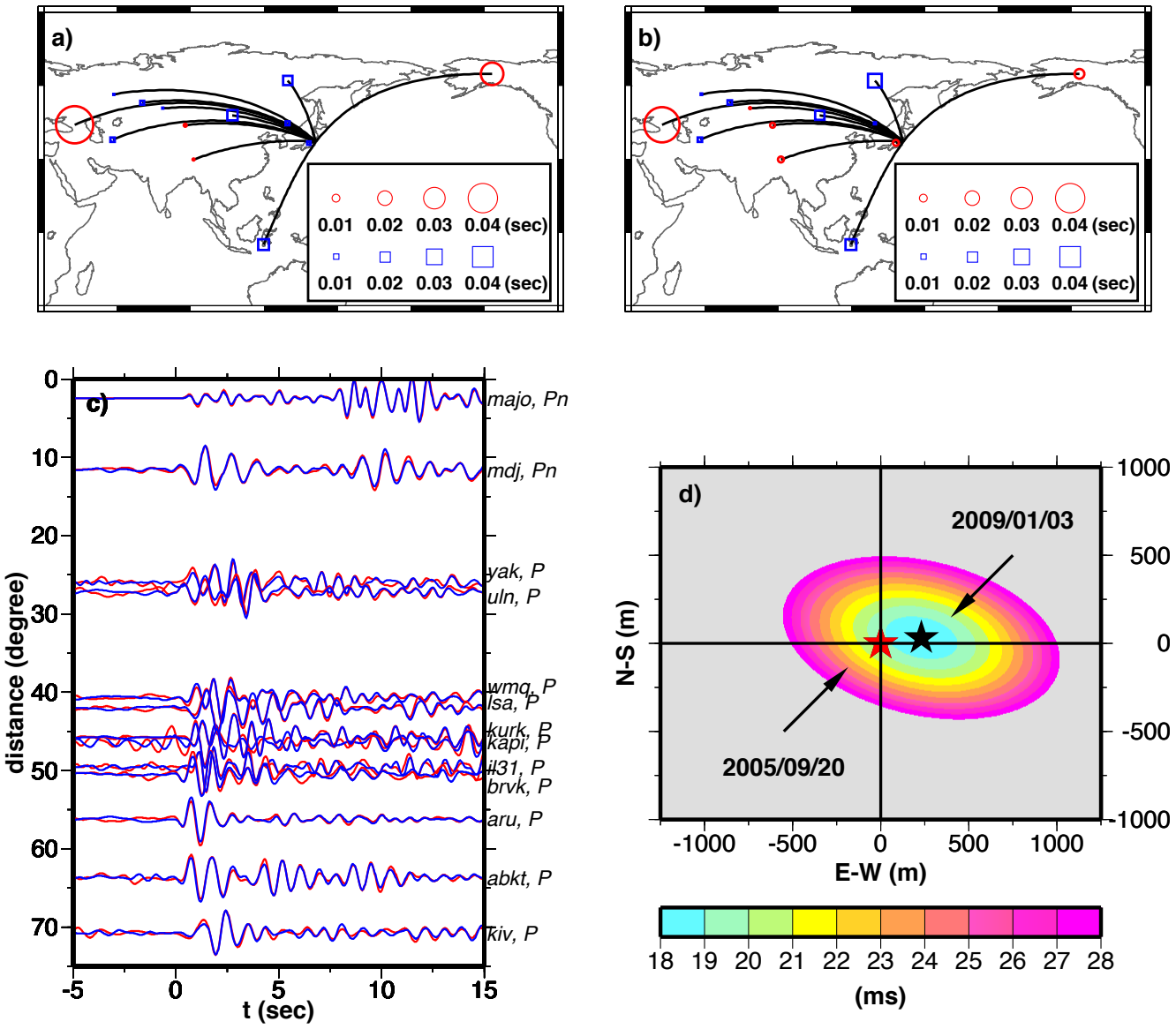

Figure 2.6. Relocation results of the 2005/09/10 and 2009/01/03 doublet. a) Measured difference in absolute arrival time (circles and squares) of P,Pn arrivals between two events, plotted centered at the location of each station, along with the great circle paths (black traces) from source to station. The arrival time differences are plotted with respect to a source origin time difference that generates a zero mean of the travel time differences for all stations. Red circles indicate that the P or Pn phase in the 2005 event arrives relatively later than in the 2009 event, while blue squares show the opposite (scale shown in the inset in the unit of sec). b) Travel time residuals between the two events after corrections using the best-fitting relative location and origin time for the 2005 event. c) Vertical components of waveform of the two events recorded at GSN stations aligned along the P,Pn arrivals, waveforms are filtered with the worldwide standard seismic network short-period instrument response and labeled

with station name and seismic phase used in the relocation. Red traces are waveforms from the 2005 event while blue traces from the 2009 event. d) Best-fitting location of the 2009 event (star) relative to the location of the 2005 event (circle) that minimizes the RMS travel time residual of the P,Pn phase observed at GSN stations shown in c). The RMS residuals larger than 28 ms are plotted as background.

2.4.2 Extraction of difference wave field

In extracting the difference wave fields resulted from the temporal change of medium, the source difference of the repeated sources has always been a challenging issue in both passive and active source experiments. To minimize the effects of source difference between the 2005 and 2009 doublet, two steps are adopted in the extraction of difference wave fields for each station between the two events. We use the observations recorded at a Hi-Net station MTDH (red triangle in Figure 2.9) as an example to illustrate the procedures (Figure 2.7).

Because we are dealing with the *SH* wave propagation, we only use the transverse components of the seismic data. We first align the waveforms of the doublet by cross-correlation and normalize the waveforms (Figure 2.7a, 2.7e). The normalization procedure is based on one event as a reference, and uses the ratio of 20-second waveform integration between the doublet to correct for amplitude difference of the other event due to the magnitude difference between the doublet at each station. We then extract difference wave fields between the doublet by weighting the subtraction of the normalized waveforms based on the cross-correlation coefficient between the doublet waveforms (Figure 2.7b – 2.7d, 2.7f – 2.7h). In this step, we

calculate cross-correlation coefficient between the doublet waveforms within a 2-second time window and move the cross-correlation time window every 0.1 s through the time series (Figure 2.7d, 2.7h). Waveform subtraction is weighted by a binary function of a value of zero for the time windows with a cross-correlation coefficient greater than a cut-off value and a value of one for other windows (Figure 2.7c, 2.7d, 2.7g, 2.7h). In another word, we only regard the difference waveforms in the de-correlated time windows (with the correlation coefficient lower than the cut-off value) as the signals resulted from temporal change of media. The difference waveforms in the correlated time windows (with correlation coefficient higher than the cut-off value) are regarded as the results from the slight differences in source radiation between the doublet. The cross-correlation coefficients are high in most of the time windows, but decrease dramatically at some time windows (Figure 2.7d). A cut-off value of 0.93 is chosen empirically in this example.

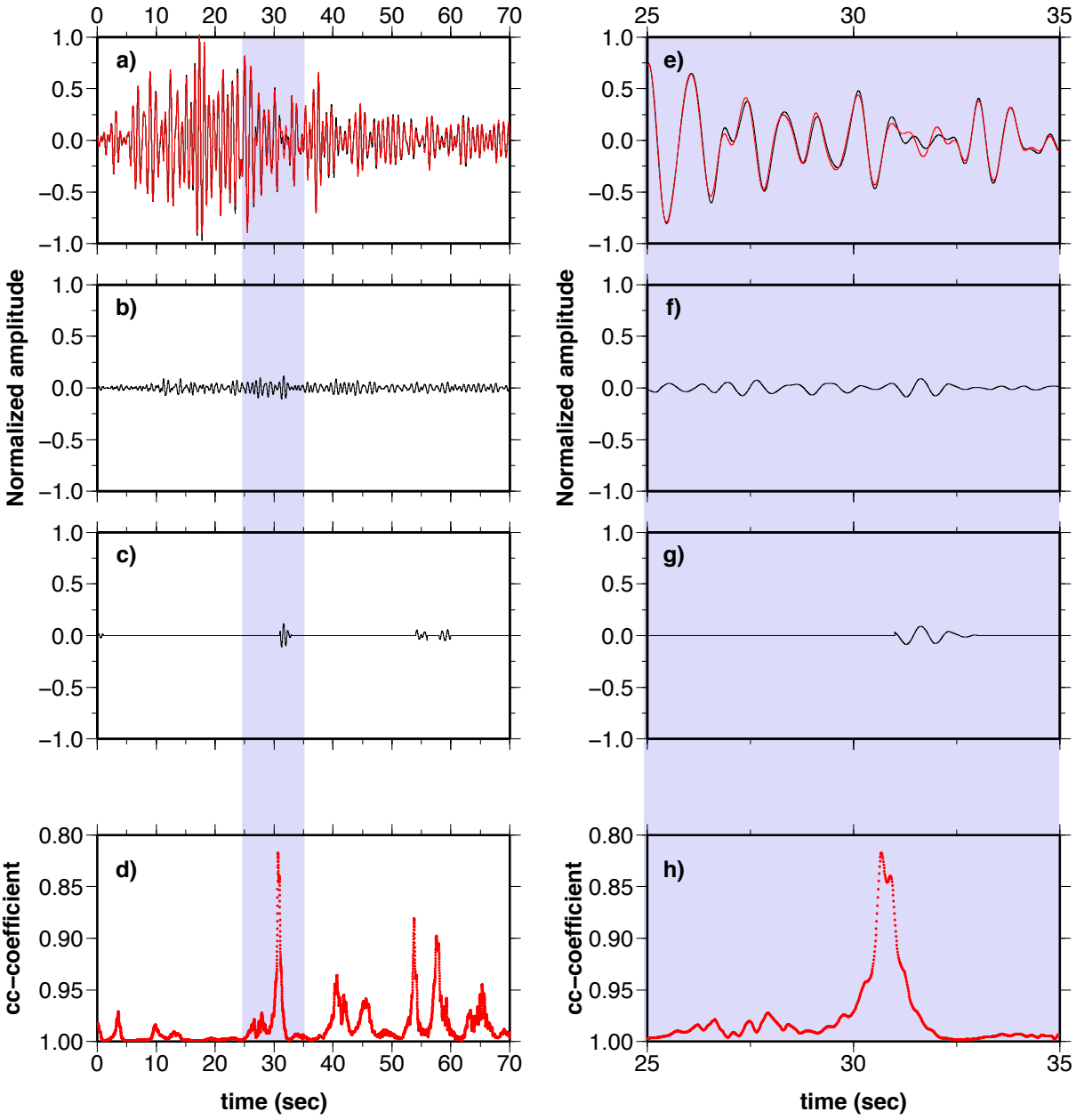

Figure 2.7. Procedures of extracting difference wave fields between the doublet, using station MTDH (noted red triangle in Figure 2.9) as an example. a) Overlap of normalized waveforms of the doublet. Waveforms are aligned based on cross-correlation and amplitudes have been normalized. b) Waveform difference obtained from the two waveforms shown in a. c) Waveform difference obtained based on a binary weighting function based on waveform cross-correlation values. d) Cross-correlation coefficients between the two waveforms in a). The moving time window for cross-correlation is 2 s, and the shifting time is 0.1 s. e)-h) are the same as a)-d), but for the time window between 25 s – 35 s, the shaded regions in a)-d).

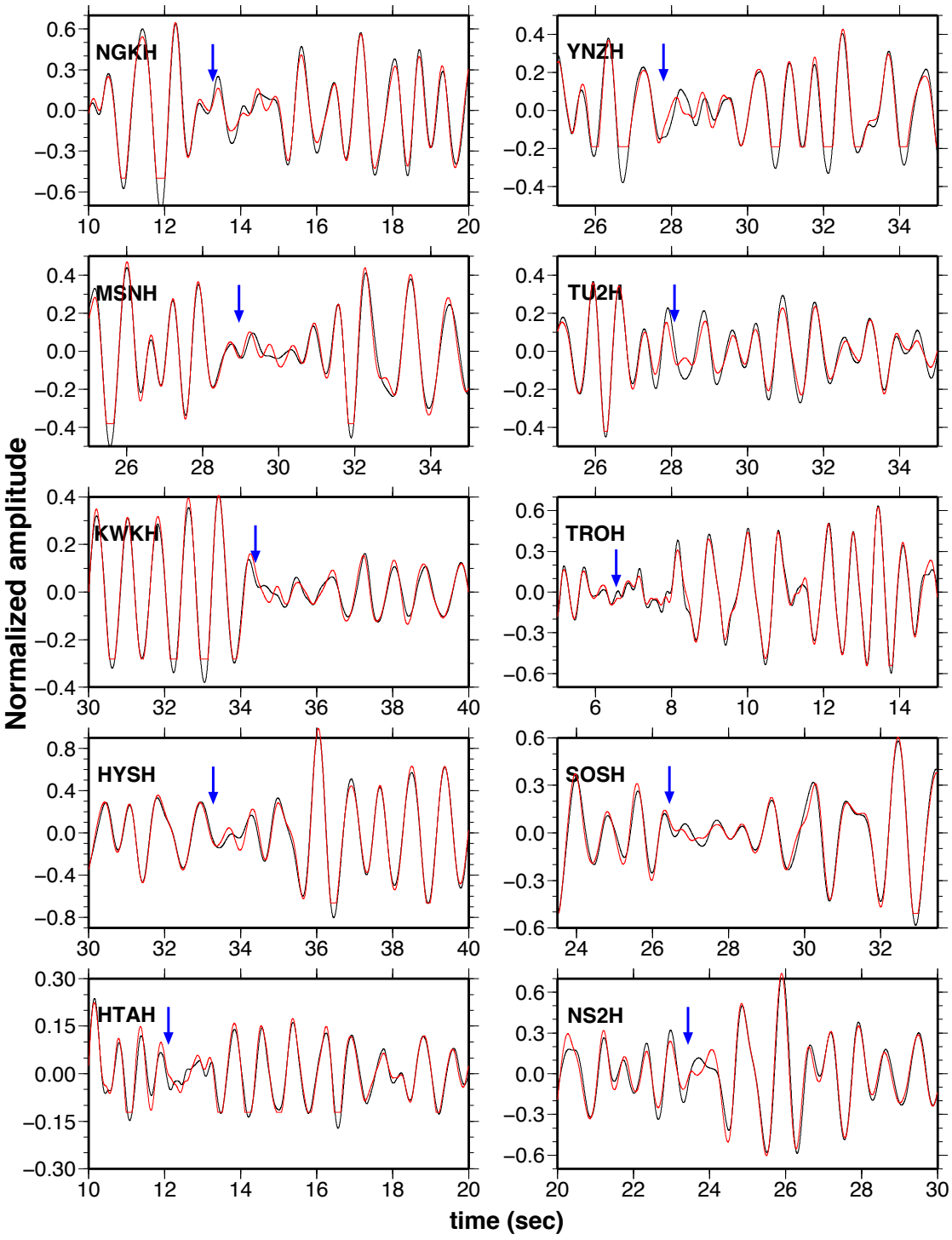

Figure 2.8. Overlap of normalized waveforms of the doublet recorded at other 10 stations (same as Figure 2.7e). Blue arrows mark the arrival times of the extracted difference wave fields signal for each station.

After these two steps, we exclude stations with the amplitude of the extracted difference wave field signal smaller than the level of the background noise, defined as the amplitude of the waveform difference of the doublet before the Pn wave. To further ensure the quality of the data, we only use those waveforms with average cross-correlation coefficient larger than 0.98 for imaging temporal medium change. Of about 700 stations in the Hi-Net, a total of 36 stations are selected based on the these selection criteria, with 19 stations on the southwest side, 9 stations on the west side and 8 stations on the northwest side (triangles, Figure 2.9). The seismic data and extracted signals at these stations have been further eye-checked for their waveform qualities (Figure 2.8). The station distribution indicates such signals are observable at large area.

2.4.3 Determination of temporal change of seismic properties

We use the observed difference *SH* wave fields to locate and quantify temporal change of seismic properties between the occurring times of the doublet. We determine the location of the temporal medium change based on the arriving times of the extracted difference signal and the magnitude of the temporal change based on the amplitudes of extracted signal and the acceleration of initial wave fields at the determined location of temporal medium change.

The conceptualization theory states that the arriving time of the signal caused by the temporal change of seismic properties at each station is the summation of the travel time from the repeated events to the location of temporal changes (the conceptual sources) and the travel time from the conceptual sources to the station.

Therefore, for a signal detected at a station, the possible conceptual sources locate at one ellipsoid-shaped surface based on the arrival time of the signal. When we have multiple stations, we can determine the location of the conceptual source, which is where those ellipsoid surfaces overlay. This back projection is implemented in the following steps, similar to those used to determine seismic scatterers in the deep mantle from PKP precursors [*Wen,* 2000; *Niu and Wen*, 2001]. For each station, we first determine its ellipsoid surface based on the station location, event location and the arrival time of the extract difference wave fields. We then assign the relative energy of the extracted difference wave fields (with respect to the maximum of the background field) to the grids of the ellipsoid surface. When multiple stations are used and their ellipsoid surfaces overlay, the projected energy is averaged. These projection steps are repeated for each assumed depth of the temporal change.

We use Preliminary Reference Earth Model (PREM) [*Dziewonski and Anderson*, 1981] to calculate the travel times and adopt a grid size of 0.2 by 0.2 degree based on the errors in predicting the Sn arrival times by PREM. The back-projection procedure places the location of temporal change at $(37.2°N, 142°E)$, where the projected energy of the difference wave fields is focused. The energy of the difference wave fields is about 3.5% relative to the main energy of the observations. Forward calculation indicates that the predicted difference wave fields travel times based on the inferred position of the temporal change are consistent with either the first or the secondary arrivals of the extracted difference wave field at those stations. Given the uncertainties of the model in predicting Sn arrival times, the uncertainty in the depth determination of the temporal change is large, between 0 and 80 km. If we assume that

the temporal changes occur at the slab interface, they should be located at 35 km depth based on the slab depth contours in the region (Figure 2.9).

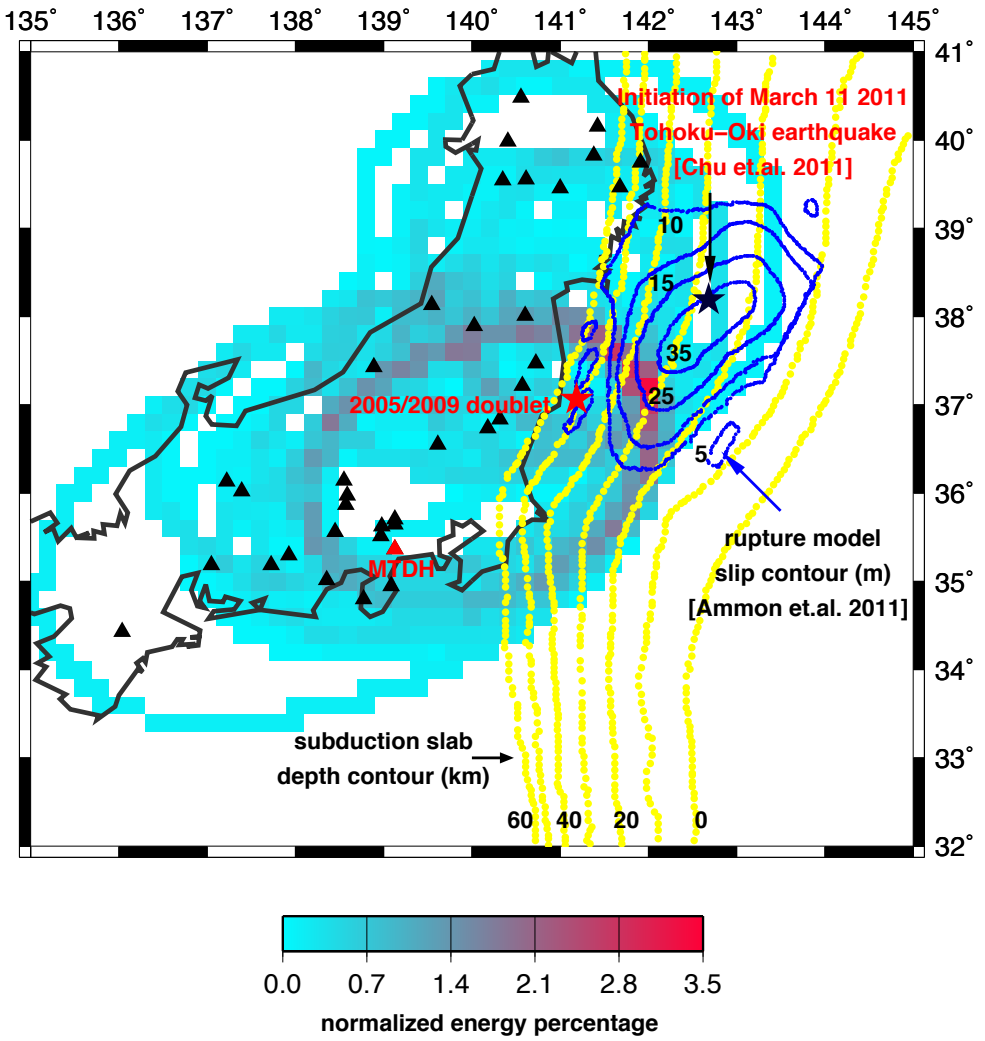

Figure 2.9. Back projected relative energy using a 0.2 degree by 0.2 degree grid size (see text for explanation). Black and red triangles represent Hi-net stations used for back projection. The projected energy is focused at (37.2°N, 142°E). Red and black stars represent the location of the 2005-2009 doublet and the initiation location of the March 11, 2011 Tohoku earthquake (Chu *et al*., 2011), respectively. Yellow lines are reconstructed subducted slab depth contours from 0-60 km (Nakajima and Hasegawa, 2006; Nakajima *et al.,* 2009). Blue lines are rupture slip contours of the March 11, 2011 Tohoku earthquake from (Ammon *et al*., 2011).

While the relative amplitudes are projected back to determine the location of temporal change, the absolute amplitude of the observed difference wave fields are used to estimate the magnitude of medium property change. The displacement generated by a single force can be expressed by:

$$U_i(\boldsymbol{x},t) = \frac{1}{4\pi\rho v^2 r}\left(\delta_{ij} - \frac{\partial r}{\partial x_i}\frac{\partial r}{\partial x_j}\right)F_j(t-\frac{r}{v}) \qquad (10)$$

where U_i is displacement in i direction, F_j body force in j direction, v velocity and r distance from the source to the receiver [Aki and Richards, 2002]. For each station, we know the amplitude of difference wave fields, U_i and the distance from the conceptual source to the station, r, so we can estimate the magnitude of the body force, F_j. When multiple stations are used, the magnitude of body force F is the average. As from equation (7), the magnitude of the conceptual source per volume is: $f = -\Delta\rho\,\frac{\partial v_o}{\partial t}|_{(x,z)=(x_c,z_c)}$, where $\Delta\rho$ is density change and $\frac{\partial v_o}{\partial t}|_{(x,z)=(x_c,z_c)}$ acceleration of the initial wave fields at the location of temporal change, and the equivalent body force $F = Vf$ with V representing the volume of the region of temporal change, the volumetric integral of density change can be estimated by equation:

$$\Delta\rho V = -F/(\frac{\partial v_o}{\partial t}|_{(x,z)=(x_c,z_c)}) \qquad (11)$$

We estimate the acceleration of the initial waves of the 2005 - 2009 doublet based on the empirical relationship of the acceleration amplitudes with distance observed in the Hi-Net stations. The accelerations of the initial wave fields $\frac{\partial v_o}{\partial t}$ decay over distance (r) following this empirical relationship: $\frac{\partial v_o}{\partial t} = 2.1\times10^{-4} * r^{-2}$ m/s^2 based on the observations in the Hi-Net stations. Thus, based on the acceleration

empirical relationship and the distance from the earthquake doublet to the location of temporal change, the acceleration at the location of the temporal change is estimated to be 3.2×10^{-4} m/s^2. The estimated magnitude of the conceptual body force associated with the temporal change of property is thus 1.15×10^{10} N. For reference, if we assume that the temporal change occurs within a volume of 10^3 km^3 and the density of oceanic crust to be 3.0 g/cm^3, the density change of the medium is estimated to be 0.87%.

The detected temporal change of medium property between 2005 and 2009 is about 125 km away from the initiation of the 11 March 2011 Tohoku-Oki earthquake [*Chu et al*., 2011] and within the rupture area of the earthquakes, as determined by many studies [*Ammon et al*., 2011; *Ide et al.,* 2011; *Yue and Lay*, 2011] (Figure 8). The timing and location of the detected temporal change may provide insights on the initiation and rupture of the large earthquake.

2.5 Discussion

Difference wave fields between earthquake doublets have been used to determine the temporal change of seismic properties in the past [e.g.,*Niu et al.*, 2003; *Taira et al.,* 2008; *Cheng et al.*, 2011]. There are similarities and differences between our study and the previous studies. In the previous studies, the difference wave fields were judged to be in existence based on cross-correlation coefficient between the doublet waveforms; the difference wave fields were projected back to possible locations of temporal changes based on their arrival times; and the length scale of the temporal change was determined based on the frequency of the difference wave fields

and the length of the time window the difference waves existed. Our identification of difference wave fields and back projection procedure are very similar to theirs. However, unlike the previous studies, which were based on just an intuitive relationship between the difference wave fields and the temporal change of medium property, our study provides a theoretical framework relating the difference wave fields to the temporal change of seismic properties. Besides locating temporal changes, our theoretical framework also illustrates how different characteristics of difference wave fields are physically related to the temporal change of seismic properties and how can those characteristics be used to quantify temporal changes of seismic properties of the medium, including their location, magnitude, volume and type of medium property change.

The doublet we used in this study has a source location separation of about 250 m. The difference wave fields we observed are unlikely due to the location difference between the doublet. A location difference of the doublet will generate a decreased cross-correlation coefficient between the waveforms of the doublet, but such decrease is independent of time base on both theory and synthetics [*Snieder et al.,* 2002; *Snieder*, 2003; *Niu et al.,* 2003]. However, our observed quick decrease of cross-correlation coefficient is only isolated in a very limited time window (Figure 2.7d, 2.7h). The characteristics of the observed cross-correlation coefficients indicates that either the waveform difference due to the location difference is small or it does not arise in the time window our difference wave fields are extracted.

The temporal changes of velocity and density are related to different types of conceptual sources and they are theoretically distinguishable based on their waveform characteristics and azimuthal variation. In our example, the complex propagation paths of the difference wave fields render it impossible to distinguish between the temporal changes of density and velocity, we have thus only considered the density change. Because of the station coverage, we are also unable to study the directivity of the difference wave fields in the data and cannot estimate the volume of the temporal change. It is hopeful that the seismic data of future simpler events or experiments in a controlled environment may be used to better constrain the volume of temporal change and separate the effects of temporal change of density from those of velocity.

2.6 Conclusions

Using *SH* elastic wave propagation as an example, we derive a theory that conceptualizes the propagation of difference wave fields of repeated sources in a temporally changed medium. We show that the *SH* difference wave fields in the changed medium could be equivalently treated as wave fields propagating from a conceptual body source and two conceptual stress perturbations located at the place of temporal medium change, with the magnitude of the conceptual body force equal to the product of density change and acceleration of the initial wave field at the location of density change, and the magnitudes of the conceptual stress perturbations equal to the product of shear modulus change and strains (displacement gradients) of the initial wave fields at the location of shear modulus change. When medium changes extend to a finite region, the conceptual sources become volumetric sources distributed over the region of the medium change and propagating in the direction of the initial wave.

The conceptualization of propagation of difference wave fields of this study indicates that the problem of locating and quantifying temporal property changes in the medium can be essentially treated as a problem of locating and quantifying the strengths of the conceptual sources using difference wave fields. When the property changes extend to a finite region, the directivity of the difference wave fields can be used to further quantify the lateral extent of the conceptualized source, and thus, of the changed medium. The conceptualization overcomes many challenging issues in the current methods for determining temporal property changes in the medium. The conceptualization makes it possible to pinpoint and quantify exact location of temporal changes inside the medium and experiment design and resolution analysis for the detection of temporal medium change straightforward.

As an example of application, we apply the theory to locate and quantify temporal change of seismic properties beneath the Japan subduction zone using an earthquake doublet as sources. We develop an empirical procedure to extract the *SH* component difference wave fields from the Hi-Net stations, which includes weighting the subtraction of the normalized waveforms between the doublet by a binary function based on cross-correlation coefficients between the waveforms. We detect temporal change of medium properties in the region and determine the location of the temporal change to be at $(37.2°N, 142°E)$ based on the arrival times of the difference wave fields using a back-projection method. Based on the amplitudes of the extracted difference signal and the acceleration of the background wave fields, we estimate the magnitude of the conceptual body force associated with the temporal change is 1.15×10^{10} N, or, as a reference, a 0.87% density change, assuming that the temporal

change occurs within a volume of 10^3 km^3. The detected temporal change of medium property between 2005 and 2009 is about 125 km away from the initiation of the 11 March 2011 Tohoku-Oki earthquake [*Chu et al*., 2011] and within the rupture area of the earthquakes

2.7 References

Aki, K., and P. G. Richards (2002), Elastic waves from a point dislocation source, in *Quantitative seismology (Second Edition)*, edited by J. Ellis, pp. 63-117, University Science Books, Sausalito, Calif.

Ammon, C. J., T. Lay, H. Kanamori and M. Cleveland (2011), A rupture model of the great 2011 Tohoku earthquake, *Earth Planets Space,* 63, 693-696.

Baisch, S. and G. H. R. Bokelmann (2001), Seismic waveform attributes before and after the Loma Prieta earthquake: Scattering change near the earthquake and temporal recovery, *J. Geophys. Res., 106***,** 16,323-16,337.

Bokelmann, G. H. R. and H. P. Harjes (2000), Evidence for temporal variation of seismic velocity within the upper continental crust, *J. Geophys. Res., 105***,** 23,879-23,894.

Bonnin, P., H. Debbabi, J. Mariani, C. Charriaut-Marlangue and S. Renolleau (2008), Ultrasonic assessment of cerebral blood flow changes during ischemia-reperfusion in 7-day-old rats, *Ultrasound Med. Biol., 34***,** 913-922.

Brenguier, F., N. M. Shapiro, M. Campillo, V. Ferrazzini, Z. Duputel, O. Coutant and A. Nercessian (2008a), Towards forecasting volcanic eruptions using seismic noise, *Nat. Geosci., 1***,** 126-130.

Brenguier, F., M. Campillo, C. Hadziioannou, N. M. Shapiro, R. M. Nadeau and E. Larose (2008b), Postseismic relaxation along the San Andreas Fault at Parkfield from continuous seismological observations, *Science, 321*, 1478-1481.

Cao, A., Y. Masson and B. Romanowicz (2007), Short wavelength topography on the inner-core boundary, *P. Natl. Acad. Sci. USA, 104***,** 31-35.

Cheng, X., F. Niu, P. G. Silver and R. M. Nadeau (2011), Seismic Imaging of Scatterer Migration Associated with the 2004 Parkfield Earthquake Using Waveform Data of Repeating Earthquakes and Active Sources, *Bull. Seismol. Soc. Am., 101***,** 1291-1301.

Chu, R., S. Wei, D. V. Helmberger, Z. Zhan, L. Zhu and H. Kanamori (2011), Initiation of the great Mw 9.0 Tohoku-Oki earthquake, *Earth Planet. Sci. Lett.*, *308*, 277-283.

Dziewonski, A.M. and D. L. Anderson (1981), Preliminary reference Earth model, *Phys. Earth Planet In., 25***,** 297-356.

Els, T., M. Daffertshofer, H. Schroeck, W. Kuschinsky and H. Hennerici (1999), Comparison of transcranial Doppler flow velocity and cerebral blood flow during focal ischemia in rabbits, *Ultrasound Med. Biol., 25***,** 933-938.

Furumoto, M., Y. Ichimori, N. Hayashi, Y. Hiramatsu and T. Satoh (2001), Seismic wave velocity changes and stress build-up in the crust of the Kanto-Tokai region, *Geophys. Res. Lett., 28***,** 3737-3740.

Gret, A., R. Snieder and J. Scales (2006), Time-lapse monitoring of rock properties with coda wave interferometry, *J. Geophys. Res., 111,* B03305, doi:10.1029/2004JB0003354.

Ide, S., A. Baltay, and G. C. Beroza (2011), Shallow Dynamic Overshoot and Energetic Deep Rupture in the 2011 M(w) 9.0 Tohoku-Oki Earthquake, *Science, 332***,** 1426-1429.

Ikuta, R. and K. Yamaoka (2004), Temporal variation in the shear wave anisotropy detected using the Accurately Controlled Routinely Operated Signal System (ACROSS), *J. Geophys. Res., 109,* B09305, doi:10.1029/2003JB002901.

Li, L., Z. Ke, K. Tong and M. Ying (2010), Evaluation of cerebral blood flow changes in focal cerebral ischemia rats by using transcranial Doppler ultrasonography, *Ultrasound Med. Biol., 36***,** 595-603.

Li, Y., J. E. Vidale, K. Aki, F. Xu and T. Burdette (1998), Evidence of shallow fault zone strengthening after the 1992 M7.5 Landers, California, Earthquake, *Science, 279***,** 217-219.

Li, Y., P. Chen, E. S. Cochran and J. E. Vidale (2007), Seismic velocity variations on the San Andreas fault caused by the 2004 M6 Parkfield Earthquake and their implications, *Earth Planets Space, 59***,** 21-31.

Lumley, D. E. (2001), Time-lapse seismic reservoir monitoring, *Geophysics, 66***,** 50-53.

Martini, F., C. J. Bean, G. Saccorotti, F. Viveiros and N. Wallenstein (2009), Seasonal cycles of seismic velocity variations detected using coda wave interferometry at Fogo volcano, Sao Miguel, Azores, during 2003-2004, *J. Volcanol Geoth. Res., 181***,** 231-246.

Matsumoto, S., K. Obara, K. Yoshimoto, T. Saito, A. Ito and A. Hasegawa (2001), Temporal change in P-wave scatterer distribution associated with the M6.1 earthquake near Iwate volcano, northeastern Japan, *Geophys. J. Int., 145***,** 48-58.

Nakajima, J. and A. Hasegawa (2006), Anomalous low-velocity zone and linear alignment of seismicity along it in the subducted Pacific slab beneath Kanto, Japan: Reactivation of subducted fracture zone?, *Geophys. Res. Lett.*, *33,* L16309, doi: 10.1029/2006GL026773.

Nakajima, J., F. Hirose and A. Hasegawa (2009), Seismotectonics beneath the Tokyo metropolitan area, Japan: Effect of slab-slab contact and overlap on seismicity, *J. Geophys. Res.,* 114, B08309, doi: 10.1029/2008JB006101.

Nishimura, T., S. Tanaka, T. Yamawaki, H. Yamamoto, T. Sano, M. Sato, H. Nakahara, N. Uchida, S. Hori and H. Sato (2005), Temporal changes in seismic velocity of the crust around Iwate volcano, Japan, as inferred from analyses of repeated active seismic experiment data from 1998 to 2003, *Earth Planets Space, 57***,** 491-505.

Niu, F., P.G. Silver, R.M. Nadeau, and T.V. McEvilly (2003), Stress-Induced Migration of Seismic Scatterers Associated with the 1993 Parkfield Aseismic Transient Event, *Nature*, *426*, 544-548.

Niu, F., P. G. Silver, T. M. Daley, X. Cheng and E. L. Majer (2008), Preseismic velocity changes observed from active source monitoring at the Parkfield SAFOD drill site, *Nature, 454***,** 204-U244.

Niu, F. and L. Wen (2001), Strong seismic scatterers near the core-mantle boundary west of Mexico, *Geophys. Res. Lett., 28***,** 3557-3560.

Peng, Z.G. and Y. Ben-Zion (2006), Temporal changes of shallow seismic velocity around the Karadere-Duzce branch of the North anatolian fault and strong ground motion, *Pure Appl. Geophys., 163***,** 567-600.

Poupinet, G., W. L. Ellsworth and J. Frechet (1984), Monitoring velocity variations in the crust using earthquake doublets: An application to the Calaveras Fault, California, *J. Geophys. Res., 89*, 5719-5731.

Rickett, J. E. and D. E. Lumley (2001), Cross-equalization data processing for time-lapse seismic reservoir monitoring: A case study from the Gulf of Mexico, *Geophysics, 66*, 1015-1025.

Rubinstein, J. L., N. Uchida and G. C. Beroza (2007), Seismic velocity reductions caused by the 2003 Tokachi-Oki earthquake, *J. Geophys. Res., 112*, B05315, doi:10.1029/2006JB00440.

Santos, E. T. F. and J. M. Harris (2009), DynaSIRT: A robust dynamic imaging method applied to CO2 injection monitoring, *SEG Expanded Abstract, 28*, 4019.

Schaff, D. P. and G. C. Beroza (2004), Coseismic and postseismic velocity changes measured by repeating earthquakes, *J. Geophys. Res., 109*, B10302, doi:10.1029/2004JB003011.

Sens-Schonfelder, C. and U. Wegler (2006), Passive image interferometry and seasonal variations of seismic velocities at Merapi Volcano, Indonesia, *Geophys. Res. Lett., 33*, L21305, doi:10.1029/2006GL027797.

Snieder, R., A. Gret, H. Douma and J. Scales (2002), Coda wave interferometry for estimating nonlinear behavior in seismic velocity, *Science, 295*, 2253-2255.

Snieder, R., (2006), The theory of coda wave interferometry, *Pure Appl. Geophys., 163*, 455-73.

Snieder, R., S. Hubbard, M. Haney, G. Bawden, P. Hatchell, A. Revil and D. G. M. Working (2007), Advanced noninvasive geophysical monitoring techniques, *Annu. Rev. Earth Planet. Sci., 35*, 653-683.

Taira, T., P. G. Silver, F. Niu, and R. M. Nadeau (2008), Detecting seismogenic stress evolution and constraining fault zone rheology in the San Andreas Fault following the 2004 Parkfield earthquake, *J. Geophys. Res., 113*, B03303, doi:10.1029/2007JB005151.

Vidale, J. E. and Y. Li (2003), Damage to the shallow Landers fault from the nearby Hector Mine earthquake, *Nature, 421***,** 524-526.

Wegler, U. and C. Sens-Schonfelder (2007), Fault zone monitoring with passive image interferometry, *Geophys. J. Int., 168***,** 1029-1033.

Wen, L. (2000), Intense seismic scattering near the Earth's core-mantle boundary beneath the Comoros hotspot, *Geophys. Res. Lett., 27***,** 3627-3630.

Wen, L. (2002), An SH hybrid method and shear velocity structures in the lowermost mantle beneath the central Pacific and South Atlantic Oceans, *J. Geophys. Res., 107*, 2055, doi:10.1029/2001JB000499.

Wen, L. (2006), Localized temporal change of the earth's inner core boundary, *Science, 314***,** 967-970.

Young, R. P. and D. S. Collins (2001), Seismic studies of rock fracture at the Underground Research Laboratory, Canada, *Int. J. Rock Mech. Min., 38***,** 787-799.

Yu, W. and L. Wen (2012), Deep-focus repeating earthquakes in the Fiji-Tonga subduction zone, *Bull. Seis. Soc. Am., 102,* 1829-1849.

Yue, H. and T. Lay (2011), Inversion of high-rate (1sps) GPS data for rupture process of the 11 March 2011 Tohoku earthquake (Mw 9.1), *Geophys. Res. Lett., 38,* L00G09, doi:10.1029/2011GL048700.

Zhang, J., X. Song, Y. Li, P. G. Richards, X. Sun and F. Waldhauser (2005), Inner core differential motion confirmed by earthquake waveform doublets, *Science, 309*, 1357-1360

Zhang, J., P. G. Richards and D. P. Schaff (2008), Wide-scale detection of earthquake waveform doublets and further evidence for inner core super-rotation, *Geophys. J. Int., 174*, 993-1006.

Zhao, P. and Z. Peng (2009), Depth extent of damage zones around the central Calaveras fault from waveform analysis of repeating earthquakes, *Geophys. J. Int.*, *179,* 1817-1830.

Chapter 3

Detailed Shear Wave Low Velocity Features in the Mid-lower Mantle Beneath Central America

3.1 Abstract

Tangential shear wave seismic observations of South American earthquakes recorded at USArray stations between 2011 and 2013 are used to place constraints on the detailed mid-lower mantle structure beneath Central America. Waveform observations sampling the center of our study region show complex reflection phases, which exhibit significant variations with azimuth and distance. Travel time analyses show increasing S wave residuals of up to 9 seconds as distance increases from 45° to 80°. Forward waveform and travel time modeling reveals that several sub-horizontal 10-20 km thick segments with –10% velocity perturbation are buried inside a "trapezoid-like" low velocity region with –2% velocity perturbation extending between 1000 and 2750 km depth. This low velocity anomaly is located at the west of a high velocity anomaly, which is believed to be the ancient Farallon subduction slab. The geometry and velocity features of the "trapezoid-like" anomaly show some similarities with the mid-lower mantle structure beneath Africa and the Pacific. This low velocity anomaly structure could be a locally chemically distinct province or driven by mantle convection, with partial melting inside.

3.2 Introduction

The North and Central America region is well known for over 150 million years of subduction history, which generates complex wave velocity structures. Back to the 90s, global travel time tomography studies from P wave [*van der Hilst, et. al., 1997*] and S wave [*Grand, 1994*] both showed the existence of high-velocity anomalies extending eastward to the lower-most mantle in this region, which was interpreted as the subduction of ancient Farallon plate [*Grand et. al., 1997; Yoshio et. al., 2001*]. Later studies revealed more detailed features such as the breaking of the Farallon plate and two-state subduction [*e.g. Lithgow-Bertelloni and Richards, 1998; Ren et. al., 2007; Sigloch et. al., 2008; Liu and Stegman, 2011*], though the main features remained consistent. Detailed crustal and upper mantle structures were studied extensively using various methods [e.g. Lin et. al., 2008; Grand and Helmberger, 1984; Obrebsi et. al., 2011; Sun and Helmberger, 2011; van der Lee and Frederiksen, 2013; van der Lee and Nolet, 1997]. Also, various studies had focused on the lower-most mantle structures [*e.g. Garnero and Lay, 2003; Hutko et. al., 2006; Lay and Helmberger, 1983; Miller and Niu, 2008; Sun et. al., 2006; Thomas et. al., 2004; Wysession et. al., 2001*], which showed a complex high velocity anomaly above the core-mantle boundary. By contrast, studies targeting the detailed mid-lower mantle structures were much less. Small-scale shear wave anomalies at depths between 1380 km and 1800 km [*Courtier and Revenaugh, 2008; Kaneshima and Helffrich, 2010*] had been detected by multiple ScS reverberationa and S-to-P scattered waves, and were interpreted as slab debris or chemical heterogeneity. A few studies had noticed a large-scale slow blanket at the east side of the subducted Farallon slab [*van der Lee et.*

al., 2008; Sigolch 2011], yet the nature of the low velocity anomalies is still mysterious.

Outside of the Americas region, investigations about velocity anomalies in the mid to lower mantle have revealed several key features. Studies had shown that two of the most prominent low velocity provinces were located below the Pacific and Africa [*e.g. Su et al., 1992; Grand et al., 1997; van der Hilst et al., 1997; Ritsema et al., 1999*], which extended hundreds of kilometers into the mid-lower mantle with possible sharp edges [*e.g. He and Wen, 2012; Ni et. al., 2002; Wang and Wen, 2007; Tanaka et. al., 2009; To et. al., 2005*]. Also small-scale scatterers or reflectors had been detected by using S-to-P converted phase [*Kaneshima and Helffrich, 1999; Kaneshima and Helffrich, 2010; Kawakatsu and Niu, 1994; Li and Yuen, 2014; Niu and Kawakatsu, 1997; Niu et. al., 2003; Vanacore et. at., 2006; Vinnik et al., 2001*], multiple ScS reverberationa [*Bagley et. al., 2013*], receiver function [*Shen et. al., 2003; Vinnik et. al., 2010*], SS, PP and P'P' precursors [*Deuss, 2009; Sebastian et. a., 2008; Stunff et. at., 1995*]. Most of the detected scatterers and reflectors are located at the depth between 750km and 1800km beneath circum-Pacific region with velocity perturbations as large as 6% [*Kaneshima, 2013*].

Thus, it's intriguing to study and understand the extent and velocity contrast of the mid-lower mantle low velocity structures beneath Central America. Of particular interests are the similarities and dissimilarities of the mid-lower mantle low velocity structures between different regions, which might shed some light on mantle dynamics and evolution. In this chapter, we use seismic waveform and travel time observations

and forward modeling to study the detailed shear wave low-velocity features in the mid-lower mantle beneath Central America.

Table 3.1. Event List

Event Date	Origin Time	Latitude($^{\circ}N$)	Longitude($^{\circ}E$)	Depth(km)
Group one:				
2012/11/14	19:02:06.0	-29.118	-71.190	63
2011/09/02	13:47:09.0	-28.398	-63.029	578.9
2012/05/28	05:07:23.0	-28.043	-63.094	586.9
2013/02/22	12:01:58.0	-27.932	-63.097	575.2
Group two:				
2012/11/22	13:07:10.0	-22.742	-63.571	516.6
2012/10/08	01:50:26.0	-21.725	-68.165	122
2011/06/20	16:36:01.0	-21.701	-68.22	128
2013/07/10	14:32:13.0	-19.23	-69.172	110
Group three:				
2012/05/14	10:00:40.0	-17.678	-69.591	105.9
2011/06/08	03:06:22.0	-17.083	-69.518	145.7
2011/11/22	18:48:16.0	-15.362	-65.087	549.9
2012/07/02	23:31:37.0	-14.423	-75.597	39.6
Group four:				
2012/08/02	09:38:31.0	-8.379	-74.245	143.3
2011/08/24	17:46:11.0	-7.641	-74.525	147
2011/11/17	01:57:05.0	-1.702	-81.546	26.6

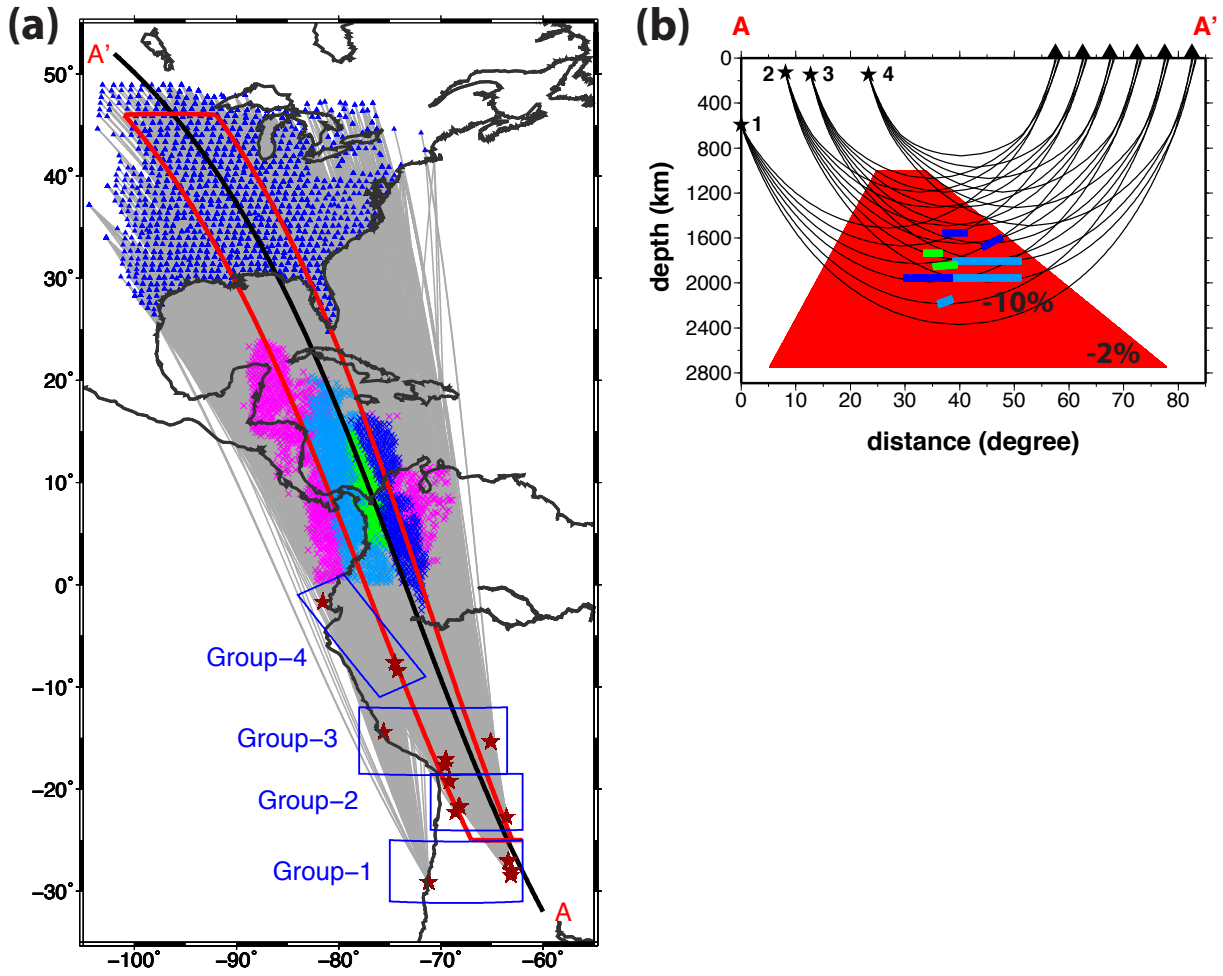

Figure 3.1. (a) Seismic data coverage map with great circle paths (gray lines) from South America seismic events (red stars) to USArray stations (blue triangles). Colored crosses mark the S wave turning points sampling different sections of the region. Waveform observations sampling sections marked with purple crosses show no or little waveform complexity, and waveform observations sampling sections marked with turquoise, green and blue crosses show distinctly different secondary reflection features after S arrival. Red box marks the region with -2% shear wave velocity perturbation in the mid-lower mantle based on S and ScS travel time analyses. AA' is the cross-section sampled in this study. Seismic events are divided into four groups by event latitude as shown in table 3.1 and marked as blue boxes. (b) Shear wave velocity structure beneath the red box in (a) with S wave ray-path along the cross-section. The turquoise, green and blue segments are 10-20 km thick segments with –10% shear wave velocity perturbation beneath the turquoise, green and blue sections correspondingly. The red region is a "trapezoid-like" low velocity region with –2% shear wave velocity perturbation extending between 1000 and 2750 km depth beneath the red box in (a).

3.3 Data and study region

Four groups of South American earthquakes occurred between 2011 and 2013 (Table 3.1) and recorded at USArray stations are collected based on sampling distance and high signal to noise ratio. Tangential seismograms are band-pass filtered between 0.1 – 1 Hz, and arrival times are hand picked. The collected seismic observations sample a large distance ranging between 35° and 82° and provide a good sampling coverage in the mid-lower mantle beneath Central America (Figure 3.1).

3.4 Seismic waveform observations and modeling

3.4.1 Detailed waveform observations

All seismic waveforms are aligned by hand picked S and ScS arrivals, and compared based on azimuth and distance coverage. We notice distinct reflection features. In general, one or multiple additional phases are observed to arrive after the S phase arrival (Figure 3.2 and 3.3). These additional secondary phases first gradually migrate closer to the S arrival at shorter distance range and then migrate away from the S arrival at larger distance range. However, strong variations with sampling azimuth and distance do exist for the secondary reflection phases. The detailed features of each waveform profile are quite unique in terms of the merging distance, move-out rate, and distance window of observable secondary phases.

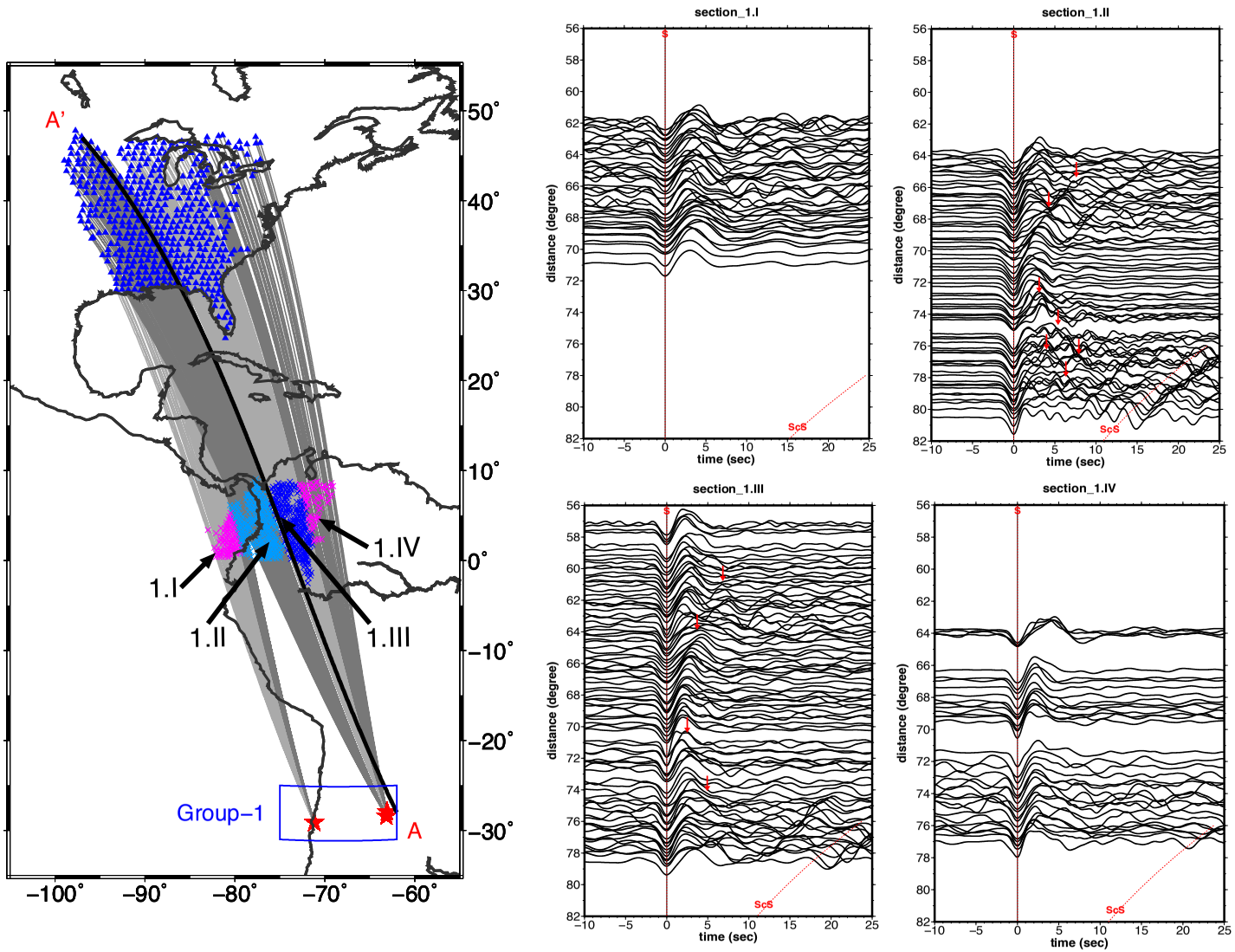
A'
A
Group−1
1.I
1.II
1.III
1.IV
50°
40°
30°
20°
10°
0°
−10°
−20°
−30°
−100°
−90°
−80°
−70°
−60°
section_1.I
section_1.II
section_1.III
section_1.IV
distance (degree)
time (sec)
S
ScS

Figure 3.2. (a)

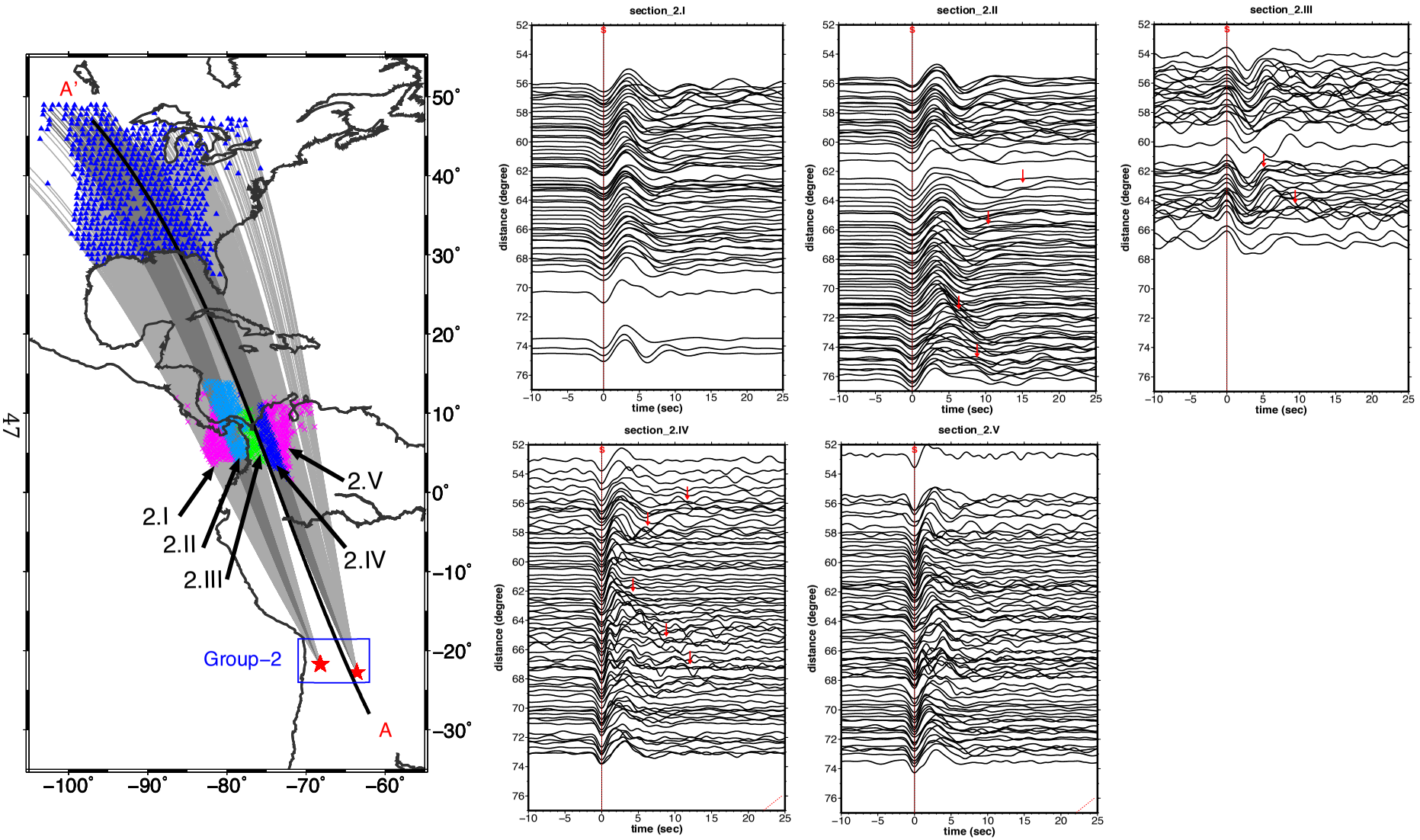
A'
A
Group–2
2.I
2.II
2.III
2.IV
2.V
50°
40°
30°
20°
10°
0°
–10°
–20°
–30°
–100°
–90°
–80°
–70°
–60°
47
section_2.I
section_2.II
section_2.III
section_2.IV
section_2.V
distance (degree)
time (sec)

Figure 3.2. (b)

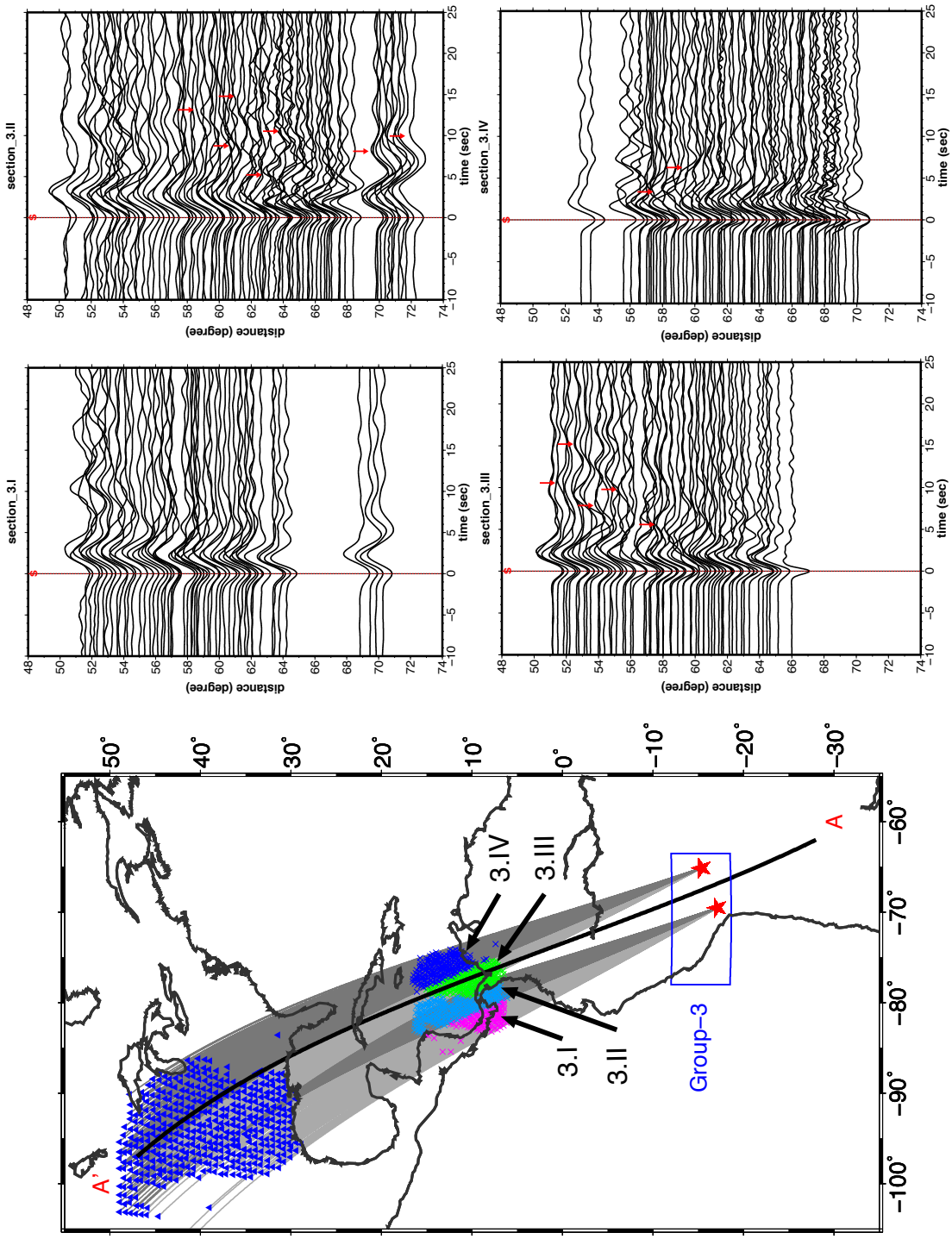

Figure 3.2. (c)

Figure 3.2. Observed seismic waveforms aligned by the S phase arrival sampled by events from Group 1, 2 and 3. Based on waveform differences, each sampling region can be divided into several sub-sections (one turquoise, one green, one blue and two purple sections). Red arrows mark the observed secondary reflection phases.

Based on similarities of waveform features, we are able to divide our study region into five azimuthal sub-sections, one turquoise, one green, one blue and two purple sections (Figure 3.1 and 3.2). The reflection features only exist when sampling the center of our study region (sections marked with turquoise, green and blue crosses in Figure 3.2). Let's take waveform observations sampled by events from Group 1 for example, which have similar coverage in terms of distance (Figure 3.2.a). The observations sampling in the turquoise and blue sections show strong secondary reflection phases; the observations sampling in the two purple sections show no sign of secondary reflection phase. However, the distance window and the merging distance of the observed secondary phases are different between the turquoise and blue sections. Waveform observations sampling in the turquoise section show one phase merging faster to the S arrival before 70° and multiple phases merging away from the S arrival beyond 72°; whereas waveform observations sampling in the blue section show only one phase merging slower to the S arrival before 68° and away from the S arrival beyond that. Azimuthal differences are observed between waveform observations sampled by events from Group 2 (Figure 3.2.b) and Group 3 (Figure 3.2.c) as well.

When the same azimuth section is sampled by different events with varied distance coverage, the reflection features are also different. One example is shown in Figure 3.3. Though all profiles are sampling in the turquoise section, the event from Group 1 samples deeper and the most southern part of the mid-lower mantle, and the event from Group 4 samples shallower and the most northern part of the mid-lower mantle. The secondary reflection features change as the event moving between Group

1, 2 and 3. We note that the event from Group 2 has a much broader source time function that would flatten and weaken the reflection features. The complex secondary reflection features disappear when the sampling event is from Group 4. One phase has about 18s of constant delay with the S arrival when the sampling event is from Group 4. Because the reflection phase from the other waveform profiles normally have a move out when the seismic waveforms are aligned by the S arrival, this observed phase does not fit the other profiles and is likely caused by the upper mantle and crust structures. Distance dependent changes in reflection features are observed for green and blue sections as well.

The complex reflection features are only found after the S arrival. Seismic waveforms following the ScS arrival show no sign of a secondary phase. One example of seismic waveforms aligned by the ScS phase is presented in Figure 3.4. The same waveform aligned by the S arrival is shown previously in Figure 3.2.(a) and 3.3. The clear differences indicate that our observed complex waveform features are likely caused by the mid-lower mantle structure, and not by source or receiver side shallow structures.

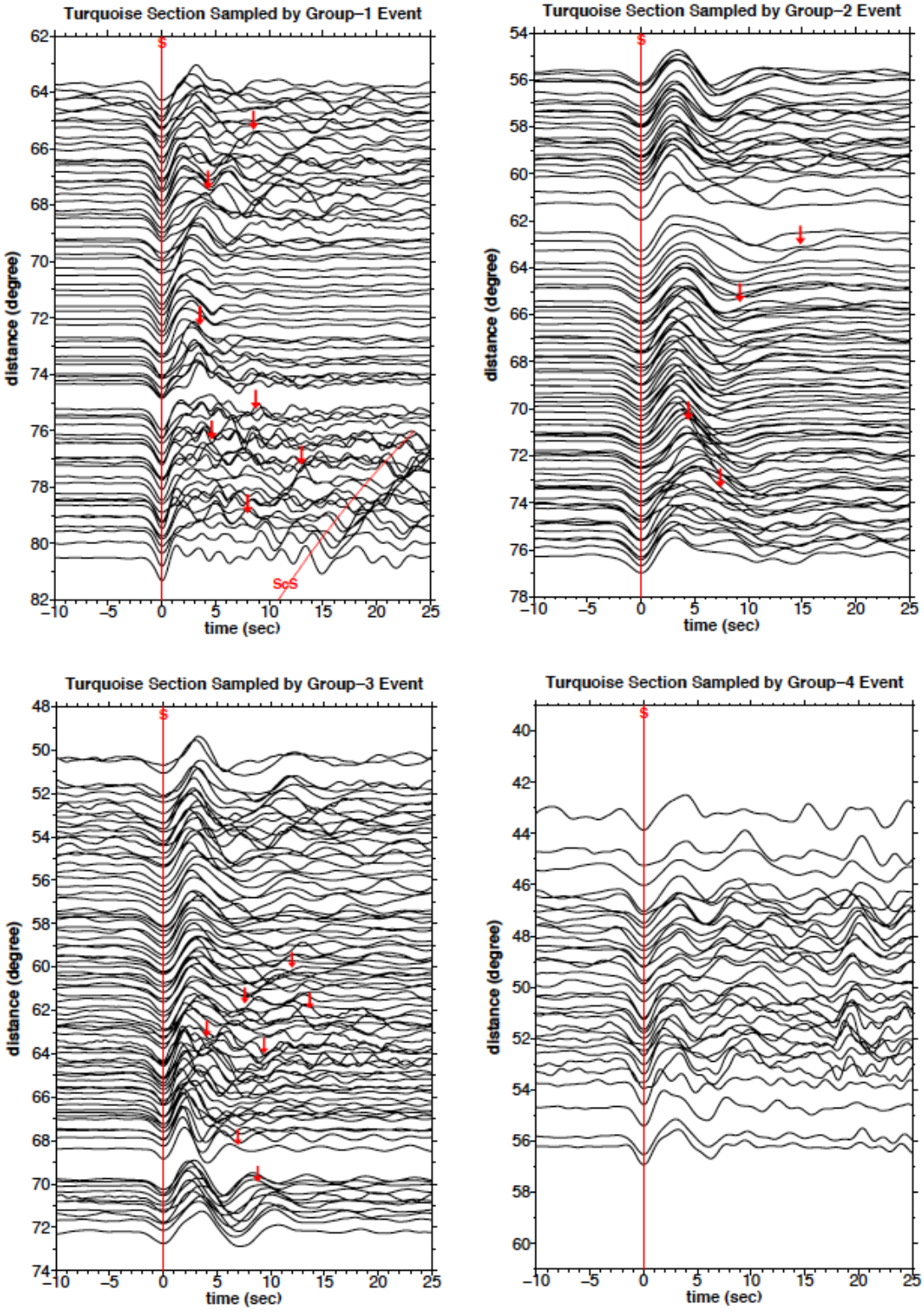

Figure 3.3. Observed seismic waveforms aligned by the S phase arrival in turquoise section sampled by events from Group 1, 2, 3 and 4. Red arrows mark the observed secondary reflection phases.

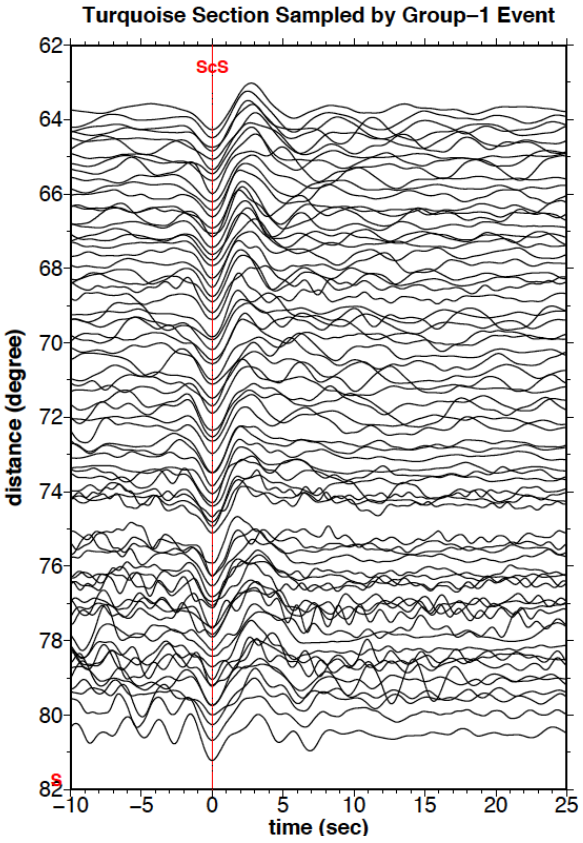

Figure 3.4. One example of observed seismic waveform observations aligned by the ScS phase arrival. No secondary reflection phase is observed after ScS arrival.

3.4.2 Waveform modeling benchmark

Extensive waveform modeling shows that the characteristics of synthetic reflection waveforms generated by the abnormal velocity segment are controlled by several key parameters, including amplitude of velocity contrast, thickness, depth, horizontal dimension and location, dipping angle, and number of the segments. We demonstrate the effects of these controlling parameters in the following bench tests. All waveform and travel time modeling in this study use a *SH* hybrid method developed by *Wen [2002]*. The *SH* hybrid method combines Generalized Ray Theory (GRT), Finite Difference (FD) and Kirchhoff Theory. It assumes an Earth flattening approximation. The input velocity model includes two parts: a 2-D velocity model in a

certain region, defined as heterogeneous region, and a 1-D velocity model outside of this region.

Segments with low and high velocity anomalies would both generate a reflective secondary phase after the S arrival. However, the secondary phase generated by a segment with high velocity anomalies has the same polarity as the S phase, and disappears beyond the distance range where the S turning depth is deeper than the location depth of the segment; the secondary phase generated by a segment with low velocity anomalies has the opposite polarity as the S phase, and is still visible but migrates away from the S arrival beyond the distance range where the S turning depth is deeper than the location depth of the segments (around 75° in Figure 3.5). The waveforms generated by a segment with low velocity anomalies are more compatible with the observations.

The amplitude of the velocity contrast affects the amplitude, width and arrival time of the secondary reflection phase. When the amplitude of the velocity contrast is less than 3%, the secondary phase is too weak. In other cases, the amplitude and width of the secondary phase increases with the amplitude of the velocity contrast, especially beyond a distance range where the S turning depth is deeper than the location depth of the segment (around 75° in Figure 3.6). Additionally, the arrival time of the secondary phase increases with the amplitude of velocity contrast beyond distance where the S turning depth is deeper than the location depth of the segment, and does not change before that.

The thickness of the segment affects the amplitude, width and arrival time of the secondary reflection phase as well, in a similar fashion as the amplitude of the velocity contrast. There are certain trade-offs between the amplitude of the velocity contrast and thickness. However, a comparison of the synthetic waveforms generated by two models, between a 20-km thick segment with -10 % velocity perturbation (Figure 3.6.d) and a 10-km thick segment with -20% velocity perturbation (Figure 3.6.b), indicates that increasing thickness would have a slightly larger impact on the amplitude, width and arrival time of the secondary phase.

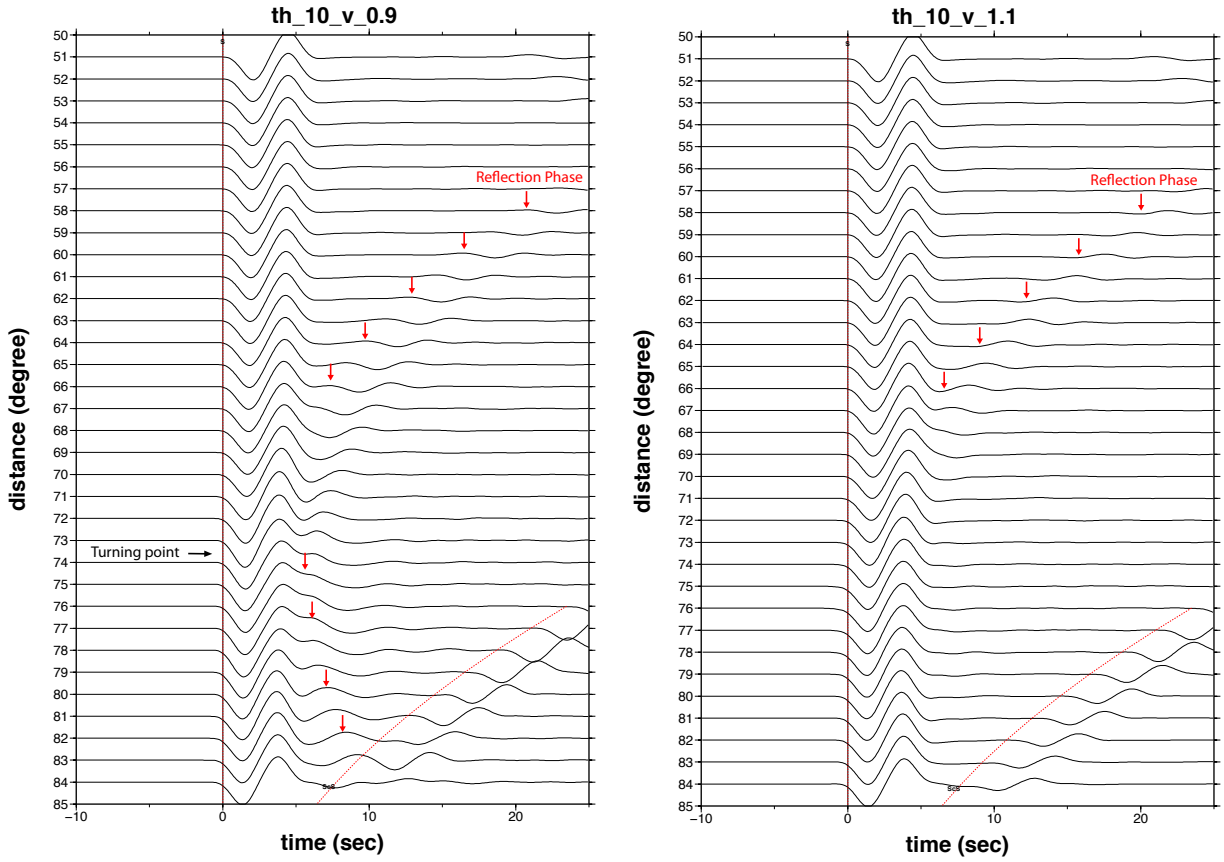

Figure 3.5. Comparison of the synthetic waveforms generated by a 10-km thick segment with -10% (left, low velocity anomaly) and 10% (right, high velocity anomaly) velocity perturbation.

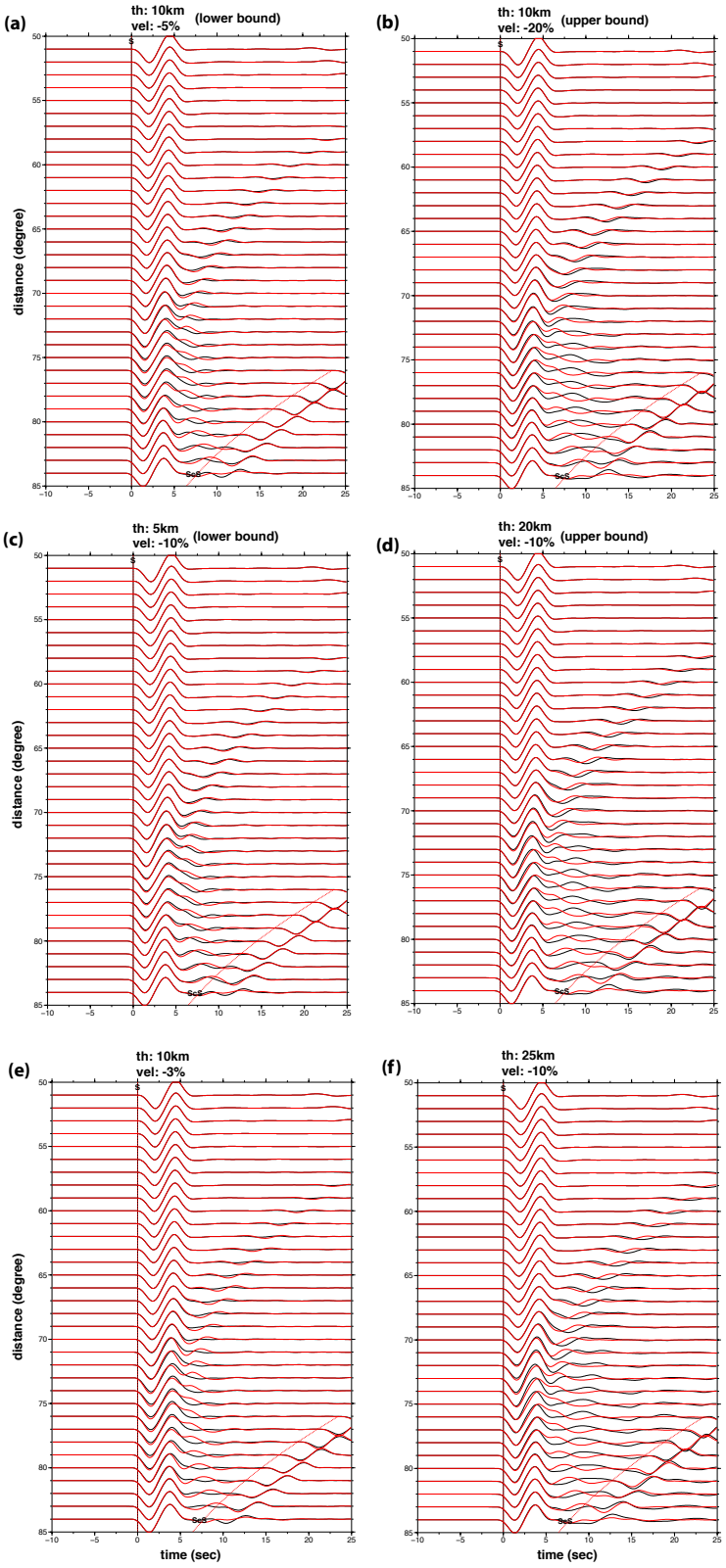

Figure 3.6. Comparisons of the synthetic waveforms generated by a segment with various thickness and velocity perturbation (black traces) and a 10-km thick segment with velocity perturbation of -10% (red traces). Other parameters are the same.

Depth, horizontal dimension and location, dipping angle of the segment control the move-out and the observable distance window of the secondary phase at the same time. First, placing the segments at larger depth would shift the move-out of the secondary phase to larger distance range (Figure 3.7.a and 3.7.d). Second, placing the segments at different location would shift the observable distance window of the secondary phase (Figure 3.7.a and 3.7.b). When the segment is moved from the source to the receiver, the observable distance window of the secondary phase shifts from closer distance to larger distance. The turning point between approaching and leaving S phase remains the same as long as the depth does not change. Move-out rate does not change with either horizontal location or depth. Similar shift also occurs when the segment is not flat. Third, dipping of the segment affects both the move-out and distance window where the secondary reflection phase can be observed. When the dipping angle is positive, it indicates that the segment dips towards the receiver side. In this case, the model with a larger dipping angle generates a secondary phase at larger distance ranges, and the move-out rate of the secondary phase approaching and leaving S phase both become larger. The secondary phase disappears when the dipping angle is beyond 15°. When the dipping angle is negative, it indicates that the segment dips towards the source side. In this case, the model with a larger dipping angle generates a secondary phase at closer distance ranges. The move-out rate of the secondary phase becomes smaller when approaching the S phase and becomes larger when leaving the S phase. The secondary phase disappears when the dipping angle is beyond -35°. A comparison between the waveforms generated by flat and dipped segment (Figure 3.7.a, 3.7.c and 3.7.d) shows the difference.

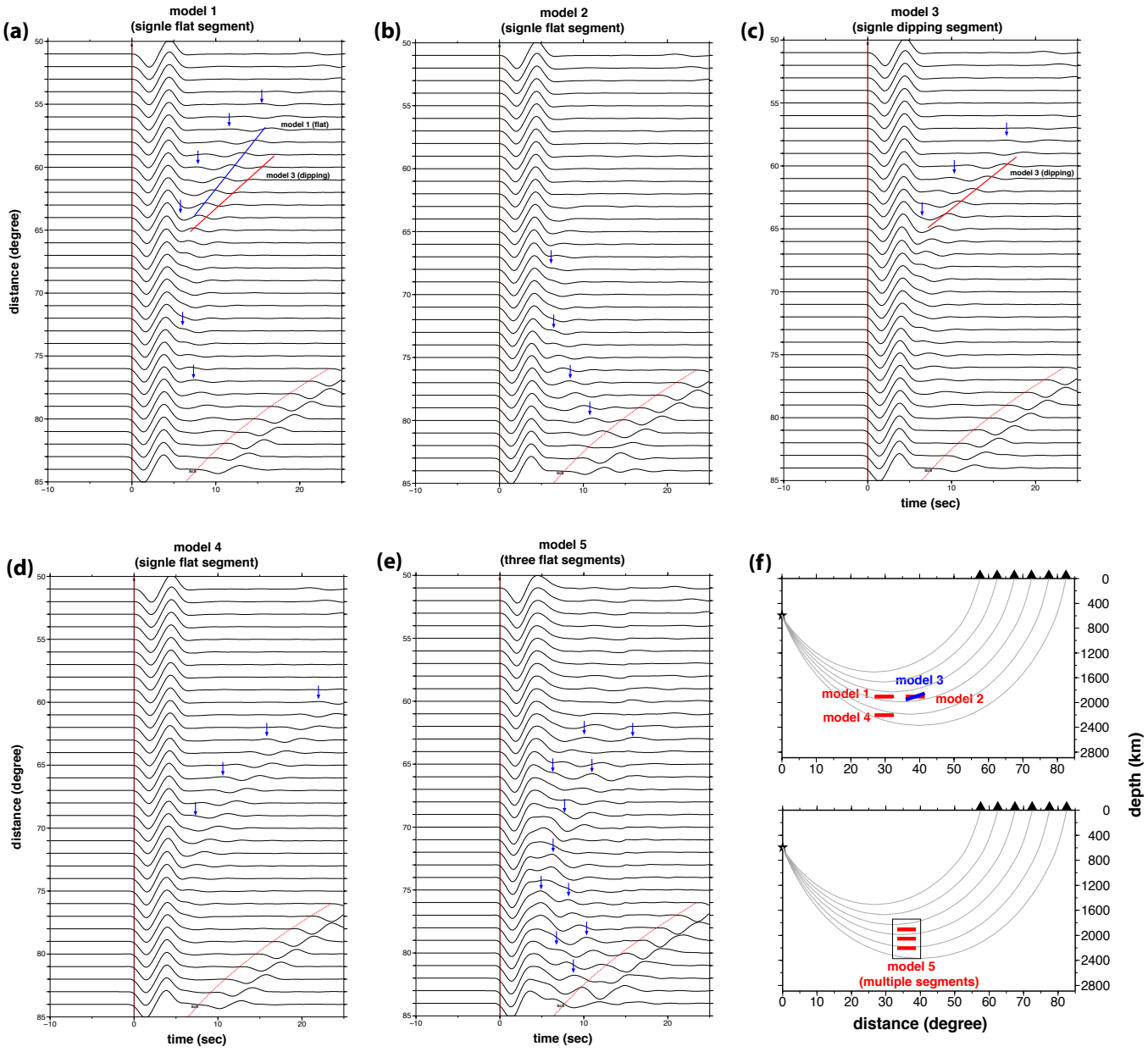

Figure 3.7. Synthetic waveforms generated by models with various depth, horizontal location, dipping angle, and number of segments. Blue arrows mark the arrivals of secondary phases.

Multiple segments generate multiple secondary phases. An example is shown in Figure 3.7.e. Depending on the depth separation of the segments, multiple secondary phases are superimposed with one another constructively or destructively. For models with dipping segments, similar superimpositions are observed.

3.4.3 Best fitting waveform modeling results

Forward waveform modeling is used to constrain the source of the additional reflection phases. Bench tests of forward waveform modeling show that the detailed waveform features, such as merging distance, move-out rate, and distance window of observable secondary phase, are closely tied with the location, dimension, orientation and velocity perturbation of the segments in the mid-lower mantle. The turquoise, green and blue sections are modeled individually. In each section, all synthetic waveforms generated by different event locations should be compatible with observed seismic waveforms.

Our best fitting model shows that several very low velocity segments with various dimensions are scattered in the center mid-lower mantle beneath Central America. In the turquoise section (waveform data shown as an example in Figure 3.4), two flat 1300-km wide, 10-km thick and one dipping 300-km wide, 20-km thick low velocity segments are located at 1800-km, 1950-km and 2150km (turquoise segments in Figure 3.8). In the green section, one flat 400-km wide, 10-km thick and one dipping 500-km wide, 10-km thick low velocity segments are located at 1730-km and 1850-km (green segments in Figure 3.9). In the blue section, one flat 700-km wide, 10-km thick, one dipping 400-km wide, 10-km thick and one flat 1000-km wide, 10-km thick low velocity segments are located at 1550-km, 1660-km and 1950-km (purple segments in Figure 3.10). To compare with data, all modeled waveforms are plotted as red traces in Figure 3.8, 3.9, and 3.10. The velocity perturbation of modeled low velocity segments is -10%, but there are slight trade-offs between velocity and thickness of the segment. Most of the segments are in horizontal position. The largest

dipping angle of non-flat segments is 13°. In the purple sections, no reflection feature is observed and thus no segment exists.

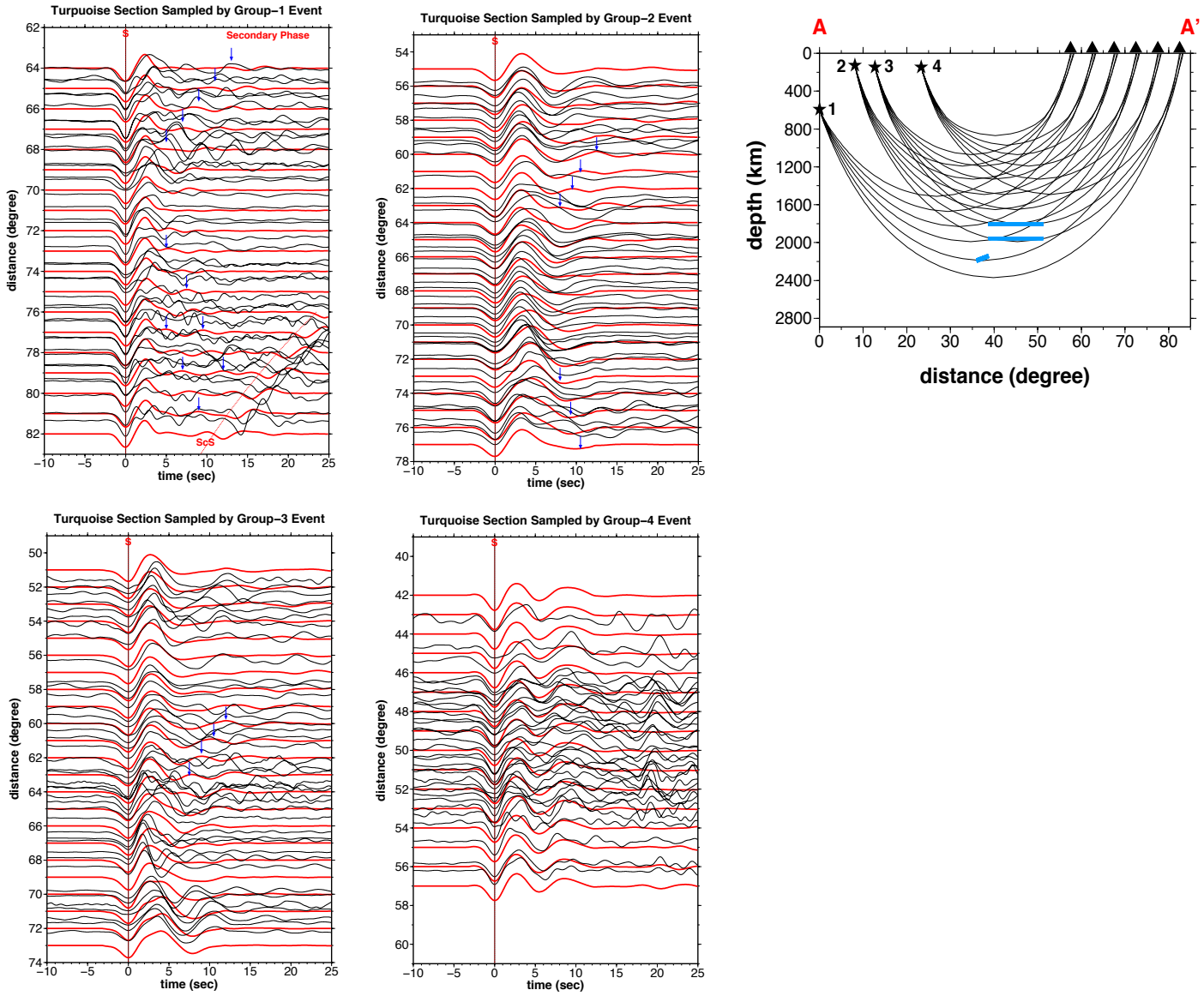

Figure 3.8. Synthetic waveforms generated by the best fitting velocity model in the turquoise section. All observations (black traces) and synthetics (red traces) are aligned by the S arrival. Blue arrows mark the arrival of the additional reflection phases distinct from the S and ScS phase. Turquoise segments marks the location of low velocity segments with -10% velocity perturbation in the mid-lower mantle of the turquoise section.

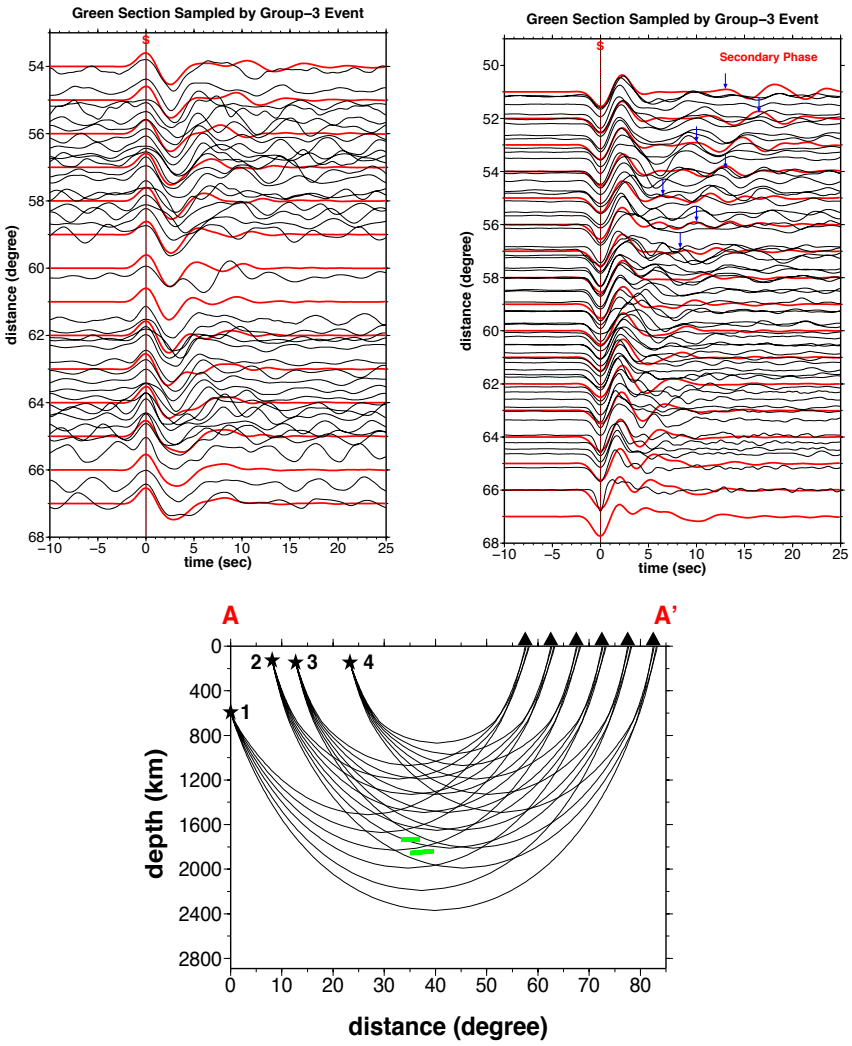

Figure 3.9. Synthetic waveforms generated by the best fitting velocity model in the green section. All observations (black traces) and synthetics (red traces) are aligned by the S arrival. Blue arrows mark the arrival of the additional reflection phases distinct from the S and ScS phase. Green segments marks the location of low velocity segments with -10% velocity perturbation in the mid-lower mantle of the green section.

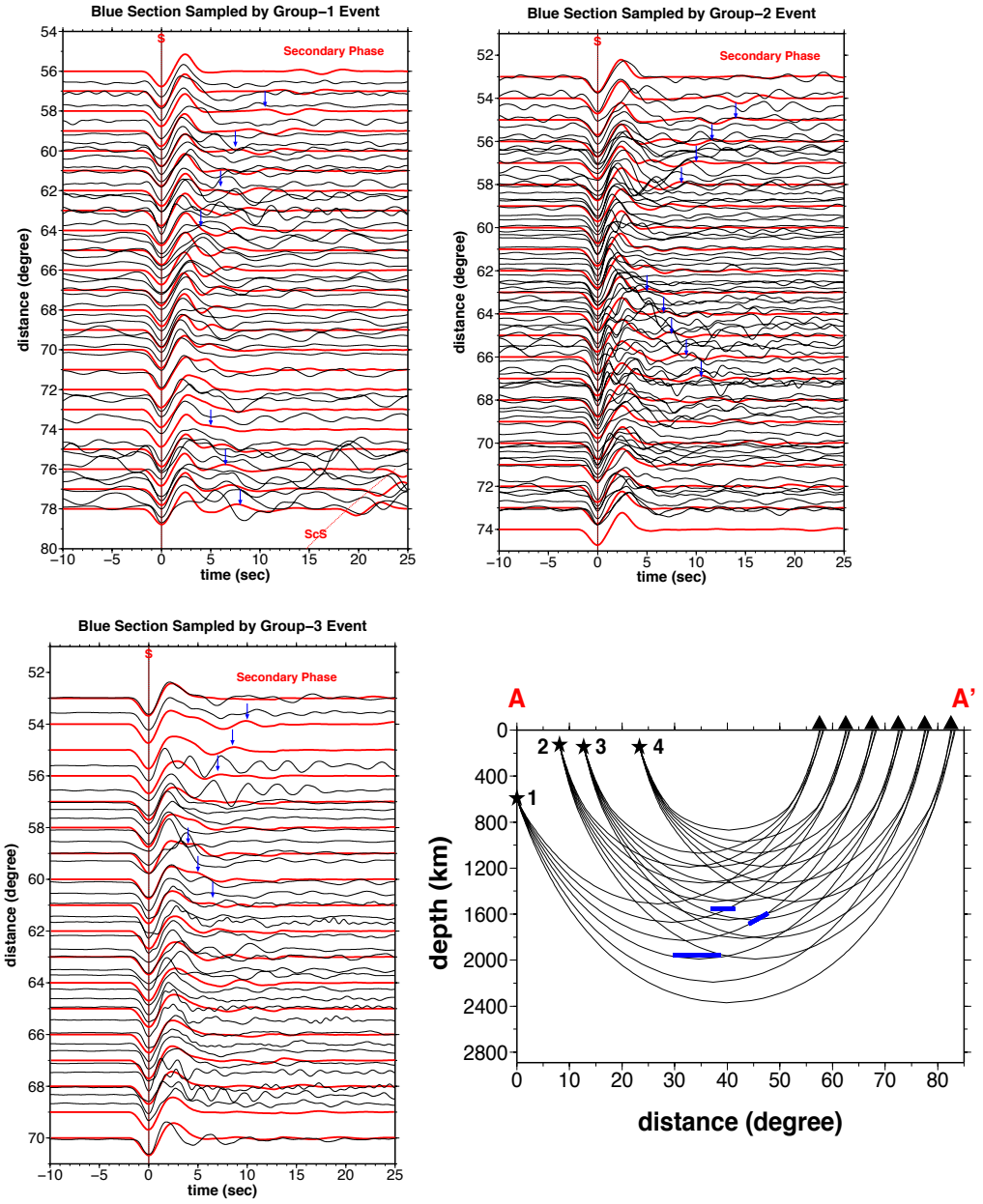

Figure 3.10. Synthetic waveforms generated by the best fitting velocity model in the blue section. All observations (black traces) and synthetics (red traces) are aligned by the S arrival. Blue arrows mark the arrival of the additional reflection phases distinct from the S and ScS phase. Blue segments marks the location of low velocity segments with -10% velocity perturbation in the mid-lower mantle of the blue section.

3.5 Travel time analyses and modeled "trapezoid-like" low velocity structure

3.5.1 Travel time analyses

Besides waveform observations, S and ScS travel time residuals sampling inside the red box of our study region in Figure 1a are also analyzed. Travel time data include two event sets. Each set of data is composed of events from different groups recorded at the same group of stations, which sample similar azimuthal section with different distance range. Our travel time analyses consist of two main steps: we first obtain absolute S and ScS residuals with reference to PREM model; then we correct for travel time residuals that are caused by heterogeneities other than from the mid-lower mantle. The corrected travel time residuals are solely tied to the mid-lower mantle structure.

One of our data set includes events 20120528, 20121008, 20120514 and 20120802 from south to north; the other data set includes events 20110902, 20110620, 20110608 and 20110824 from south to north. Southern events have further distance coverage and sample deeper, and northern events have closer distance coverage and sample shallower. These two data sets have very similar event locations. The recording station coverage is close as well. For each data set, we divide them into 4 sub-sets by every 2° of azimuth coverage.

Global shear wave tomography (Figure 3.11) shows that the upper mantle and crust effects are very strong, therefore it is important to remove travel time contributions from the upper mantle and crust during travel time analyses. Two

separate procedures are used to remove receiver and source side contributions. Receiver side contributions can be corrected by using one reference event because the ray-paths in the upper mantle and crust from different events are almost identical in the receiver side. We use the most northern event (20110824 for the 2011 event set and 20120802 for the 2012 event set) as reference event, and absolute travel time residuals of other events are corrected based on station location. Source side contributions can be corrected by using a group of western stations as reference because of similar ray-paths near the source for each event (Figure 3.11). The averaged absolute S travel time residuals from those western stations then correct the source side contributions for each event individually.

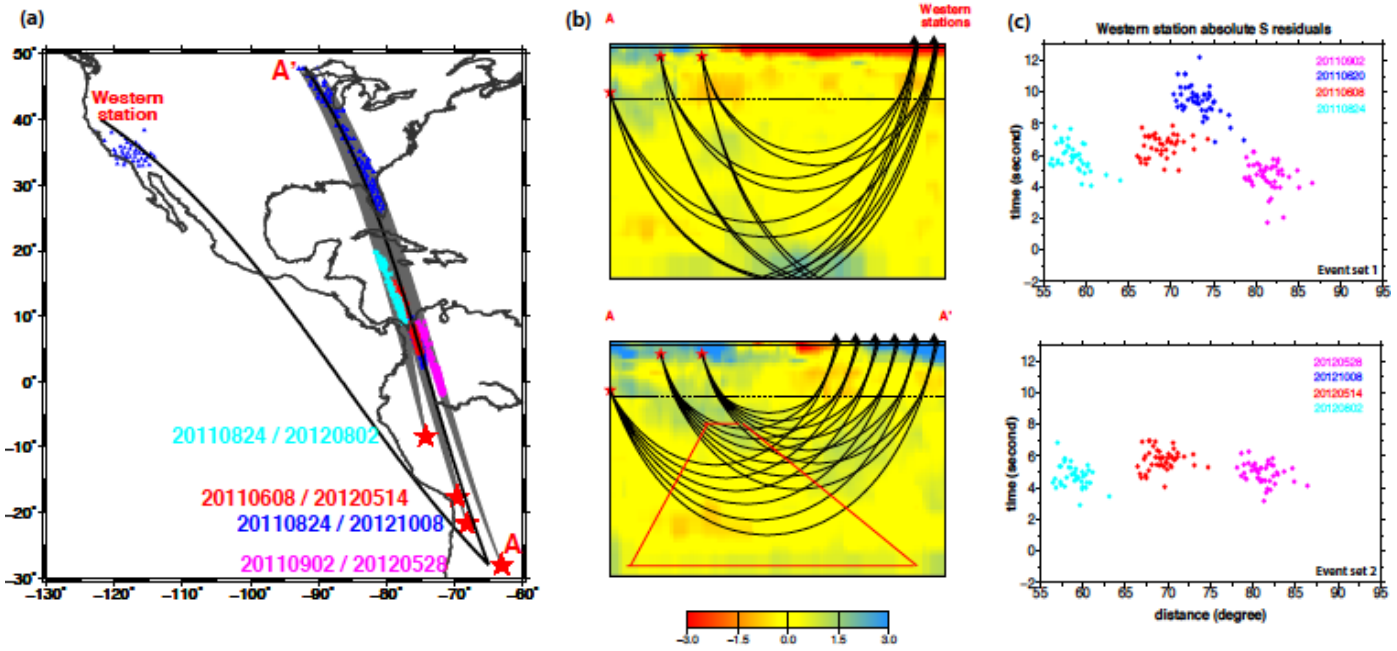

Figure 3.11. (a) Selected events (red stars), selected stations and reference western stations (blue triangles) location. AA' and A-western stations are two cross-sections. (b) Global shear wave tomography (*Grand, 2002*) along cross section AA' and A-western stations with corresponding S wave ray-paths from events to stations. (c) Absolute S residuals of western stations with reference to PREM model. For event 20121008, no clear S phase from western stations is available.

Detailed travel time analyses results are plotted in Figure 3.12 (2012 data set) and Figure 3.13 (2011 data set). The absolute S and ScS residuals from different events show strong correlation with station locations. This is expected due to the strong upper mantle and crust effect, and is later taken care of by corrections. After corrections, S travel time residuals keep increasing as distance increases from 45° to 80°, and have a change of increase rate around 55° (trend marked as black lines in Figure 3.12 and 3.13). There are still some notches in the corrected S travel time residuals, which are likely the remaining minor upper mantle and crust effects, but the main increasing trend for corrected S travel time residuals remains the same. The increasing trend of S residuals is consistent for all azimuths. For corrected ScS travel time residuals, notches also exist and no increasing trend as a function of distance is observed.

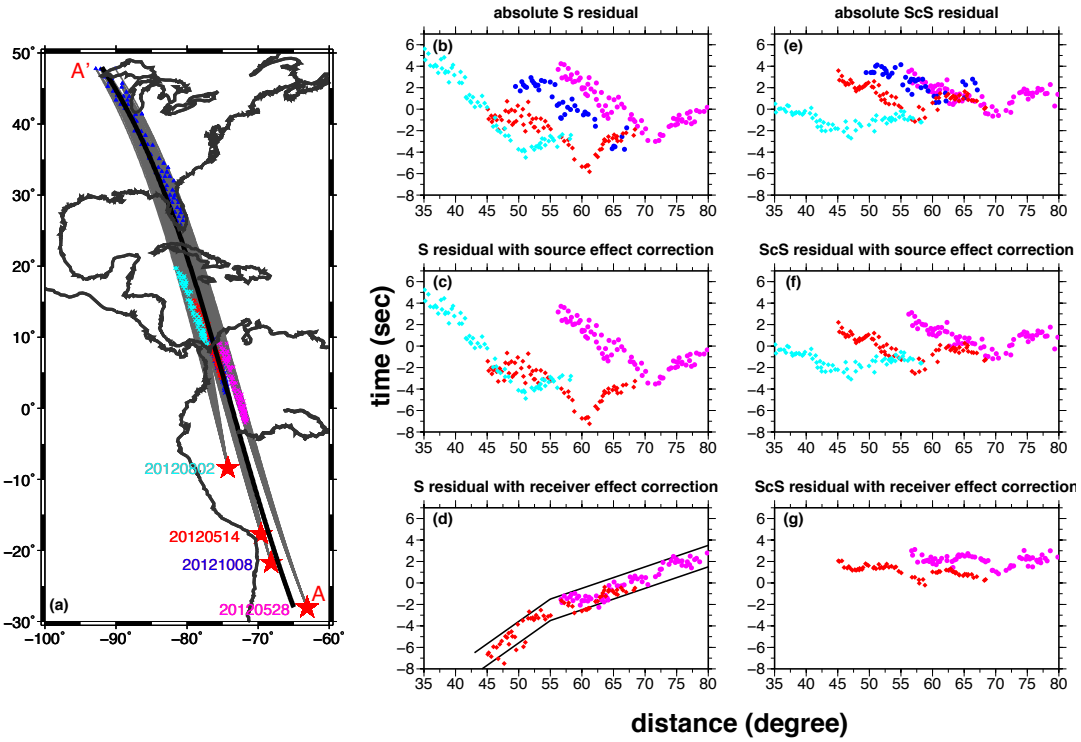

Figure 3.12. (1)

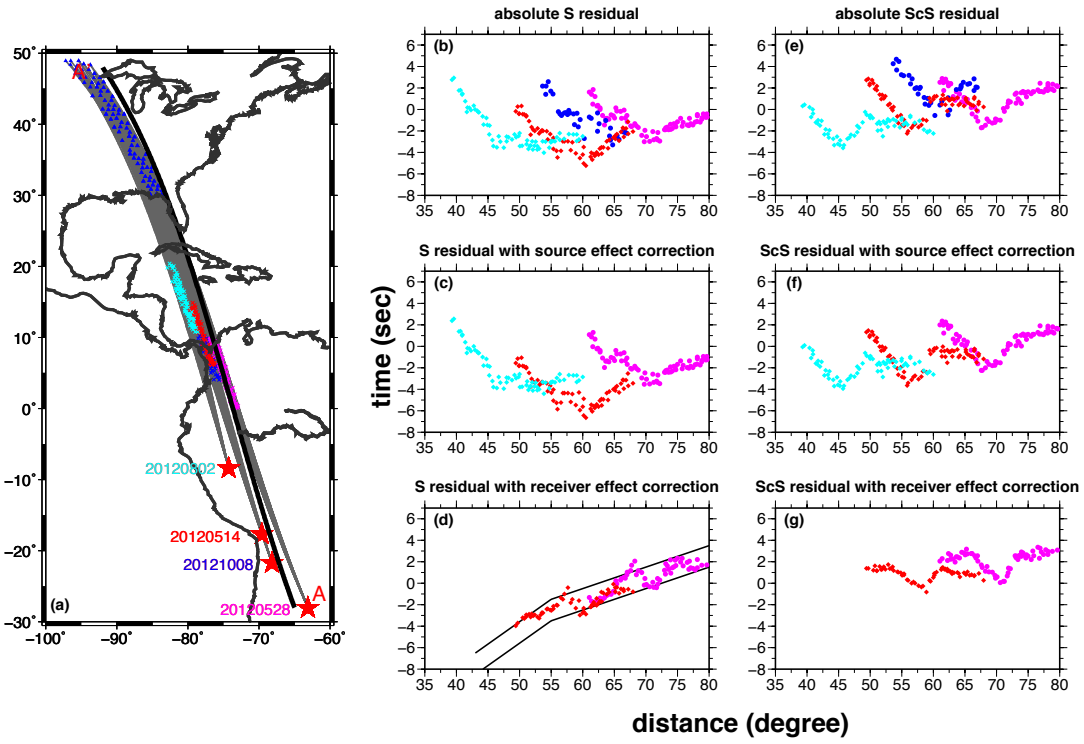

Figure 3.12. (2)

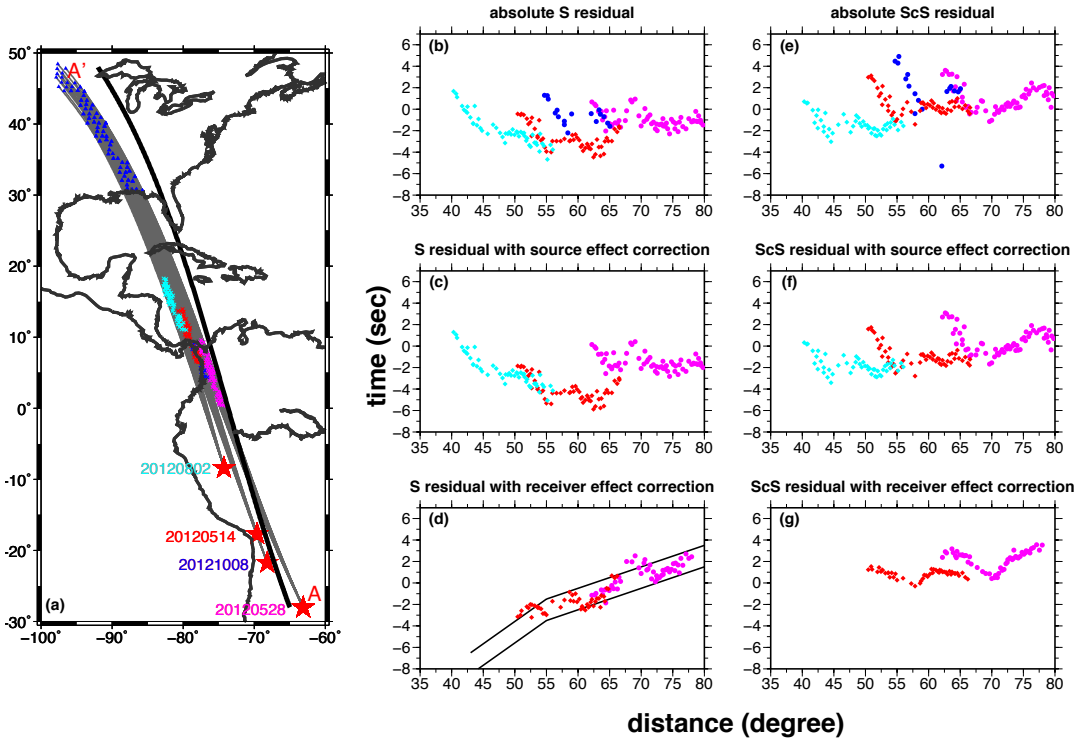

Figure 3.12. (3)

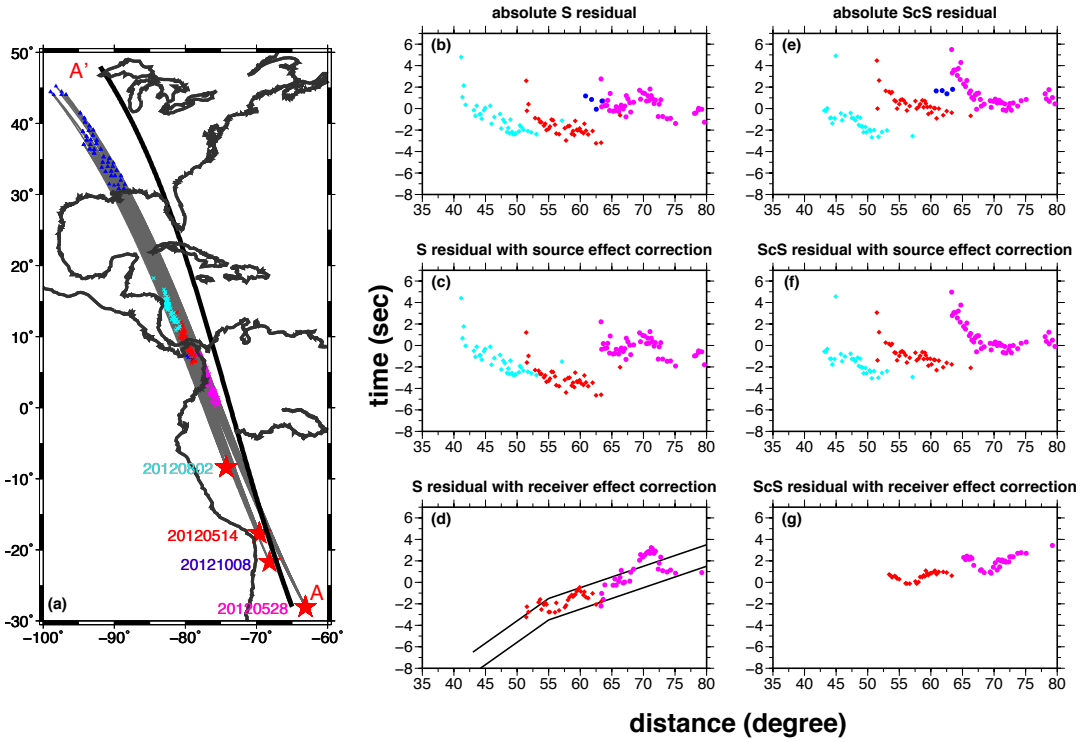

Figure 3.12. (4)

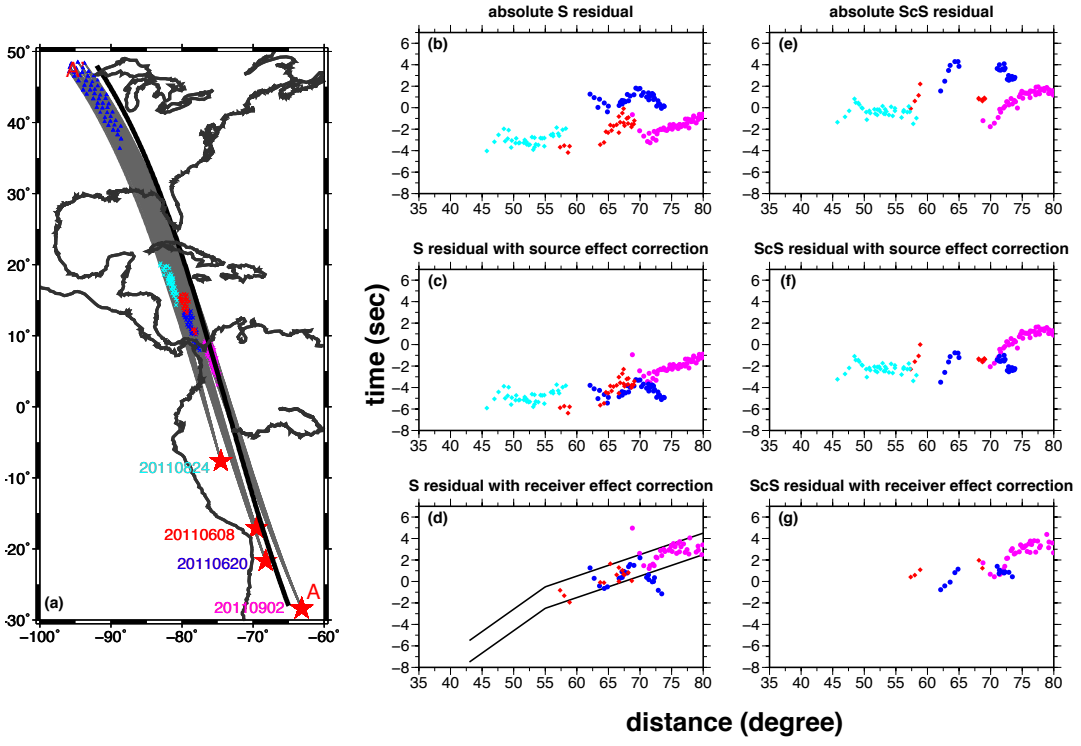

Figure 3.13. (1)

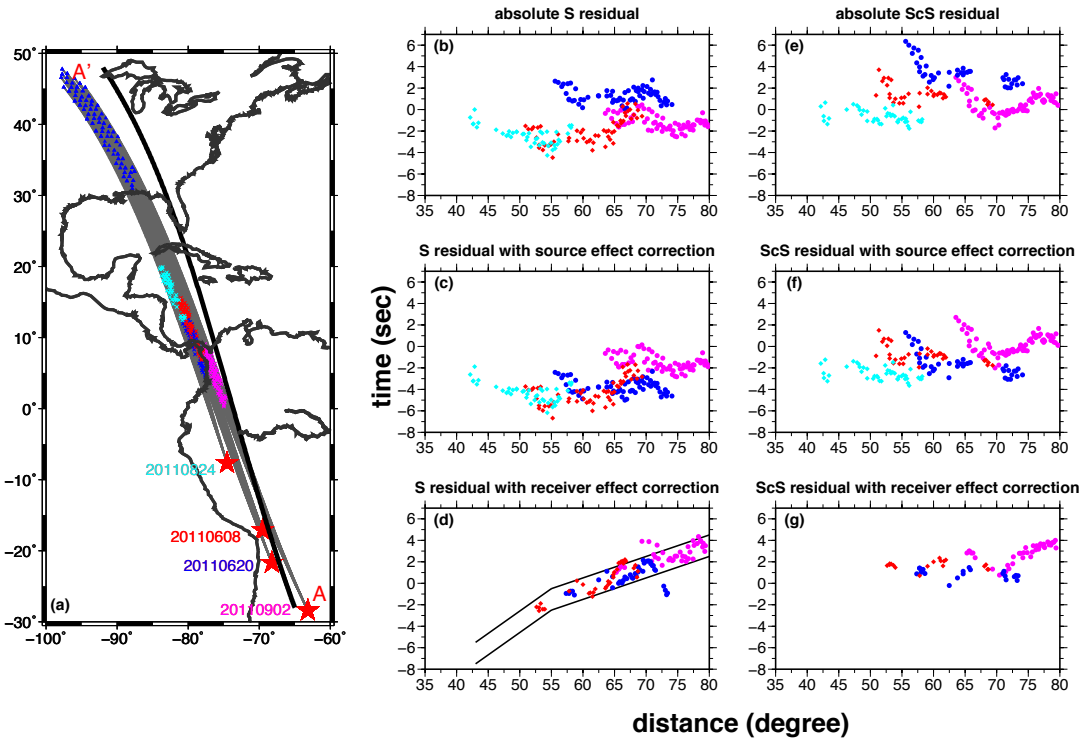

Figure 3.13. (2)

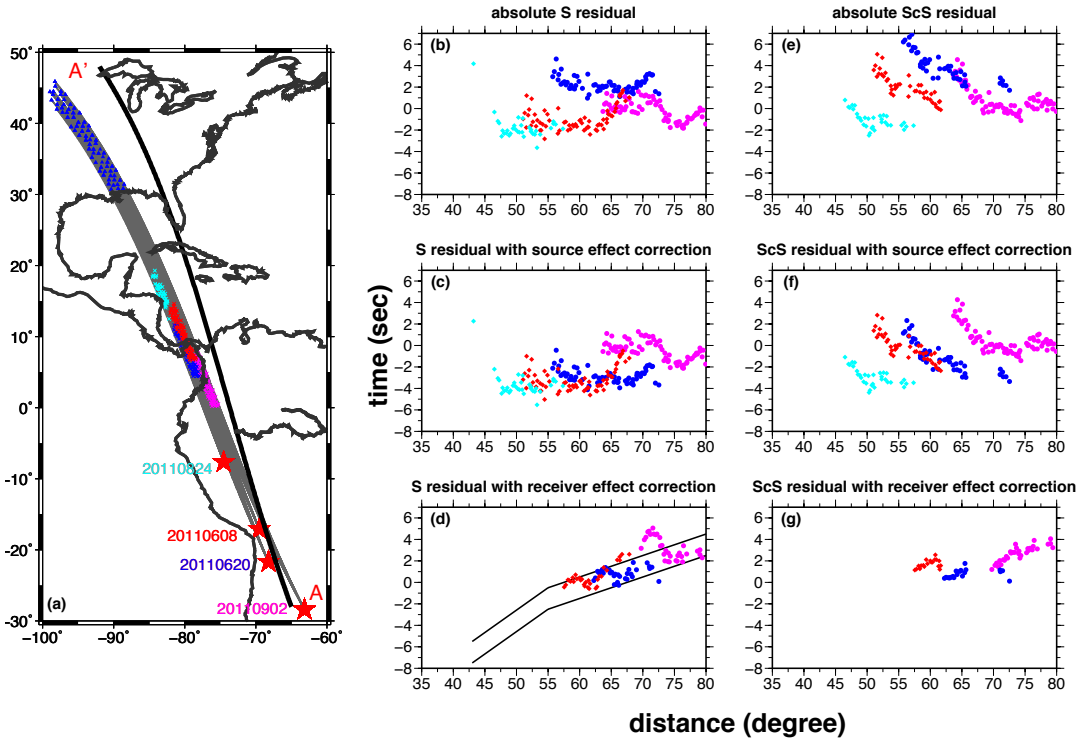

Figure 3.13. (3)

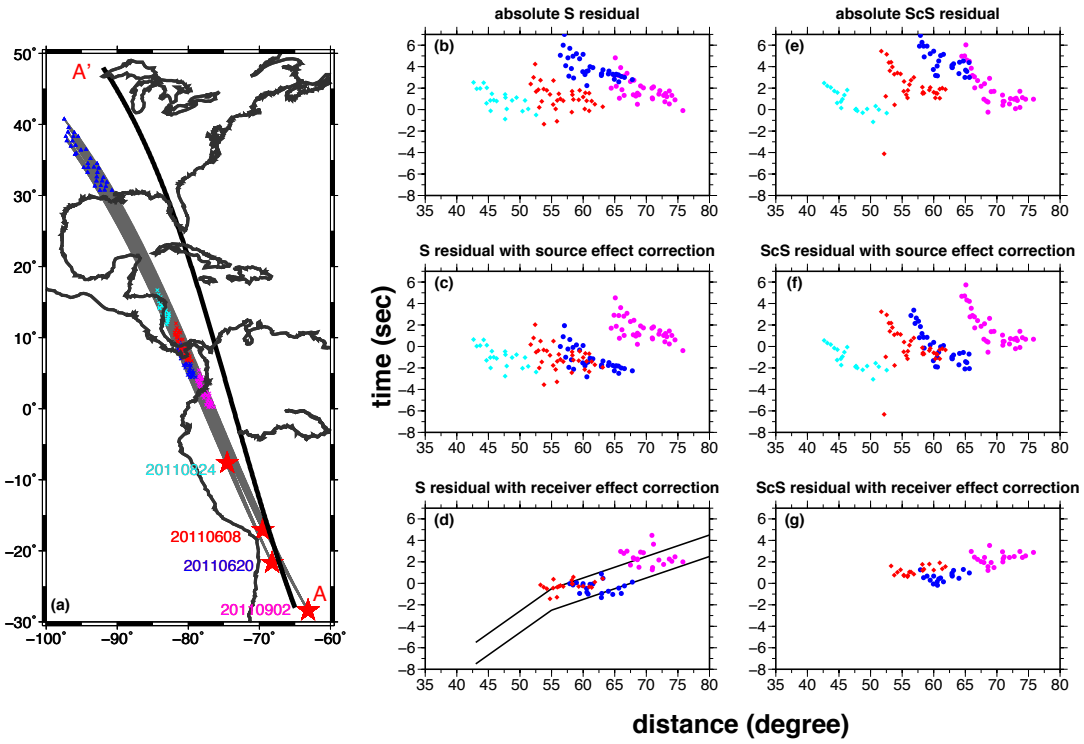

Figure 3.13. (4)

Figure 3.12. S and ScS travel time residuals from data set 1, which includes event 20120802, 20120514, 20121008, 20120528. 1(a) - 4(a) are sampling area of selected data; 1(b) - 4(b), 1(e) – 4(e) are absolute S and ScS travel time residual; 1(c) – 4(c), 1(e) – 4(e) are S and ScS travel time residual with source side correction; 1(d) – 4(d), 1(e) – 4(e) are S and ScS travel time residual with source side and receiver side corrections. Each color represents data from each event.

Figure 3.13. S and ScS travel time residuals from data set 2, which includes event 20110824, 20110608, 20110620 and 20110902. 1(a) - 4(a) are sampling area of selected data; 1(b) - 4(b), 1(e) – 4(e) are absolute S and ScS travel time residual; 1(c) – 4(c), 1(e) – 4(e) are S and ScS travel time residual with source side correction; 1(d) – 4(d), 1(e) – 4(e) are S and ScS travel time residual with source side and receiver side corrections. Each color represents data from each event. Note two data sets have overlapped coverage, and are consistent with each other.

3.5.2 Best fitting model for travel time observations

Considering minor scatterings of the data, the corrected S travel time residuals show an increase of up to 9 seconds as distance increases from 45° to 80°, and change of increase rate around 55° (Figure 3.12, 3.13 and 3.14.e). The travel time analyses indicate that S waves encounter a low velocity anomaly along their ray-paths. Forward travel time modeling is used to define the boundary and magnitude of the low velocity anomaly.

Our best travel time fitting model is a "trapezoid-like" low velocity region with -2% velocity perturbation extending up to 1000 km depth (red region in Figure 3.1.b or grey region in Figure 3.14.b). The model has a broad base and narrows as the depth decrease, therefore the S wave with further sampling distance travels deeper and has a larger portion of ray-path inside the low velocity anomaly. The top boundary are defined by the onset of the increasing S residuals; the change of increase rate of S residuals around 55° is the key characteristic used to place constraints on the width of the top of "trapezoid like" low velocity structure, the steepness of its edge, and its location. In the best fitting model, the S waves from the reference event (event 20120802 in Figure 3.14 or events from group 4) does not encounter this low velocity region until 60° which is out of the sampling distance range; whereas the S waves from other southern events travel through this region differently and show an increasing arrival delay as the corrected data shows (Figure 3.14.g). The ScS waves with various sampling distance, however, have similar portion of ray-path inside the "trapezoid-like" anomaly. The synthetic ScS residuals show no increasing trend as a function of distance (Figure 3.14.h) similarly to the corrected ScS residuals. A

constant offset exists between the corrected and modeled ScS residuals, and is likely caused by the lower-most mantle structure above the core-mantle boundary.

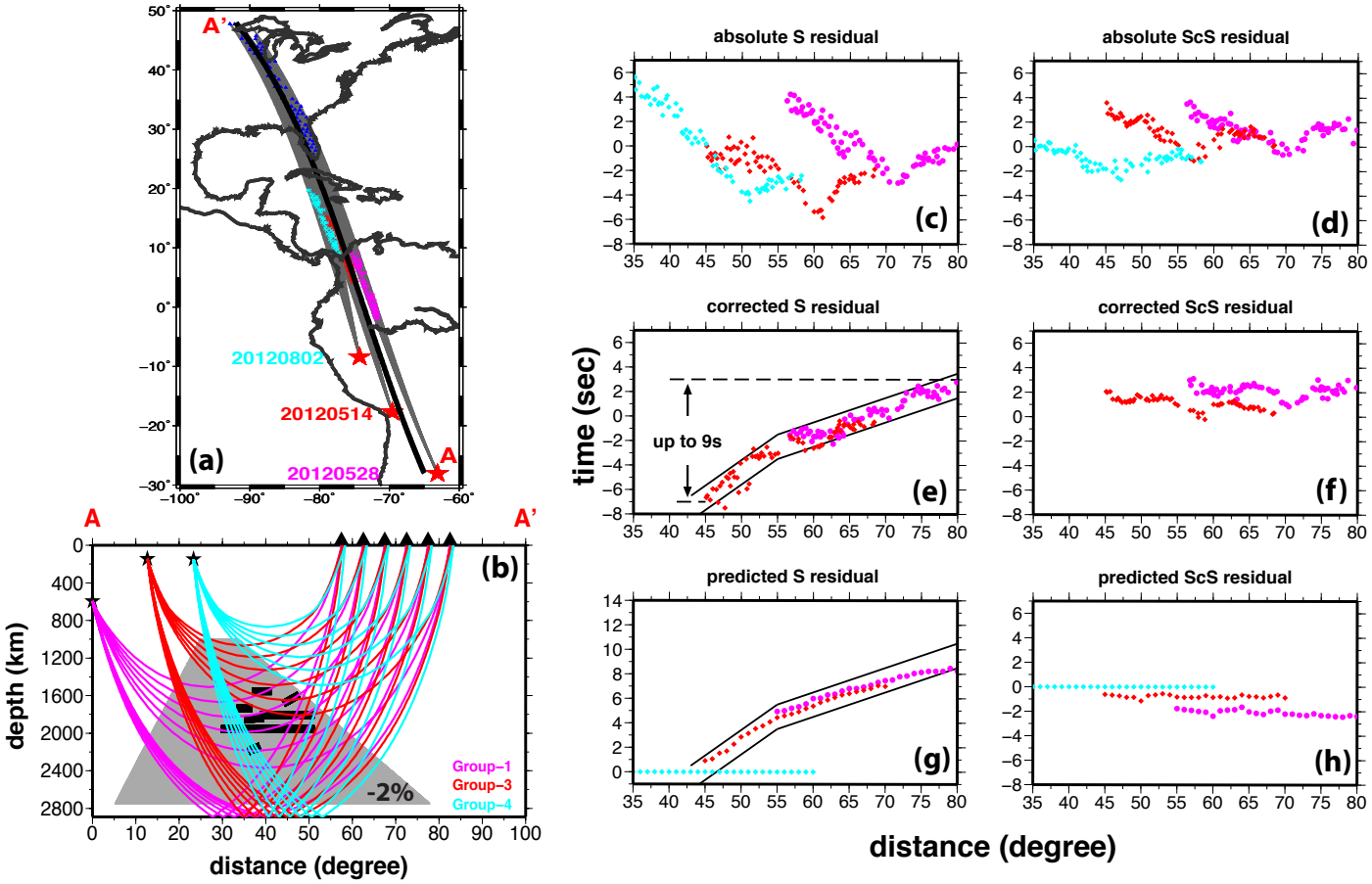

Figure 3.14. (a) Selected events (red stars) and stations (blue triangles) location. AA' are the sampling cross-section. (b) The best fitting model and S and ScS wave ray-path along sampled cross-section AA'. The grey "trapezoid-like" region has -2% shear wave velocity perturbation. (c) and (d) are absolute S and ScS travel time residuals with reference to PREM. (e) and (f) are corrected S and ScS travel time residuals. (g) and (h) are predicted S and ScS travel time residuals based on shear wave velocity structure of (b). Reference event is also used in (g) and (h). Different colors represent data and prediction of different event.

The bottom depth of the low velocity region is constrained by an "Scd-like" phase observed beyond 75°. Modeling results indicate the bottom boundary of the low velocity region is 2750 km (Figure 3.15) and a 1-2% velocity jump at the bottom is preferred (Figure 3.15). When the velocity jump is 1% (Model_2 in Figure3.16), no significant reflection phase is observed; when the velocity jump is 4% (Model_3 and Model_7 in Figure 3.16), the reflection phase is too strong and observable even around 56°. Synthetic waveforms generated by models with gradual velocity changes between 2750-km and CMB (Model_4, 5, 6 in Figure 3.16) do not fit the data either.

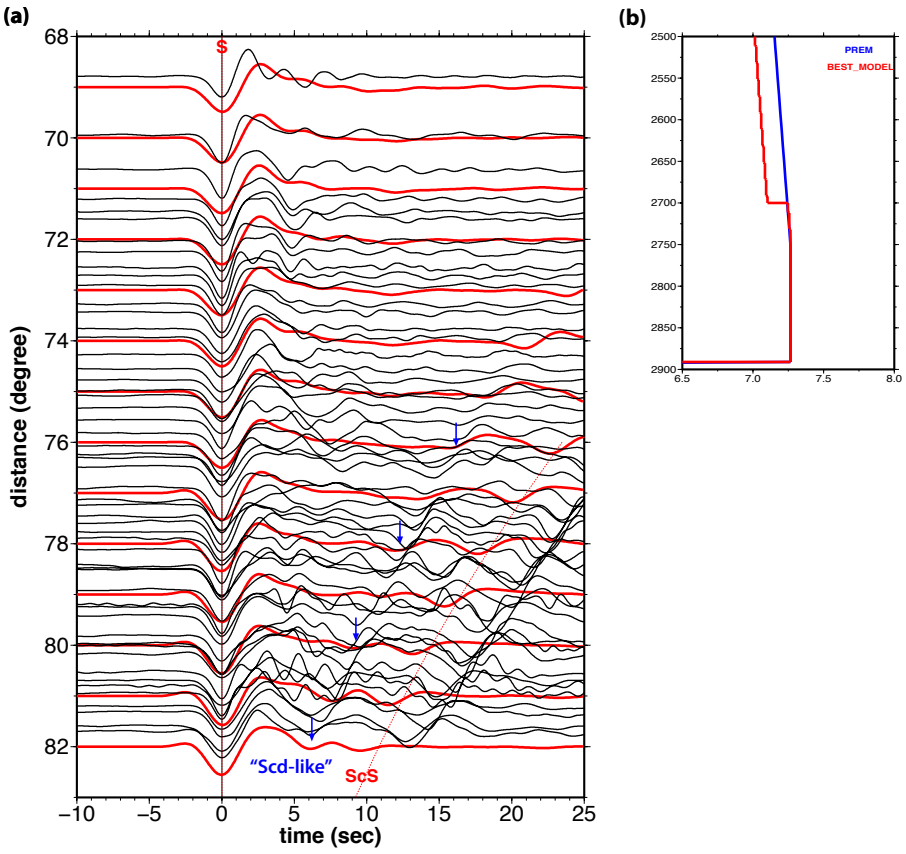

Figure 3.15. (a) Waveform observations (black traces) and the best fitting synthetics (red traces) of the "Scd-like" phase (marked by blue arrows), both aligned based on S arrival. (b) The best fitting bottom structure of the "trapezoid" low velocity structure based on the "Scd-like" phase.

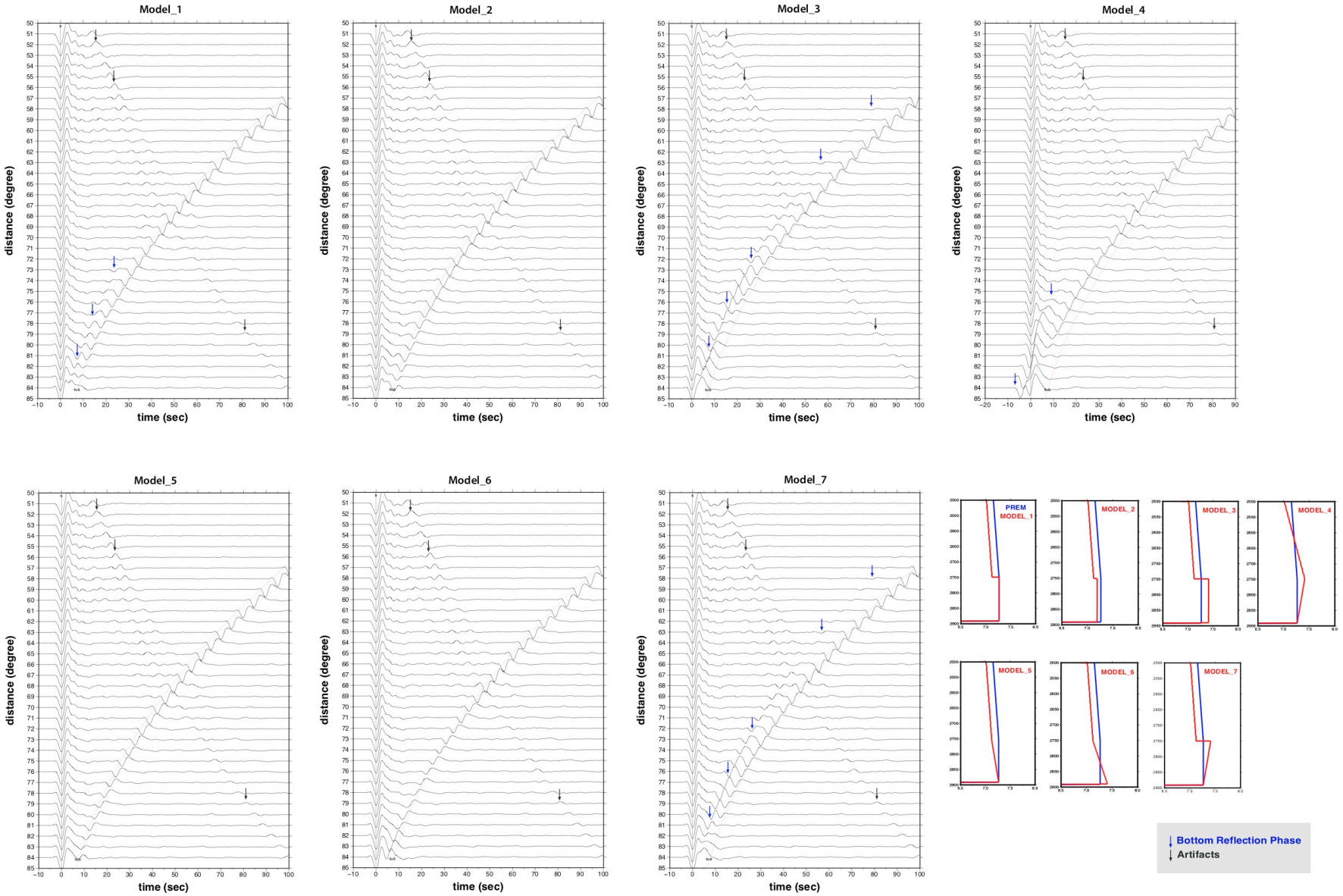
Model_1
Model_2
Model_3
Model_4
Model_5
Model_6
Model_7
distance (degree)
time (sec)
PREM
MODEL_1
MODEL_2
MODEL_3
MODEL_4
MODEL_5
MODEL_6
MODEL_7
↓ Bottom Reflection Phase
↓ Artifacts

Figure 3.16.

Figure 3.16. Comparison between synthetic waveforms generated by models with different bottom structures. All models have the same top "trapezoid" low velocity structure with –2% velocity perturbation. Model_1, Model_2 and Model_3 show an instant velocity jump from -2% to normal, -1% and 2% at 2750-km; Model_4 show gradual velocity increases from -2% to 2% between 2500-km and 2750km, and then gradual velocity decreases from 2% to normal between 2750-km and CMB; Model_5 and Model_6 show gradual velocity decreases from -2% to normal and 2% between 2750-km and CMB; Model_7 show an instant velocity jump from -2% to 2% at 2750-km, and then gradual velocity decreases from 2% to normal between 2750-km and CMB. All synthetic waveforms are aligned based on S phase. Blue arrows mark the corresponding reflection phase generated by the bottom structure; whereas black arrows mark the artifacts generated by the SH hybrid method.

In search of the best fitting shear wave velocity structure, "box-shaped" low velocity structure models are also tested. They generate "dome-shaped" S residuals because the lengths of the S wave ray-paths inside the low velocity region are similar (Figure 3.17). When the location changes, the shape of S residuals will change slightly. However, none of the "box-shaped" low velocity anomalies could generate continuously increasing S residuals between 45° and 80°.

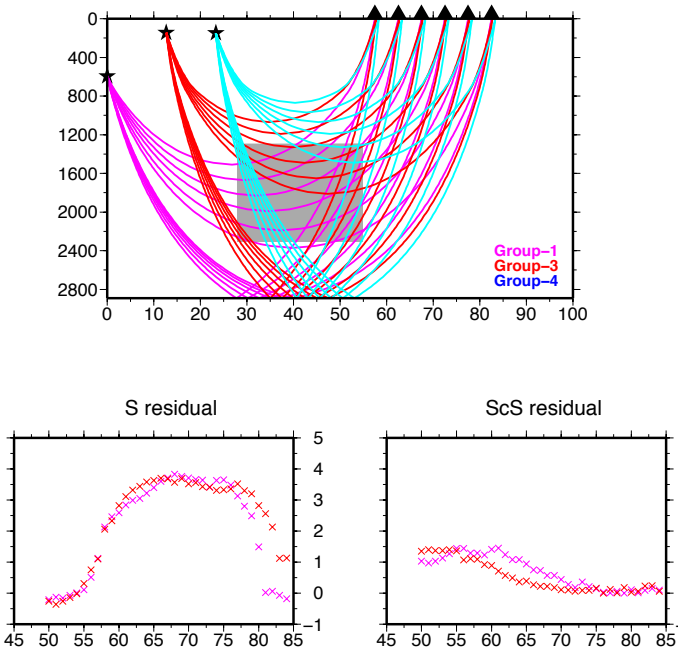

Figure 3.17. S and ScS travel time residuals generated by a "box-shaped" low velocity anomaly with -1% velocity perturbation.

Travel time analyses outside of the red box in Figure 1a are not available, thus we are not able to place constraints on the extent of this low velocity region on NNE-SSW direction.

3.6 Conclusions and discussions

In this study, we observed seismic waveform and travel time features related to a shear wave low velocity anomaly in the mid-lower mantle beneath Central America. Secondary reflection phases are observed after S arrival when sampling the center of our study region. The waveform features show significant variations with azimuth and distance. Travel time analyses reveal consistently increasing S phase residuals of up to 9 seconds between 45° and 80°. Forward waveform and travel time modeling reveals that several sub-horizontal 10-20 km thick segments with –10% shear wave velocity perturbation are buried inside a "trapezoid-like" low velocity region with –2% shear wave velocity perturbation extending between 1000 and 2750 km depth.

The low velocity structure beneath Central America shows strikingly strong similarities with the mid-lower mantle structure beneath African and the Pacific in terms of the geometry and velocity contrast. In both regions, low velocity anomalies with -2% to -3% shear wave perturbations extend high above the core mantle boundary with shape dipping edge, 1300km in Africa [*Wang and Wen, 2007*], and 740 km in the Pacific [*He and Wen, 2011*]. Our modeled structure in Central America has –2% velocity perturbations and extends between 1000 and 2750 km depth. Lateral dimensions at the base of all three low velocity structures are thousands of km. However, the lowermost mantle structures can be quite different. In African and the

Pacific regions, the very low velocity zone (VLVZ) is located at the lowermost mantle above core-mantle boundary, whereas in Central America region, it is not likely to be the same case. Hence it is interesting to discuss the source for these large-scale low velocity anomalies extending high up in the mid mantle. There are two possible explanations. One possible explanation would be intrinsic chemical differences in all three regions. These could be primary reservoirs existing since early Earth. The other possible explanation would be velocity anomalies caused by mantle convection. In the African and Pacific regions, thermal effect is the dominant force of mantle convection. In Central America, the complex subduction history is likely the main driving force of mantle convection (Figure 3.18). The active subduction on the west side and the ancient subduction on the east side push mantle material moving away from the center of Central America, and new material from the south and north direction flow back to fill it in, forming some heterogeneity in the mid-lower mantle beneath Central America. For the small-scale segments with -10% velocity segments buried inside the low velocity anomaly beneath Central America, partial melting likely occurs due to water or other weakening effects.

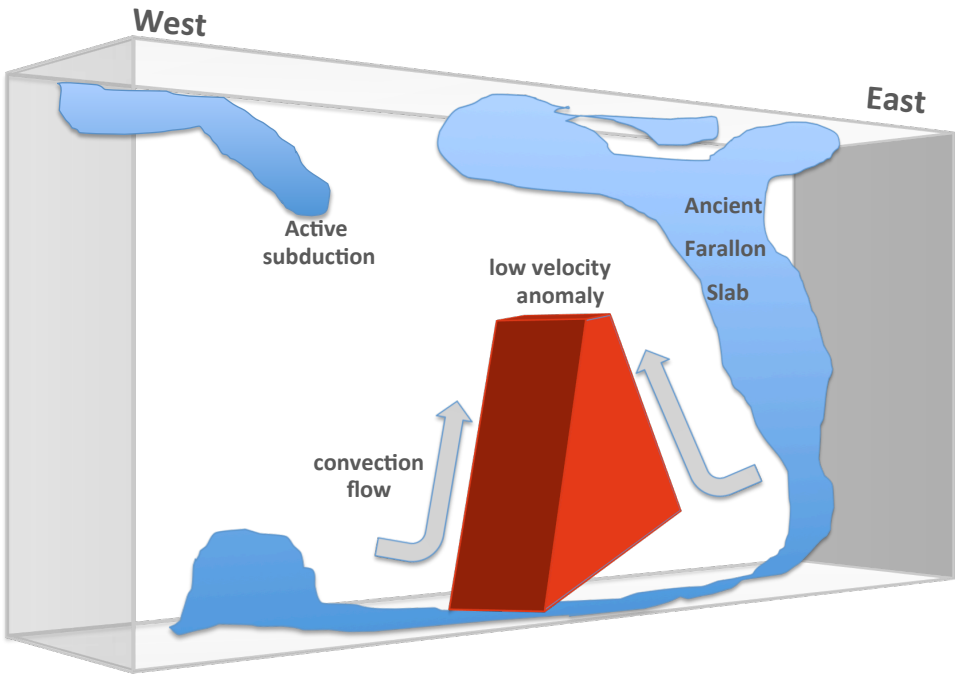

Figure 3.18. Illustration of mantle convection derived heterogeneity in the mid-lower mantle beneath Central America.

3.7 References

Bagley, B., Courtier, A. M., and Revenaugh, J., Seismic shear wave reflectivity structure of the mantle beneath northeast China and northwest Pacific, *J. Geophys. Res., 118*, 5417–5427, 2013.

Courtier, A. M. and Revenaugh, J., Slabs and shear wave reflectors in the midmantle, *J. Geophys. Res., 113*, B08312, doi:10.1029/2007JB005261, 2008.

Deuss, A., Global observations of mantle discontinuities using SS and PP precursors, Surv. Geophys., 30, 301-326, 2009.

He, Y. and Wen, L., Geographic boundary of the "Pacific Anomaly" and its geometry and transitional structure in the north, *J. Geophys. Res., 117*, B09308, doi:10.1029/2012JB009436, 2012.

Garnero, E. D. and Lay, T., D'' shear velocity heterogeneity, anisotropy and discontinuity structure beneath the Caribbean and Central America, *Phy. Earth Plant. Int., 140*, 219-242, 2003.

Grand, S. P., Mantle shear structure beneath the Americas and surrounding oceans, *J. Geophys. Res.*, *99*, 11,591–11,621, 1994.

Grand, S. P. and Helmberger, D. V., Upper mantle shear structure of North America, *Geophys. J. Roy. Astron. Soc., 76*, 399-438, 1984.

Grand, S. P., van der Hilst, R. D. and Widiyantoro, S., Global seismic tomography: A snapshot of convection in the Earth, *GSA Today*, *7*, 1-7, 1997.

Hutko, A. R., Lay, T., Garnero, E. J. and Revenaugh, J., Seismic detection of folded, subducted lithosphere at the core-mantle boundary, *Nature*, *441*, 333-336, 2006.

Kaneshima, S., Lower mantle seismic scatterers below the subducting Tonga slab: Evidence for slab entrainment of transition zone materials, *Phy. Earth Plant. Int., 222*, 35-46, 2013.

Kaneshima, S. and Helffrich, G., Dipping low-velocity layer in the mid-lower mantle: evidence for geochemical heterogeneity, *Science, 283*, 1888-1892, 1999.

Kaneshima, S. and Helffrich, G., Small scale heterogeneity in the mid-lower mantle beneath the circum-Pacific area, *Phy. Earth Plant. Int., 183*, 91-103, 2010.

Kawakatsu, H. and Niu, F., Seismic evidence for a 920-km discontinuity in the mantle, *Nature, 371*, 301-305, 1994.

Lay, T. and Helmberger, D. V., A lower mantle S-wave triplication and the shear velocity structure of D'', *Geophys. J. R. astr. Soc., 75*, 799-837, 1983.

Li, J. and Yuen, D. A., Mid-mantle heterogeneities associated with Izanagi plate: Implications for regional mantle viscosity, *Earth Plant. Sci. Lett, 385*, 137-144, 2014.

Lin, F., Moschetti, M. P. and Ritzwoller, M. H., Surface wave tomography of the western United States from ambient seismic noise: Rayleigh and Love wave phase velocity maps, *Geophys. J. Int.,* doi: 10.1111/j.1365-246X.2008.03720.x, 2008.

Lithgow-Bertelloni, C. and Richards, M. A., The dynamics of Cenozoic and Mesozoic plate motions, *Rev. Geophys*., *36*, 27-78, 1998.

Liu, L. and Stegman, D. R., Segmentration of the Farallon slab, *Earth Planet. Sci. Lett.*, *311*, doi: 10.1016/j.epsl.2011.09.027, 2011.

Miller, M. S. and Niu, F., Bulldozing the core-mantle boundary: Localized seismic scatterers beneath the Caribbean Sea, *Phys. Earth and Planet. Int., 170*, 89-94, 2008.

Ni, D., Tan. E., Curnis, M. and Helmberger, D. V., Shape sides to the African superplume, *Science, 296,* 1850-1852, 2002.

Niu, F. and Kawakatsu, H., Depth variation of the mid-mantle seismic discontinuity, *Geophys. Res. Lett., 24,* 429-432, 1997.

Niu, F., Kawakatsu, H. and Fukao, Y., Seismic evidence for a chemical heterogeneity in the midmantle: a strong and slightly dipping seismic reflector beneath the Mariana subduction zone, *J. Geophys. Res., 108*, doi:10.1029/2002JB002384, 2003.

Obrebski, M., Allen. R. M., Pollitz, F. and Hung, S., Lithosphere–asthenosphere interaction beneath the western United States from the joint inversion of body-

wave traveltimes and surface-wave phase velocities, *Geophys. J. Int., 185*, 1003–1021, 2011.

Ren, Y., Stutzmann, E., van der Hilst, R. D. and Besse, J., Understanding seismic heterogeneities in the lower mantle beneath the Americas from seismic tomography and plate tectonic history, *J. Geophys. Res*., *112*, doi: 10.1029/2005JB004154, 2007.

Ritsema, J., H. J. van Heijst, and J. H. Woodhouse, Complex shear wave velocity structure imaged beneath Africa and Iceland, *Science, 286,* 1925– 1928, 1999.

Sebastian, R., Garnero, E. J. and Williams, Q., Seismic array detection of subducted oceanic crust in the lower mantle, *J. Geophys. Res., 113*, B06303, doi:10.1029/2007JB005263, 2008.

Shen, Y., Wolfe, C. J., and Solomon, S. C., Seismological evidence for a mid-mantle discountinuity beneath Hawaii and Iceland, *Earth Planet. Sci. Lett., 214,* 143-151, 2003.

Sigloch, K., Mantle provinces under North America from multi-frequency P-wave tomography, *Geochem. Geophys. Geosyst., 12,* DOI: 10.1029/2010GC003421, 2011.

Sigloch, K., McQuarrie, N. and Nolet, G., Two-stage subduction history under North America inferred from multiple-frequency tomograpgy, *Nature Geoscience*, *1*, 458-462, 2008.

Stunff, Y. L., Wicks Jr., C. W., Romanowicz, B., P'P' precursors under Africa: Evidence for mid-lower reflectors, *Sciecne, 270*, 74-77, 1995.

Su, W. J., R. L. Woodwoard, and A. M. Dziewonski (1992), Degree 12 model of shear velocity heterogeneity in the mantle, *J. Geophys. Res., 99*, 6945– 6980.

Sun, D., Song, T. A. and Helmberger, D. V., Complexity of D'' in the presence of slab-debris and phase changes, *Geophys. Res. Lett.*, *33*, doi: 10.1029/2005GL025384, 2006.

Sun. D. and Helmberger, D. V., Upper-mantle structures beneath USArray derived from waveform complexity*, Geophys. J. Int., 184*, 416-438, 2011.

Tanaka, S., Suetsugu, D., Shiobara, H., Kanazawa, T., Fukao, Y., Barruol, G. and Reymod, D., On the vertical extent of the large low shear velocity province beneath the South Pacific Superswell, *Geophys. Res. Lett., 36,* L07305, doi:10.1029/2009GL037568, 2009.

Tanaka, S., Suetsugu, D., Shiobara, H., Kanazawa, T., Fukao, Y., Barruol, G. and Reymod, D., On the vertical extent of the large low shear velocity province beneath the South Pacific Superswell, *Geophys. Res. Lett., 36*, L07305, doi:10.1029/2009GL037568, 2009.

Thomas, C., Garnero, E. J. and Lay, T., High-resolution imaging of lowermost mantle structure, *J. Geophys. Res., 109*, doi: 10.1029/2004JB003013, 2004.

To, A., Romanowicz, B., Capdeville, Y. and Takeuchi, N., 3D effects of sharp boundaries at the borders of the African and Pacific Superplumes: Observation and modeling, *Earth Planet. Sci. Lett., 233*, 137-153, 2005.

van der Lee, S. and Nolet, G., Upper mantle S velocity structure of North America, *J. Geophys. Res., 102*, 22,815-22,838, 1997.

van der Lee, S., Regenauer-Lieb, K. and Yuen, D. A., The role of water in connecting past and future episodes of subduction, *Earth Planet. Sci. Lett., 273*, 15-27, doi:10.1016/j.epsl.2008.04.041, 2008.

van der Lee, S. and Frederiksen, A., Surface wave tomography applied to the North America, *in Seismic Earth: Array Analysis of Broadband Seismograms* (eds A. Levander and G. Nolet), American Geophysical Union, Washington, D.C.. doi: 10.1029/157GM05, 2013.

van der Hilst, R. D., Widiyantoro, S. and Engdahl, E. R., Evidence for deep mantle circulation from global tomography, *Nature*, *386*, 578-584, 1997.

Vanacore, E., Niu, F., and Kawakatsu, H., Obervations of the mid-mantle discontinuity beneath Indonesia from S to P converted waveforms, *Geophys. Res. Lett., 33*, L04302, doi:10.1029/2005GL025106, 2006.

Vinnik, L., Kato, M., and Kawakatsu, H., Search for seismic discontinuities in the lower mantle, *Geophys. J. Int., 147*, 41-56, 2001.

Vinnik, L. P., Oreshin, S. I., Speziale, S. and Weber, M., Mid-mantle layering from SKS receiver functions, *J. Geophys. Res., 37*, L24302, doi:10.1029/2010GL045323, 2010.

Wang, Y. and L. Wen, Geometry and P and S velocity structure of the "African Anomaly", *J. Geophys. Res*., *112*, B05313, doi:10.1029/2006JB004483, 2007.

Wen, L., An SH hybrid method and shear velocity structure in the lowermost mantle beneath the central Pacific and South Atlantic Oceans, *J. Geophys. Res., 107*, doi: 10.1029/2001JB000499, 2002.

Wessel, P., and W. H. F. Smith, New version of the Generic Mapping Tools released, *Eos Trans. AGU, 76(33)*, 329, 1995.

Wysession, M. E., Fischer, K. M., Al-eqabi, G. I., Shore, P. J. and Gurari, I., Using MOMA broadband array ScS-S data to image smaller scale strucutures at the base of the mantle, *Geophys. Res. Lett., 28*, 867-870, 2001.

Yoshito, F., Widiyantoro, S. and Obayashi, M., Stagnant slabs in the upper and lower mantle transition region, *Reviews of Geophysics*, *39*, 291-323, 2001.

Chapter 4

A Transition of Velocity Structure at the Lowermost Mantle Beneath Central America

4.1 Abstract

We suggest the existence of a structural transition at the base of the Earth's mantle beneath Central America based on ScSH-SH and PcP-P differential travel time residuals. Our seismic data set includes Southern American earthquakes recorded at USArray stations between 2007 and 2011. The analyzed ScSH-SH differential travel time residuals show that the shear wave velocity decreases from at lease 2% velocity perturbation to normal along the northwest-southeast direction; and the analyzed PcP-P differential travel time residuals show that the compressional wave velocity decreases from normal to -2% velocity perturbation along the same direction. Both shear and compressional velocity experience a 2% of velocity decrease along the northwest-southeast direction, suggesting that a structural transition boundary likely exists at the lowermost mantle beneath Central America. Stacked S or ScS waveforms sampling different velocity perturbation provinces are slightly different, but stacked S and ScS waveforms sampling the same velocity perturbation province are very similar. Stacked P or PcP waveforms sampling different velocity perturbations are also very similar. These indicate that attenuation is relatively uniform across different provinces. Moreover, the rapidly changing ScSH/SH amplitude ratio and incoherently delayed radial component S and ScS phases both indicate widely existing anisotropy and

heterogeneity. Relatively simple shear waveform features indicate that the heterogeneity is of relatively small-scale.

4.2 Introduction

The lowermost mantle is one crucial part of the Earth because it is the region where heat is conducted from the core into the mantle and has major implications for thermal evolution and mantle dynamics. As we mentioned in Chapter 3, many studies have focused on the lower-most mantle structure beneath Central America, detecting high-velocity anomalous D'' shear wave structures [*Garnero and Lay, 2003; Lay and Helmberger, 1983*] with possibly folded features [*Hutko et. al., 2006; Sun et. al., 2006*], small-scale low-velocity anomalies inside the large high-velocity anomalies [*Wysession et. al., 2001; Thomas et. al., 2004*], scatterers near the high-velocity anomalies [*Miller and Niu, 2008*] and rapid P-wave travel time change across a small region [*Sun et. al., 2006*]. Past studies have shown that the lowermost mantle beneath Central America is very complex. Given the improvement of data coverage, we are interested in finding seismic features that might have been missed in the past. In this study, we suggest a structural transition by using both shear and compressional shear wave travel time and waveform observations.

4.3 Seismic data

We collect broadband displacement of 14 South American earthquakes between 2007 and 2011 (listed in Table 4.1) recorded at USArray stations. Our seismic data provide a dense coverage near the core mantle boundary in Central America. The

seismograms are deconvolved using their corresponding instrument response and rotated to tangential, radial and vertical components. Tangential and radial seismograms are band-pass filtered between 0.1-1 Hz, and vertical seismograms are band-pass filtered between 1-4 Hz. Arrival times of S, ScS, P and PcP phases are hand picked.

Table 4.1. Event List

Event Date	Origin Time	Latitude($^{\circ}N$)	Longitude($^{\circ}E$)	Depth(km)
2007/05/25	17:47:31.0	-24.22	-67.03	180
2007/07/21	15:34:53.0	-22.15	-65.78	289
2007/11/16	03:12:59.8	-23.10	-77.84	122
2008/02/04	17:01:17.0	-20.27	-70.76	46.1
2008/09/03	11:25:14.0	-26.74	-63.22	569
2008/10/12	20:55:42.0	-20.12	-64.97	352
2009/07/12	06:12:50.0	-15.25	-70.75	197
2009/09/05	03:58:39.0	-15.12	-70.25	210
2009/11/14	19:44:33.0	-23.04	-66.83	221
2010/01/28	08:04:16.0	-23.64	-66.96	205
2010/03/04	22:39:29.0	-22.36	-68.69	119
2010/05/24	16:18:33.0	-8.08	-71.64	591
2010/07/12	00:11:26.0	-22.24	-68.61	134
2011/01/01	09:57:04.0	-27.04	-63.39	586

Because ScS and S phases propagate along similar ray paths in the upper mantle and crust (Figure 4.1), ScS-S differential travel time residuals minimize upper mantle and crustal heterogeneity effects. This is also true for PcP-P differential travel time residuals. In this study, we mainly use ScSH-SH and PcP-P differential travel time residuals to constrain velocity perturbations in the lowermost mantle. We further use comparisons of stacked waveforms, the ScSH/SH amplitude ratio, differentiated arrival times of radial and tangential S and ScS phases, and waveform complexity to investigate possible seismic features in the lowermost mantle in this region.

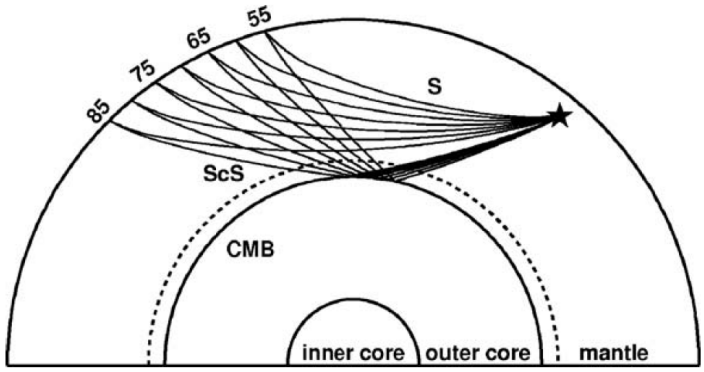

Figure 4.1. Illustration of S and ScS ray-paths in the mantle.

4.4 A structural transition in the lowermost mantle based on ScSH-SH and PcP-P differential travel times

The ScSH-SH and PcP-P differential travel-time residuals provide good coverage in the lowermost mantle beneath Central America (Figure 4.2 and 4.3). We are primarily interested in the velocity structure in the lowermost 300 km of the mantle. Three steps are taken to obtain the velocity perturbations in the lowermost mantle. First, absolute differential travel time residuals with reference to PREM model are obtained. Next, tomographic corrections are used to remove the effects of heterogeneities 300km above the core mantle boundary. Despite the fact that ScSH-SH and PcP-P differential travel time residuals are not sensitive to upper mantle and crust effects, the seismic heterogeneities 300km above the core mantle boundary might still contribute to the differential travel times at close distances. Tomographic corrections are calculated based on the tomography models, using the global S wave tomography model from Stephen P. Grand and the global P wave tomography model from Robert D. van der Hilst. Finally, averaged S and P wave perturbations at the lowermost 300 km mantle are calculated based on corrected ScSH-SH and PcP-P differential travel

time residuals. In this step, we assume a uniformly 300 km thick layer with lateral velocity variations.

As we presented in Chapter 3, a strong mid-lower mantle low shear wave velocity structure is located on the east side of our study region. It is important to check how efficiently tomographic corrections remove the contributions from the mid-lower mantle structure. Here we use the same data set as in Chapter 3. The S wave perturbations of the lowermost mantle based on corrected ScSH-SH differential travel time residuals from this data set range between 0% and -0.5% (Figure 4.2). This indicates that our tomographic corrections efficiently remove most of the contributions from the mid-lower mantle.

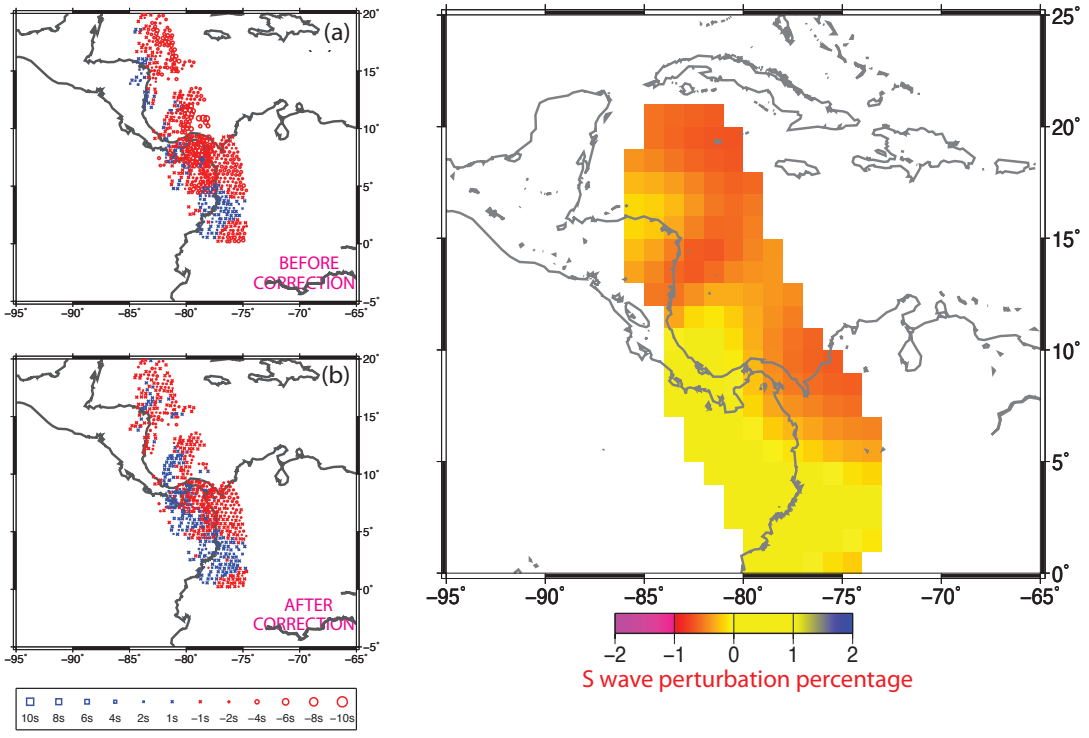

Figure 4.2. Test of tomographic corrections on the "trapezoid-like" low velocity anomaly in the mid-lower mantle. Data include ScSH-SH differential travel time residuals of events 20110824, 20110608, 20110620, 20110902 (same data set as in Chapter 3). Same procedures are taken as for Figure 4.3 and 4.4.

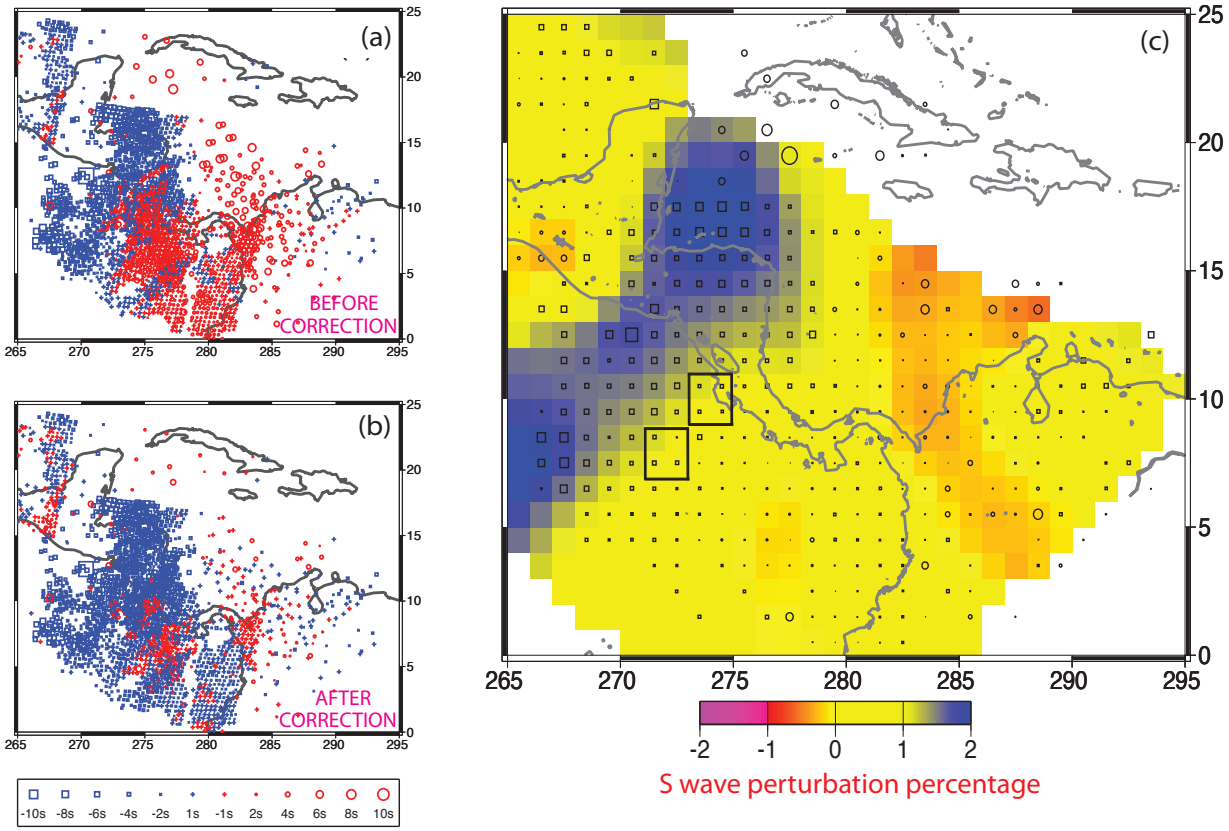

Figure 4.3. Shear wave velocity perturbations at the lowermost 300km mantle using ScSH-SH differential travel time residuals. (a) Absolute ScSH-SH differential travel time residuals with reference to PREM model. (b) Corrected ScSH-SH differential travel time residuals based on the global S wave tomography model from Stephen P. Grand. In (a) and (b), squares represent less than -2s, crosses represent -1s to 1s, and circles represent larger than 2s ScS-SH differential travel time residuals correspondingly. (c) Average S wave velocity perturbation percentages at the lowermost 300km mantle. Squares and circles are averaged values in 1 by 1 degree grid size. Squares represent high velocity perturbations; circles represent low velocity perturbations. Color plottings are Gaussian smoothed perturbations. Two black boxes are the locations of seismic scatter determined by Niu and Wen [2001] based on PKP precursor data.

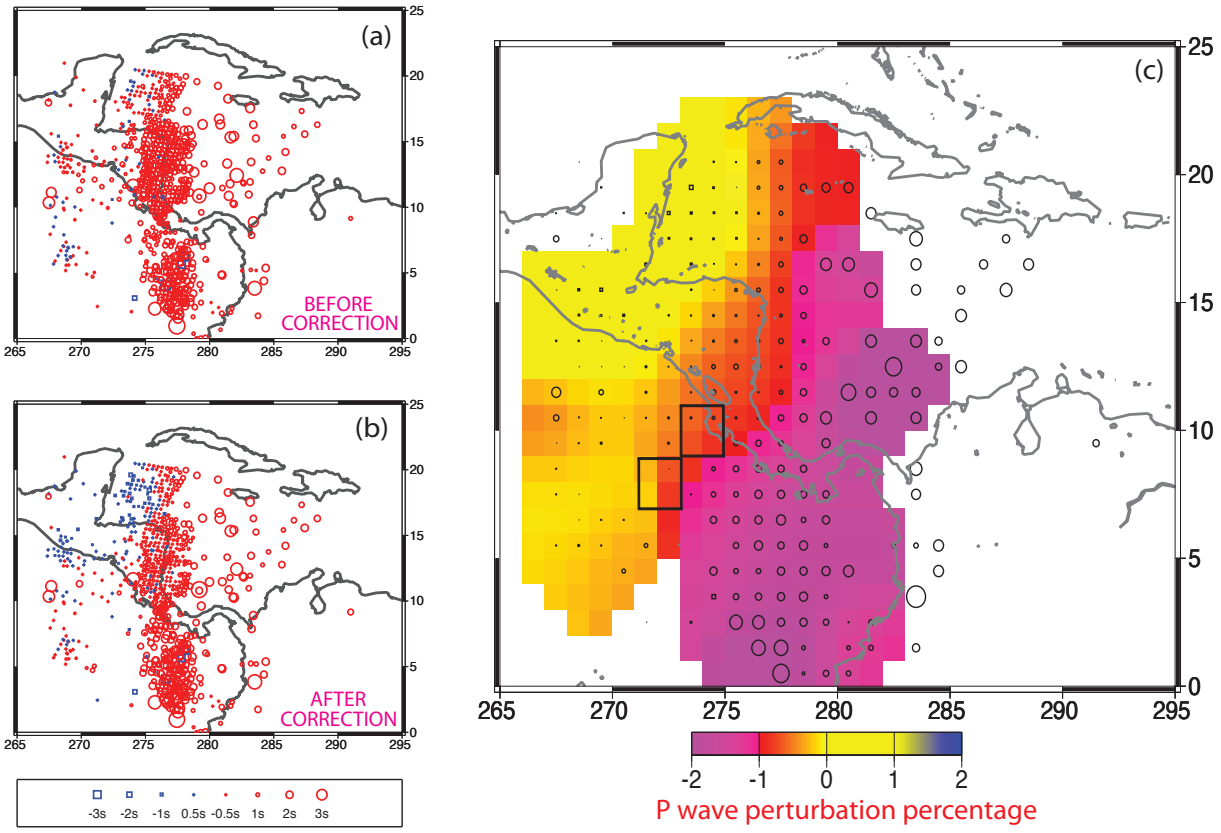

Figure 4.4. Compressional wave velocity perturbations at the lowermost 300km mantle using PcP-P differential travel time residuals. Same as Figure 4.3 except that tomographic corrections are based on the global P wave tomography model from Robert D. van der Hilst.

Looking at absolute ScSH-SH differential travel time residuals of this study (Figure 4.3), we observe negative residuals in the northwest province of the region, positive residuals in the southeast and east province of the region, and mixed residuals in the middle province of the region. The difference between the residuals from the northwest province and residuals from the east province varies up to 10 seconds. After tomographic corrections, mixed ScSH-SH differential travel time residuals in the middle province are reduced significantly, which again proves that tomographic corrections are necessary and effective. Furthermore, the difference between the residuals from the northwest province and residuals from the east province is also

reduced down to approximately 5 seconds. Averaged shear wave velocity perturbations at the lowermost 300 km mantle show that there is a high velocity anomaly with at least 2% velocity perturbation in the northern province. This high velocity anomaly is compatible with other studies. In the southern province, it is normal lowermost mantle. On the east province, there is a weak low velocity anomaly with about -0.5% velocity perturbations. Comparing it with Figure 4.2, the velocity perturbations are about the same magnitudes, and are likely the remaining contributions from the mid-lower mantle.

Looking at absolute and corrected PcP-P differential travel time residuals (Figure 4.4), positive residuals are dominant in most of the region, and very weak negative residuals are observed in a small northwest province. The difference between the residuals from the northwest province and residuals from the east province is 4-5 seconds, similar to shear wave data. Averaged compressional wave velocity perturbations at the lowermost 300 km mantle show that there is a low velocity anomaly with -1% to -2% velocity perturbation in the middle and southern province.

In comparison, a clear anti-correlation between shear wave and compressional wave perturbations is observed in the lowermost 300 km mantle. Interestingly, a similar velocity-decreasing trend exists along the northwest-southeast direction. Shear wave velocity decreases from at lease 2% velocity perturbation to normal, and compressional wave velocity decreases from normal to -2% velocity perturbation. Both shear and compressional velocity experience a 2% of velocity decrease along the

northwest-southeast direction. This feature suggests that a structural transition boundary likely exists at the lowermost mantle beneath Central America.

4.5 Other seismic features

To further constrain seismic features along the structure transitional region, we also look at differences of stacked waveforms, ScSH/SH amplitude ratio, differentiated arrival times of radial and tangential S and ScS phases, and waveform complexity.

Seismic attenuation determines how fast seismic energy is lost during propagation, and constitutes an important characteristic of structures. The direct effects of seismic attenuation are reduced amplitude and broadened waveforms. To investigate seismic attenuation in this region, we focus on waveform broadening caused by attenuation and compare stacked S and ScS waveforms across different geological provinces. Based on the velocity perturbations in the lowermost 300 km mantle, we divide our study region into three provinces. Then S and ScS waveforms are normalized and stacked for each province. For shear waves (Figure 4.5), the black province is the high velocity anomalous province, the red province is the transition province, and the green province is the normal province. Comparing stacked S waveforms across different provinces, we observe gradual waveform broadening when stacking stations move from high velocity anomalous province to the normal province. Similar waveform broadening is observed for stacked ScS waveforms. However, further comparisons between stacked S and ScS waveforms from the same province, exhibit no significant difference. This indicates that the broadening of the stacked S

and ScS waveforms across different provinces is caused by attenuation from upper structures. For compressional waves (Figure 4.6), the black province is the normal province, the red province is the transition province, and the green province is the low velocity anomalous province. Very similar waveforms are observed when comparing between stacked P and PcP waveform across different provinces. Based on joint observations of stacked S and P phase waveforms, seismic attenuation is likely relatively uniform across different provinces in this region.

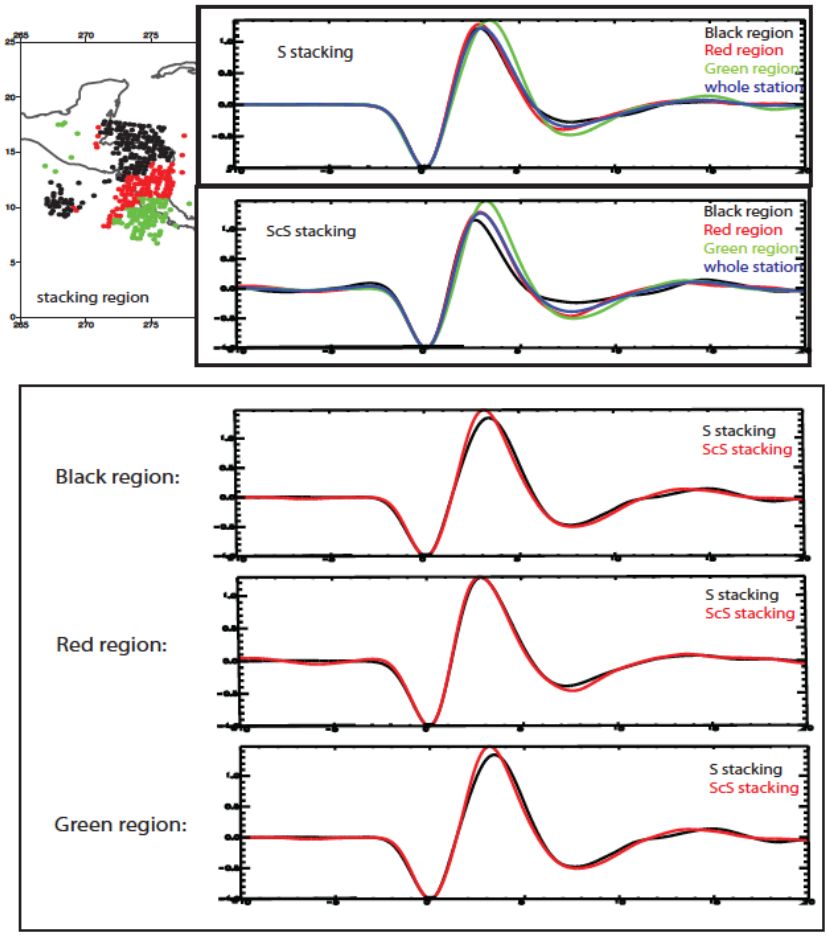

Figure 4.5. (top) Comparisons of stacked S or ScS waveforms between different provinces. The Black, red, green traces correspond to the stacked waveforms of the black, red, green provinces in the left. Blue traces are stacked waveforms based on all stations. (bottom) Comparisons of stacked S and ScS waveforms in the same provinces. Black traces are stacked S waveforms, red traces are stacked ScS waveforms.

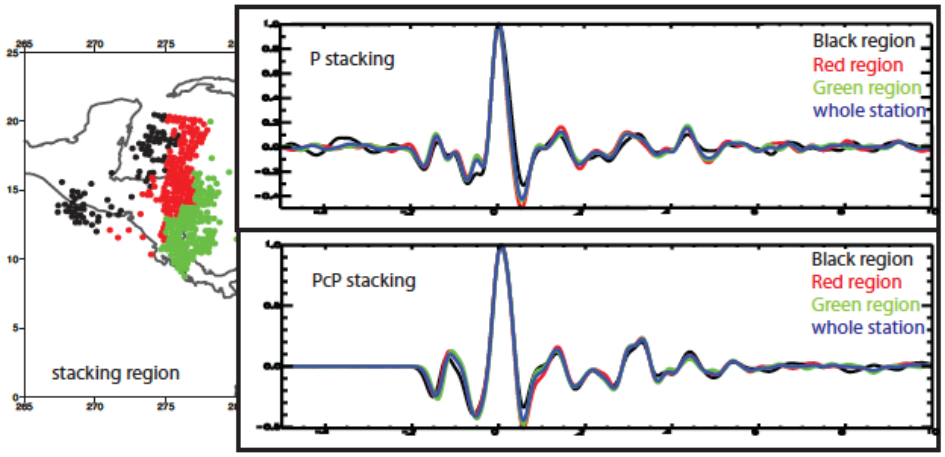

Figure 4.6. Comparisons of stacked P or PcP waveforms between different provinces. The black, red, green traces correspond to the stacked waveforms of the black, red, green provinces in the left. Blue traces are stacked waveforms based on all stations.

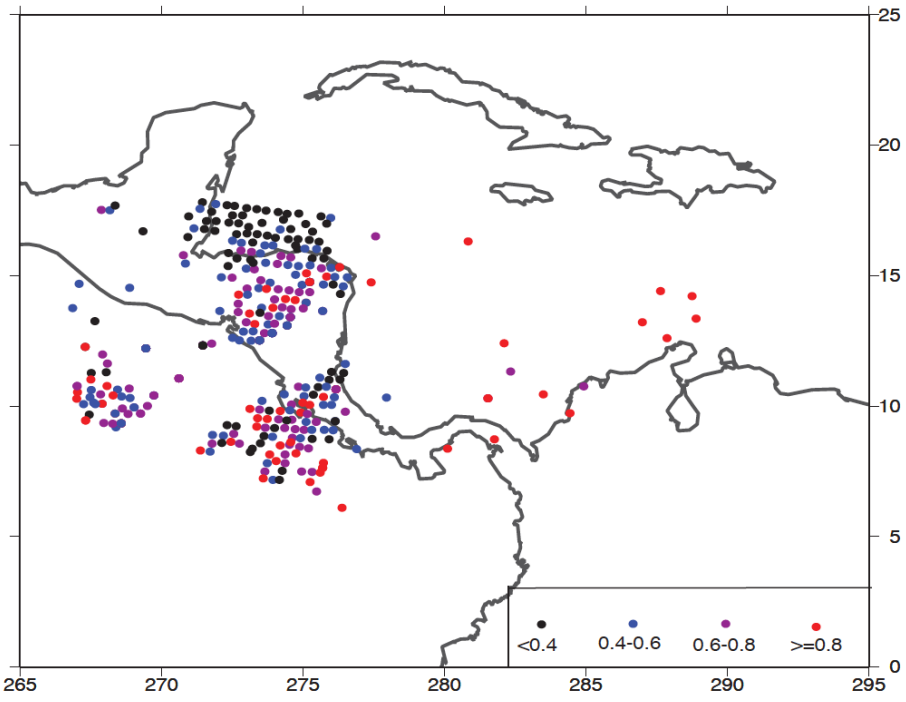

Figure 4.7. The ScSH/SH amplitude ratio plotted at ScS reflection point on the core mantle boundary. Data between 60° and 64° are not used because sS and ScS phases are mixed at this distance window. Different colors represent different ScSH/SH amplitude ratios.

Lateral structural variations have significant effects on the amplitude of waveforms. Figure 4.7 shows the amplitude ratios between the ScSH phase and the SH phase. Along the southeast-northwest direction, we observe gradual amplitude ratio decrease as a function of epicentral distance. But the ScSH/SH amplitude ratio also changes rapidly over very small areas, which cannot be explained by geometric amplitude ratio decay. Furthermore the anisotropy in this region is inferred by comparing the arrival times of two components of a shear phase when polarized horizontally (SH) and vertically (SV). Figure 4.7 shows the differentiated arrival times of SV (radial component) and SH (tangential component). The majority of the data shows positive SV-SH and ScSV-ScSH differential travel time, indicating delayed SV and ScSV arrivals. However, there are also significant differences between SV-SH and ScSV-ScSH differential travel times, which are caused by anisotropy in the lowermost mantle. Rapidly changing ScSH/SH amplitude ratio and incoherently delayed radial component S phases both suggest widely existing anisotropy and heterogeneity.

Relatively simple shear waveforms are observed in this region. An example is shown in Figure 4.9. An “Scd” phase observed beyond 70° is the reflection phase from the top boundary of the high shear wave anomaly. Apart from the S, ScS and Scd phases, no additional phase is observed. The lateral anisotropy and heterogeneity is likely to be of relatively small scale and is not reflected on shear waveform observations.

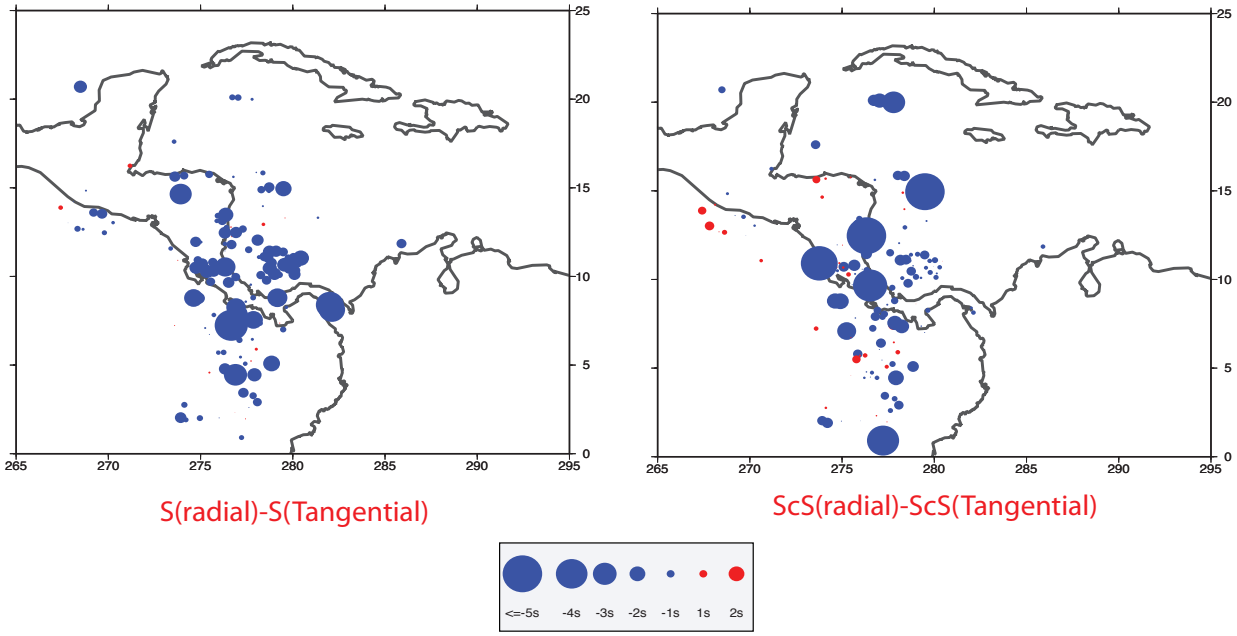

Figure 4.8. Differentiated arrival times of radial and tangential S and ScS arrivals plotted at ScS reflection points on the core mantle boundary.

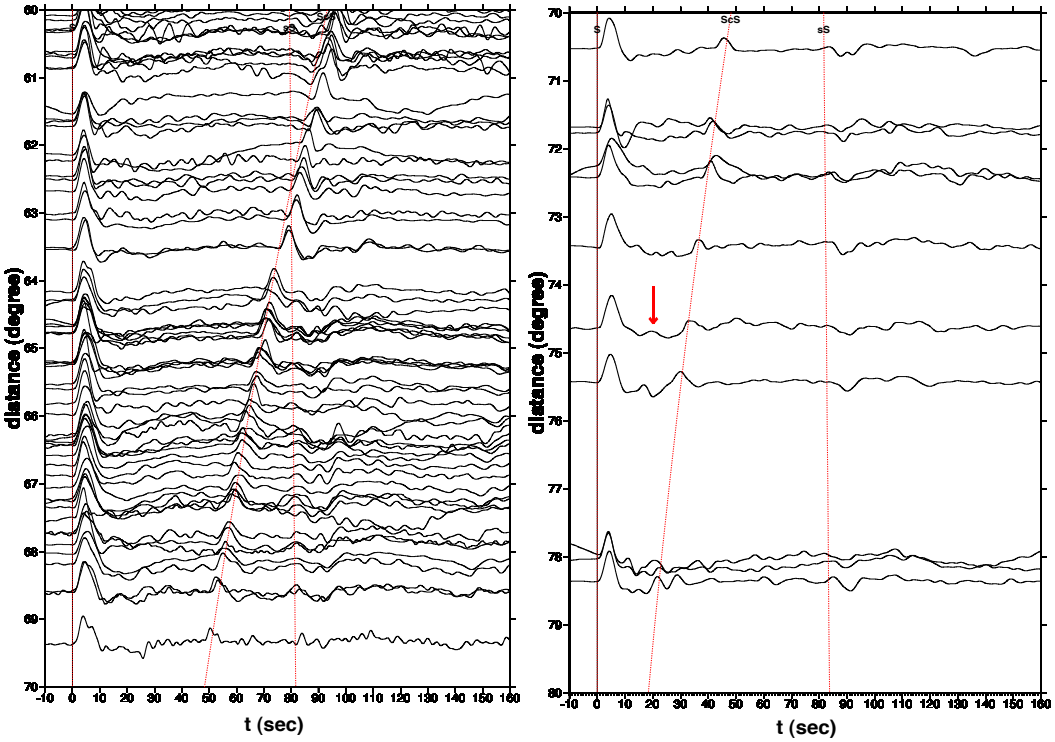

Figure 4.9. Tangential shear waveform aligned by S phase arrival. Red arrow marks "Scd" phase. Red lines are theoretical travel time curves for S, sS and ScS phase.

4.6 Conclusions

We utilize the observed ScSH-SH and PcP-P differential travel time residuals to derive the averaged velocity perturbations in the lowermost 300 km of the mantle beneath Central America. The calculated shear wave velocity structure shows that a high velocity province with at lease 2% velocity perturbation is located in the northern province, and gradually changes to normal in the southern province. The calculated compressional wave velocity structure shows that normal perturbations exist in the northern province, and gradually changes to a low velocity province with -2% velocity perturbations in the southern province. Both shear and compressional velocity experience a 2% of velocity decrease along the northwest-southeast direction, suggesting that a structural transition boundary likely exists at the lowermost mantle beneath Central America. We further constrain seismic features in this region by comparing stacked waveforms, the ScSH/SH amplitude ratio, differentiated arrival time of radial and tangential S and ScS phases, and waveform complexity. Stacked S or ScS waveforms sampling different velocity perturbation provinces are slightly different, but stacked S and ScS waveforms sampling the same velocity perturbation province are very similar. Stacked P or PcP waveforms sampling different velocity perturbations are also very similar. These indicate that attenuation is relatively uniform across different provinces. Rapidly changing ScSH/SH amplitude ratio and incoherently delayed radial component S and ScS phases both indicate widely existing anisotropy and heterogeneity. Relatively simple shear waveform features indicate that the heterogeneity is of relatively small-scale.

Chapter 5

Overall Conclusions

In this thesis, I present two regional studies about the seismic velocity structures beneath Japan and Central America by using body waves. Because these two studies are focused on different aspects of seismic structure, one regarding temporal structure change and the other one regarding spatial seismic structure, different approaches are utilized.

A new theory is derived to locate and quantify temporal structural changes by using difference wave fields of repeated events. The theory states that the difference wave fields of two repeated sources in a temporally changed medium can be equivalently treated as wave fields propagating from conceptual sources, with their location at the place of temporal change and their strengths equal to the product of magnitude of medium property change and magnitude of the initial wave fields from the repeated sources. When the medium change extends to a finite region, the conceptual sources become volumetric sources distributed over the region of the medium change and propagating in the direction of the initial wave. Japan has a great geological setting for studying temporal changing seismic structures, and the new theory is successfully applied here. I search repeating earthquakes occurring in the Japan subduction zone, formulate an empirical procedure to extract the difference wave fields between repeating earthquakes and determine the temporal change of

seismic properties using a back-projection method. I locate the temporal change of seismic properties beneath the Japan subduction zone to be at $(37.2^{\circ}N, 142^{\circ}E)$, and estimate the magnitude of the conceptual body force associated with the temporal change to be 1.15×10^{10} N, or as a reference, a 0.87% density change for an assumed volume of temporal change of 10^3 km^3.

With the great improvement of station coverage by USArray, I am able to study the detailed mid-lower mantle and lowermost mantle structures beneath Central America by using South American earthquake dataset. First, seismic waveform and travel time observations sampling the mid to lower mantle of Central America are analyzed and modeled. Waveform observations show complex reflection phases and exhibit significant variations with azimuth and distance, and travel time analysis shows increasing S residuals of up to 9 seconds as distance increases from 45° to 80°. Forward waveform and travel time modeling reveals that several sub-horizontal 10-20 km thick segments with –10% shear wave velocity perturbation are buried inside a "trapezoid-like" low velocity region with –2% shear wave velocity perturbation extending between 1000 and 2750 km depth. Secondly, a structural transition at the lowermost mantle is suggested based on ScSH-SH and PcP-P differential travel time residuals. The calculated shear wave velocity structure shows that a high velocity province with at lease 2% velocity perturbation is located in the northern province, and gradually changes to normal in the southern province. The calculated compressional wave velocity structure shows that normal perturbations exist in the northern province, and gradually changes to a low velocity province with -2% velocity perturbations in the southern province. Both shear and compressional velocity experience a 2% of

velocity decrease along the northwest-southeast direction, suggesting that a structural transition boundary likely exists at the lowermost mantle beneath Central America. Also, comparisons of stacked waveforms across the region indicate relatively uniform attenuation. Rapidly changing ScSH/SH amplitude ratio and incoherently delayed radial component S and ScS phases both indicate widely existing anisotropy and heterogeneity.

Advanced methods and more data usually bring more answers to the nature of Earth structure. What can we do next? The theory used for quantitatively determination of temporal changes may be used to monitor temporal changes associated with other geological activities, such as glacial, tremor and volcanic activities. Regions with improved data coverage recently could be the next study as well. Rest assured, seismograms will continue to provide insightful information for seismologists.

Bibliography

Aki, K., and P. G. Richards (2002), Elastic waves from a point dislocation source, in *Quantitative seismology (Second Edition)*, edited by J. Ellis, pp. 63-117, University Science Books, Sausalito, Calif.

Ammon, C. J., T. Lay, H. Kanamori and M. Cleveland (2011), A rupture model of the great 2011 Tohoku earthquake, *Earth Planets Space, 63*, 693-696.

Bagley, B., A. M. Courtier, and J. Revenaugh (2013), Seismic shear wave reflectivity structure of the mantle beneath northeast China and northwest Pacific, *J. Geophys. Res.*, *118*, 5417–5427.

Baisch, S. and G. H. R. Bokelmann (2001), Seismic waveform attributes before and after the Loma Prieta earthquake: Scattering change near the earthquake and temporal recovery, *J. Geophys. Res., 106***,** 16,323-16,337.

Bokelmann, G. H. R. and H. P. Harjes (2000), Evidence for temporal variation of seismic velocity within the upper continental crust, *J. Geophys. Res., 105***,** 23,879-23,894.

Bonnin, P., H. Debbabi, J. Mariani, C. Charriaut-Marlangue and S. Renolleau (2008), Ultrasonic assessment of cerebral blood flow changes during ischemia-reperfusion in 7-day-old rats, *Ultrasound Med. Biol., 34***,** 913-922.

Brenguier, F., N. M. Shapiro, M. Campillo, V. Ferrazzini, Z. Duputel, O. Coutant and A. Nercessian (2008a), Towards forecasting volcanic eruptions using seismic noise, *Nat. Geosci., 1***,** 126-130.

Brenguier, F., M. Campillo, C. Hadziioannou, N. M. Shapiro, R. M. Nadeau and E. Larose (2008b), Postseismic relaxation along the San Andreas Fault at Parkfield from continuous seismological observations, *Science*, *321*, 1478-1481.

Cao, A., Y. Masson and B. Romanowicz (2007), Short wavelength topography on the inner-core boundary, *P. Natl. Acad. Sci. USA, 104***,** 31-35.

Cheng, X., F. Niu, P. G. Silver and R. M. Nadeau (2011), Seismic Imaging of Scatterer Migration Associated with the 2004 Parkfield Earthquake Using Waveform Data of Repeating Earthquakes and Active Sources, *Bull. Seismol. Soc. Am., 101***,** 1291-1301.

Chu, R., S. Wei, D. V. Helmberger, Z. Zhan, L. Zhu and H. Kanamori (2011), Initiation of the great Mw 9.0 Tohoku-Oki earthquake, *Earth Planet. Sci. Lett.*, *308*, 277-283.

Courtier, A. M. and J. Revenaugh (2008), Slabs and shear wave reflectors in the midmantle, *J. Geophys. Res., 113*, B08312, doi:10.1029/2007JB005261.

Deuss, A. (2009), Global observations of mantle discontinuities using SS and PP precursors, *Surv. Geophys*., *30*, 301-326.

Dziewonski, A.M. and D. L. Anderson (1981), Preliminary reference Earth model, *Phys. Earth Planet In., 25***,** 297-356.

Els, T., M. Daffertshofer, H. Schroeck, W. Kuschinsky and H. Hennerici (1999), Comparison of transcranial Doppler flow velocity and cerebral blood flow during focal ischemia in rabbits, *Ultrasound Med. Biol., 25***,** 933-938.

Furumoto, M., Y. Ichimori, N. Hayashi, Y. Hiramatsu and T. Satoh (2001), Seismic wave velocity changes and stress build-up in the crust of the Kanto-Tokai region, *Geophys. Res. Lett., 28***,** 3737-3740.

Garnero, E. D. and T. Lay (2003), D'' shear velocity heterogeneity, anisotropy and discontinuity structure beneath the Caribbean and Central America, *Phy. Earth Plant. Int., 140*, 219-242.

Grand, S. P. (1994), Mantle shear structure beneath the Americas and surrounding oceans, *J. Geophys. Res.*, *99*, 11,591–11,621.

Grand, S. P. and D. V. Helmberger (1984), Upper mantle shear structure of North America, *Geophys. J. Roy. Astron. Soc., 76*, 399-438.

Grand, S. P., R. D. van der Hilst and S. Widiyantoro (1997), Global seismic tomography: A snapshot of convection in the Earth, *GSA Today*, *7*, 1-7.

Gret, A., R. Snieder and J. Scales (2006), Time-lapse monitoring of rock properties with coda wave interferometry, *J. Geophys. Res., 111,* B03305, doi:10.1029/2004JB0003354.

He, Y. and L. Wen (2012), Geographic boundary of the "Pacific Anomaly" and its geometry and transitional structure in the north, *J. Geophys. Res., 117*, B09308, doi:10.1029/2012JB009436.

Hutko, A. R., T. Lay, E. J. Garnero and J. Revenaugh (2006), Seismic detection of folded, subducted lithosphere at the core-mantle boundary, *Nature*, *441*, 333-336.

Ide, S., A. Baltay, and G. C. Beroza (2011), Shallow Dynamic Overshoot and Energetic Deep Rupture in the 2011 M(w) 9.0 Tohoku-Oki Earthquake, *Science, 332***,** 1426-1429.

Ikuta, R. and K. Yamaoka (2004), Temporal variation in the shear wave anisotropy detected using the Accurately Controlled Routinely Operated Signal System (ACROSS), *J. Geophys. Res., 109,* B09305, doi:10.1029/2003JB002901.

Kaneshima, S. (2013), Lower mantle seismic scatterers below the subducting Tonga slab: Evidence for slab entrainment of transition zone materials, *Phy. Earth Plant. Int.*, *222*, 35-46.

Kaneshima, S. and G. Helffrich (1999), Dipping low-velocity layer in the mid-lower mantle: evidence for geochemical heterogeneity, *Science*, *283*, 1888-1892.

Kaneshima, S. and G. Helffrich (2010), Small scale heterogeneity in the mid-lower mantle beneath the circum-Pacific area, *Phy. Earth Plant. Int., 183*, 91-103.

Kawakatsu, H. and F. Niu (1994), Seismic evidence for a 920-km discontinuity in the mantle, *Nature*, *371*, 301-305.

Lay, T. and D. V. Helmberger (1983), A lower mantle S-wave triplication and the shear velocity structure of D'', *Geophys. J. R. astr. Soc., 75*, 799-837.

Li, J. and D. A. Yuen (2014), Mid-mantle heterogeneities associated with Izanagi plate: Implications for regional mantle viscosity, *Earth Plant. Sci. Lett*, *385,* 137-144.

Li, L., Z. Ke, K. Tong and M. Ying (2010), Evaluation of cerebral blood flow changes in focal cerebral ischemia rats by using transcranial Doppler ultrasonography, *Ultrasound Med. Biol., 36***,** 595-603.

Li, Y., J. E. Vidale, K. Aki, F. Xu and T. Burdette (1998), Evidence of shallow fault zone strengthening after the 1992 M7.5 Landers, California, Earthquake, *Science, 279***,** 217-219.

Li, Y., P. Chen, E. S. Cochran and J. E. Vidale (2007), Seismic velocity variations on the San Andreas fault caused by the 2004 M6 Parkfield Earthquake and their implications, *Earth Planets Space, 59***,** 21-31.

Lin, F., M. P. Moschetti and M. H. Ritzwoller (2008), Surface wave tomography of the western United States from ambient seismic noise: Rayleigh and Love wave phase velocity maps, *Geophys. J. Int.,* doi: 10.1111/j.1365-246X.2008.03720.x.

Lithgow-Bertelloni, C. and M. A. Richards (1998), The dynamics of Cenozoic and Mesozoic plate motions, *Rev. Geophys*., *36,* 27-78.

Liu, L. and Stegman, D. R. (2011), Segmentration of the Farallon slab, *Earth Planet. Sci. Lett.*, *311*, doi: 10.1016/j.epsl.2011.09.027.

Lumley, D. E. (2001), Time-lapse seismic reservoir monitoring, *Geophysics, 66***,** 50-53.

Martini, F., C. J. Bean, G. Saccorotti, F. Viveiros and N. Wallenstein (2009), Seasonal cycles of seismic velocity variations detected using coda wave interferometry at Fogo volcano, Sao Miguel, Azores, during 2003-2004, *J. Volcanol Geoth. Res., 181***,** 231-246.

Matsumoto, S., K. Obara, K. Yoshimoto, T. Saito, A. Ito and A. Hasegawa (2001), Temporal change in P-wave scatterer distribution associated with the M6.1 earthquake near Iwate volcano, northeastern Japan, *Geophys. J. Int., 145***,** 48-58.

Miller, M. S. and F. Niu (2008), Bulldozing the core-mantle boundary: Localized seismic scatterers beneath the Caribbean Sea, *Phys. Earth and Planet. Int., 170*, 89-94.

Nakajima, J. and A. Hasegawa (2006), Anomalous low-velocity zone and linear alignment of seismicity along it in the subducted Pacific slab beneath Kanto, Japan: Reactivation of subducted fracture zone?, *Geophys. Res. Lett.*, *33,* L16309, doi: 10.1029/2006GL026773.

Nakajima, J., F. Hirose and A. Hasegawa (2009), Seismotectonics beneath the Tokyo metropolitan area, Japan: Effect of slab-slab contact and overlap on seismicity, *J. Geophys. Res., 114,* B08309, doi: 10.1029/2008JB006101.

Ni, D., E. Tan, M. Curnis and D. V. Helmberger (2002), Shape sides to the African superplume, *Science, 296,* 1850-1852.

Nishimura, T., S. Tanaka, T. Yamawaki, H. Yamamoto, T. Sano, M. Sato, H. Nakahara, N. Uchida, S. Hori and H. Sato (2005), Temporal changes in seismic velocity of the crust around Iwate volcano, Japan, as inferred from analyses of repeated active seismic experiment data from 1998 to 2003, *Earth Planets Space, 57***,** 491-505.

Niu, F. and H. Kawakatsu (1997), Depth variation of the mid-mantle seismic discontinuity, *Geophys. Res. Lett., 24*, 429-432.

Niu, F., H. Kawakatsu and Y. Fukao (2003), Seismic evidence for a chemical heterogeneity in the midmantle: a strong and slightly dipping seismic reflector beneath the Mariana subduction zone, *J. Geophys. Res., 108*, doi:10.1029/2002JB002384.

Niu, F., P. G. Silver, R. M. Nadeau, and T.V. McEvilly (2003), Stress-Induced Migration of Seismic Scatterers Associated with the 1993 Parkfield Aseismic Transient Event, *Nature*, *426*, 544-548.

Niu, F., P. G. Silver, T. M. Daley, X. Cheng and E. L. Majer (2008), Preseismic velocity changes observed from active source monitoring at the Parkfield SAFOD drill site, *Nature, 454***,** 204-U244.

Niu, F. and L. Wen (2001), Strong seismic scatterers near the core-mantle boundary west of Mexico, *Geophys. Res. Lett., 28***,** 3557-3560.

Obrebski, M., Allen. R. M., Pollitz, F. and Hung, S. (2011), Lithosphere–asthenosphere interaction beneath the western United States from the joint inversion of body-wave traveltimes and surface-wave phase velocities, *Geophys. J. Int., 185*, 1003–1021.

Peng, Z.G. and Y. Ben-Zion (2006), Temporal changes of shallow seismic velocity around the Karadere-Duzce branch of the North anatolian fault and strong ground motion, *Pure Appl. Geophys., 163***,** 567-600.

Poupinet, G., W. L. Ellsworth and J. Frechet (1984), Monitoring velocity variations in the crust using earthquake doublets: An application to the Calaveras Fault, California, *J. Geophys. Res., 89***,** 5719-5731.

Ren, Y., E. Stutzmann, R. D. van der Hilst and J. Besse (2007), Understanding seismic heterogeneities in the lower mantle beneath the Americas from seismic tomography and plate tectonic history, *J. Geophys. Res*., *112*, doi: 10.1029/2005JB004154.

Rickett, J. E. and D. E. Lumley (2001), Cross-equalization data processing for time-lapse seismic reservoir monitoring: A case study from the Gulf of Mexico, *Geophysics, 66***,** 1015-1025.

Ritsema, J., H. J. van Heijst, and J. H. Woodhouse (1999), Complex shear wave velocity structure imaged beneath Africa and Iceland, *Science, 286,* 1925– 1928.

Rubinstein, J. L., N. Uchida and G. C. Beroza (2007), Seismic velocity reductions caused by the 2003 Tokachi-Oki earthquake, *J. Geophys. Res., 112*, B05315, doi:10.1029/2006JB00440.

Santos, E. T. F. and J. M. Harris (2009), DynaSIRT: A robust dynamic imaging method applied to CO2 injection monitoring, *SEG Expanded Abstract, 28***,** 4019.

Schaff, D. P. and G. C. Beroza (2004), Coseismic and postseismic velocity changes measured by repeating earthquakes, *J. Geophys. Res., 109*, B10302, doi:10.1029/2004JB003011.

Sens-Schonfelder, C. and U. Wegler (2006), Passive image interferometry and seasonal variations of seismic velocities at Merapi Volcano, Indonesia, *Geophys. Res. Lett., 33*, L21305, doi:10.1029/2006GL027797.

Shen, Y., C. J. Wolfe and S. C. Solomon (2003), Seismological evidence for a mid-mantle discountinuity beneath Hawaii and Iceland, *Earth Planet. Sci. Lett., 214,* 143-151.

Sigloch, K. (2011), Mantle provinces under North America from multi-frequency P-wave tomography, *Geochem. Geophys. Geosyst., 12,* DOI: 10.1029/2010GC003421.

Sigloch, K., N. McQuarrie and G. Nolet (2008), Two-stage subduction history under North America inferred from multiple-frequency tomograpgy, *Nature Geoscience*, *1*, 458-462.

Snieder, R., A. Gret, H. Douma and J. Scales (2002), Coda wave interferometry for estimating nonlinear behavior in seismic velocity, *Science, 295***,** 2253-2255.

Snieder, R., (2006), The theory of coda wave interferometry, *Pure Appl. Geophys., 163***,** 455-73.

Snieder, R., S. Hubbard, M. Haney, G. Bawden, P. Hatchell, A. Revil and D. G. M. Working (2007), Advanced noninvasive geophysical monitoring techniques, *Annu. Rev. Earth Planet. Sci., 35***,** 653-683.

Stunff, Y. L., C. W. Wicks Jr. and B. Romanowicz (1995), P'P' precursors under Africa: Evidence for mid-lower reflectors, *Sciecne, 270,* 74-77, 1995.

Su, W. J., R. L. Woodwoard, and A. M. Dziewonski (1992), Degree 12 model of shear velocity heterogeneity in the mantle, *J. Geophys. Res., 99*, 6945– 6980.

Sun, D., T. A. Song and D. V. Helmberger (2006), Complexity of D'' in the presence of slab-debris and phase changes, *Geophys. Res. Lett*., *33*, doi: 10.1029/2005GL025384.

Sun. D. and D. V. Helmberger (2011), Upper-mantle structures beneath USArray derived from waveform complexity*, Geophys. J. Int., 184*, 416-438.

Taira, T., P. G. Silver, F. Niu, and R. M. Nadeau (2008), Detecting seismogenic stress evolution and constraining fault zone rheology in the San Andreas Fault following the 2004 Parkfield earthquake, *J. Geophys. Res., 113*, B03303, doi:10.1029/2007JB005151.

Tanaka, S., D. Suetsugu, H. Shiobara, T. Kanazawa, Y. Fukao, G. Barruol and D. Reymod (2009), On the vertical extent of the large low shear velocity province beneath the South Pacific Superswell, *Geophys. Res. Lett., 36,* L07305, doi:10.1029/2009GL037568.

Thomas, C., E. J. Garnero and T. Lay (2004), High-resolution imaging of lowermost mantle structure, *J. Geophys. Res., 109*, doi: 10.1029/2004JB003013.

To, A., B. Romanowicz, Y. Capdeville and N. Takeuchi (2005), 3D effects of sharp boundaries at the borders of the African and Pacific Superplumes: Observation and modeling, *Earth Planet. Sci. Lett., 233*, 137-153.

van der Lee, S. and G. Nolet (1997), Upper mantle S velocity structure of North America, *J. Geophys. Res., 102*, 22,815-22,838.

van der Lee, S., K. Regenauer-Lieb and D. A. Yuen (2008), The role of water in connecting past and future episodes of subduction, *Earth Planet. Sci. Lett., 273*, 15-27, doi:10.1016/j.epsl.2008.04.041.

van der Lee, S. and A. Frederiksen (2013), Surface wave tomography applied to the North America, *in Seismic Earth: Array Analysis of Broadband Seismograms* (eds A. Levander and G. Nolet), American Geophysical Union, Washington, D.C.. doi: 10.1029/157GM05.

van der Hilst, R. D., S. Widiyantoro and E. R. Engdahl (1997), Evidence for deep mantle circulation from global tomography, *Nature*, *386*, 578-584.

Vanacore, E., F. Niu and H. Kawakatsu (2006), Obervations of the mid-mantle discontinuity beneath Indonesia from S to P converted waveforms, *Geophys. Res. Lett., 33,* L04302, doi:10.1029/2005GL025106.

Vidale, J. E. and Y. Li (2003), Damage to the shallow Landers fault from the nearby Hector Mine earthquake, *Nature, 421***,** 524-526.

Vinnik, L., M. Kato, and H. Kawakatsu (2001), Search for seismic discontinuities in the lower mantle, *Geophys. J. Int., 147*, 41-56.

Vinnik, L. P., S. I. Oreshin, S. Speziale and M. Weber (2010), Mid-mantle layering from SKS receiver functions, *J. Geophys. Res., 37*, L24302, doi:10.1029/2010GL045323.

Wang, Y. and L. Wen (2007), Geometry and P and S velocity structure of the "African Anomaly", *J. Geophys. Res*., *112*, B05313, doi:10.1029/2006JB004483.

Wegler, U. and C. Sens-Schonfelder (2007), Fault zone monitoring with passive image interferometry, *Geophys. J. Int., 168***,** 1029-1033.

Wen, L. (2000), Intense seismic scattering near the Earth's core-mantle boundary beneath the Comoros hotspot, *Geophys. Res. Lett., 27***,** 3627-3630.

Wen, L. (2002), An SH hybrid method and shear velocity structures in the lowermost mantle beneath the central Pacific and South Atlantic Oceans, *J. Geophys. Res., 107*, 2055, doi:10.1029/2001JB000499.

Wen, L. (2006), Localized temporal change of the earth's inner core boundary, *Science, 314***,** 967-970.

Wessel, P., and W. H. F. Smith (1995), New version of the Generic Mapping Tools released, *Eos Trans. AGU, 76(33)*, 329.

Wysession, M. E., K. M. Fischer, G. I. Al-eqabi, P. J. Shore and I. Gurari, (2001), Using MOMA broadband array ScS-S data to image smaller scale strucutures at the base of the mantle, *Geophys. Res. Lett., 28*, 867-870.

Yoshito, F., S. Widiyantoro and M. Obayashi (2001), Stagnant slabs in the upper and lower mantle transition region, *Reviews of Geophysics*, *39*, 291-323.

Young, R. P. and D. S. Collins (2001), Seismic studies of rock fracture at the Underground Research Laboratory, Canada, *Int. J. Rock Mech. Min., 38***,** 787-799.

Yu, W. and L. Wen (2012), Deep-focus repeating earthquakes in the Fiji-Tonga subduction zone, *Bull. Seis. Soc. Am., 102,* 1829-1849.

Yue, H. and T. Lay (2011), Inversion of high-rate (1sps) GPS data for rupture process of the 11 March 2011 Tohoku earthquake (Mw 9.1), *Geophys. Res. Lett., 38,* L00G09, doi:10.1029/2011GL048700.

Zhang, J., X. Song, Y. Li, P. G. Richards, X. Sun and F. Waldhauser (2005), Inner core differential motion confirmed by earthquake waveform doublets, *Science, 309***,** 1357-1360

Zhang, J., P. G. Richards and D. P. Schaff (2008), Wide-scale detection of earthquake waveform doublets and further evidence for inner core super-rotation, *Geophys. J. Int., 174***,** 993-1006.

Zhao, P. and Z. Peng (2009), Depth extent of damage zones around the central Calaveras fault from waveform analysis of repeating earthquakes, *Geophys. J. Int.*, *179,* 1817-1830.